Whole-head functional brain imaging of economic risk decision making and transcranial photobiomodulation with fNIRS and EEG

Hashini I. Wanniarachchi

Presented to the Faculty of the Graduate School of

The University of Texas at Arlington in Partial Fulfillment

of the Requirements

for the Degree of

DOCTOR OF PHILOSOPHY

THE UNIVERSITY OF TEXAS AT ARLINGTON

August 2020

Acknowledgment

First, I would like to acknowledge my supervising professor Dr. Hanli Liu for her continuous support in terms of guidance and inspiration all through my path towards completing the degree. I appreciate the time that I spent in the lab and under her guidance. If not for here, I will not be who I am today.

Second, I thank my committee members Dr. Alexandrakis, Dr. Wang, Dr. Chen, and Dr. Nerur for their support.

Third, I would like to express my especial gratitude for Dr. Wang for continuous support throughout the years. Moreover, I would like to thank all my friends and lab-mates for always being by my side, with special thanks to Dr. Wu, Dr. Parisa Rabbani, Dr. Olajide Babawale, Akhil Chaudhri, Dr. Nghi Troung, Dr. Liangchieh Ma, Tyrell Pruitt, Dr. Elizabeth Urqhart and Devarshi Desai.

Finally, and most importantly, I would like to thank my family for always being there for me and supporting me in every possible way. I especially would like to mention my brother, Ranuka Wanniarachchi, for providing me unconditional love and support for having a good education and a good life.

September 04, 2020

Abstract

Whole-head functional brain imaging of economic risk decision making and transcranial photobiomodulation with fNIRS and EEG

Hashini Wanniarachchi

The University of Texas at Arlington, 2020

Supervising Professor: Dr. Hanli Liu

Functional near-infrared spectroscopy (fNIRS) and electroencephalography (EEG) are two non-invasive brain imaging or mapping modalities that allow us to measure cerebral hemodynamic and electrophysiological changes in the human brain, respectively. LABNIRS is a cutting-edge, whole-head, optical brain mapping system with 40 pairs of light sources (at 780 nm830 nm) and 40 detectors, forming up to 133 detection channels. In my study, whole-head LABNIRS and 64-channel EEG were utilized to investigate respective alterations in response to risk decision- making under business context and to non-invasive photobiomodulation.

As the first part of my study, I utilized fNIRS (i.e., LABNIRS) as a tool to measure hemoglobin concentration changes across the frontal regions in response to the newsvendor problem (NP). NP is an essential concept in the research area of business operations. The scenario refers to the decision-making in an inventory management context in a highly uncertain environment where an individual must balance between potential loss and waste to achieve maximum expected profit. However, there are few studies to investigate this concept from the perspective of neuroimaging. Consequently, with 77-channel fNIRS measurements taken from 27 human subjects, I reported in Chap. 2 that significant activation induced by NP was shown in both the dorsolateral prefrontal cortex (DLPFC) and orbitofrontal cortex (OFC) across all subjects.

Specifically, higher risk NP with low-profit margins (LM) activated left-DLPFC but deactivated right-DLPFC in 14 subjects while lower risk NP with high-profit margins (HM) stimulated both DLPFC and OFC in 13 subjects. Moreover, graph theory-based network analysis was performed and showed that global brain network properties altered when the human brain switched from rest to the NP-evoked phase. The clustering coefficient of the network was significantly enhanced under both LM and HM, while the small-worldness was boosted by higher-risk decision taking.

Transcranial photobiomodulation (tPBM) is a light-based technique to stimulate the human brain non-invasively. It is proven to improve human cognition, such as memory and reaction time. tPBM is also shown that tPBM delivered to the healthy human forehead enhances not only hemodynamic and metabolic functions but also the EEG power in alpha and beta brain rhythms during eyes-open resting state. Nonetheless, the tPBM-induced effect under the eyes-closed resting state is unknown, and whether the measured changes in EEG powers could result directly from laser heating is also unclear. As the second part of my study, Chapter 3 explores the impact of tPBM on neuro-electrophysiological functions under the eyes-closed resting state and the effect of heat produced by the laser on the EEG power alterations. My results suggest that tPBM increased alpha, and beta EEG power during eyes-closed resting state relative to those under sham, consistent with our previous results reported under eyes-opened conditions. On the other hand, thermal stimulation reduced alpha and beta powers relative to sham, showing the opposite trends to those induced by tPBM and separating the confounding effects between tPBM and heat.

While previous studies have reported tPBM-induced hemodynamic increases near the stimulation site, it is unclear if the impact is limited to only the stimulation site or across multiple cortical areas in the brain. To answer this question, as the third part of my study, whole-head fNIRS was used to detect/map tPBM-evoked hemodynamic activations and network alterations from 19

healthy human subjects. Chapter 4 reported that significant activation of hemodynamics near the right prefrontal cortex increased over the time span of the stimulation period relative to that during the sham condition. Some activation in the left primary somatosensory area was also seen, probably due to the heat sensation of the laser. Furthermore, dynamic functional connectivity analysis was performed and showed that the brain connectivity increased across the entire cortical areas during the later portion of tPBM, followed by slight decreases during the post-stimulation.

Table of Contents

Table of Figures

List of Tables

Chapter 1- Introduction

1.1 Functional Near-Infrared Spectroscopy as a Tool to Measure Whole-head Hemodynamic Alterations

Functional Near-Infrared spectroscopy is a non-invasive optical imaging modality that is capable of measuring hemodynamics in the human brain at the cortical level. Multi-channel fNIRS is a portable and non-invasive imaging technique that measures cortical hemodynamic activities in the human brain. It quantifies the cerebral concentration changes of oxygenated hemoglobin (Δ[HbO]) and deoxygenated hemoglobin (Δ[Hb]) with the high temporal resolution based on the alteration of optical absorption and scattering of near-infrared (NIR) light propagating through the human brain. The temporal and spatial features of Δ[HbO] and Δ[Hb] are then used as biomarkers of neuronal activations[1]. In the last two decades, fNIRS has gained popularity and is recognized as a non-invasive tool to functionally image brain activations and/or diagnose brain diseases[2]. Compared to fMRI, fNIRS is cost-effective, less sensitive to motion artifacts, and with a higher temporal resolution, all of which makes it easier to use in a task-oriented, more-naturistic experimental environment. An fNIRS system consists of single or multiple channels made with a light source and a detector. The intensity of the source and loss of the outcoming intensity of the signal is measured using a detector. The intensity change of light in the near-infrared region is converted into relative hemoglobin concentrations (i.e., [HbO] and [Hb]) using Modified Beer-Lambert Law (MBLL). An alteration in optical density ΔOD can be described using MBLL as follows:

$$\Delta OD(\lambda) = log_{10}[\frac{I_0(\lambda)}{I(\lambda)}] \quad \text{(1-1)}$$

I_0 /I represent the ratio between incoming and outgoing intensity as a function of wavelength (λ). Corresponding to the MBLL [3, 4], ΔOD at each λ could be conveyed as a sum of optical absorbance accounted by HbO, and Hb elements:

$$\Delta OD(\lambda) = \{\Delta[HbO] * \varepsilon_{HbO}(\lambda) + \Delta[Hb] * \varepsilon_{Hb}(\lambda) * L(\lambda), \quad (1\text{-}2)$$

where Δ[HbO] is the relative change in HbO concentration, Δ[Hb] is the relative change in Hb concentration, $\varepsilon_{HbO}(\lambda)$, and $\varepsilon_{Hb}(\lambda)$ is the extinction coefficients of HbO, and Hb, which is accessible in ref. [5], and L(λ) denotes the pathlength of the spotted photons across the tissues. Moreover, L(λ) can be estimated as:

$$L(\lambda) = r * DPF(\lambda), \quad (1\text{-}1)$$

where 'r' is the source-detector distance, and DPF(λ) is the wavelength-dependent differential pathlength factor. By swapping Eq. (1-3) into Eq. (1-2) for multiple wavelengths, I can illustrate Δ[HbO], and Δ[Hb] in a matrix format related to two wavelengths ΔOD (λ) over DPF(λ), as follows:

$$\begin{bmatrix}\Delta[HbO] \\ \Delta[Hb]\end{bmatrix} = \frac{1}{r} * \begin{bmatrix}\varepsilon_{HbO}(\lambda_1) & \varepsilon_{Hb}(\lambda_1) \\ \varepsilon_{HbO}(\lambda_2) & \varepsilon_{Hb}(\lambda_2)\end{bmatrix}^{-1} \begin{bmatrix}\frac{\Delta OD(\lambda_1)}{DPF(\lambda_1)} \\ \frac{\Delta OD(\lambda_2)}{DPF(\lambda_2)}\end{bmatrix} \quad (1-4)$$

A continuous-wave, multi-channel fNIRS system (LABNIRS, Shimadzu Corp., Kyoto, Japan) was utilized for the study, which consists of 40-sources and detectors creating more than 133 channels. The system is sourced with laser diodes with 3 wavelengths (780, 805, and 830nm). The LABNIRS system was used for studying hemodynamic response during the newsvendor problem, which lacks a neuroimaging overview with a 77-channel custom layout and a comprehensive protocol.

1.2 Newsvendor Problem: An Economic Decision-Making Task in Need of Neuroimaging Investigation using fNIRS

Newsvendor Problem (NP) is one of the significant concepts associated with management science [8]; it refers to a prevalent business decision-making scenario, where an individual has to balance between potential loss and waste to achieve maximum expected profit. The typical scenario is that of a store manager deciding the number of units of products to stock when the number of customers is uncertain [6]. Too little stock leads to potential lost sales; too much stock leads to potential waste. Risky decisions are needed to stock the inventory for profit under arbitrary requirements. In such a decision contained risks, the likelihood of the consequence is known. However, a safe or risky outcome differs in terms of the reward [7]. There are a few empirical research on the brain activities underlying decisions made under varying conditions of risk. Previous neuroeconomics literature reported that there are three processes involved in risk decision-making processes, namely, reward processing, cognitive control, and social cognition [8]. These processes trigger mainly the dorsolateral prefrontal cortex (DLPFC), orbitofrontal cortex (OFC), and angular cingulate cortex (ACC) along with several other regions in the brain as a network shown in the fMRI studies [9].

1.3 Need for Quantifying Electrophysiological and Hemodynamic Fluctuations due to Transcranial Photobiomodulation(tPBM) using EEG /fNIRS During the Eyes-closed Resting State.

Transcranial photobiomodulation (tPBM) is a light-based technique to stimulate the human brain non-invasively. Recent studies have shown that tPBM using a 1064-nm laser can be applied to improve cognitive functions on healthy brains. This non-invasive optical neuromodulation tool has been reported to enhance human cognitive performance on a variety of cognitive tasks using sham-

controlled experiments with about 300 human subjects [10-13]. Our previous studies have objectively measured and observed significantly enhanced concentrations of hemoglobin oxygenation and oxidized cytochrome-c-oxidase (CCO) during and after tPBM on human right frontal-cortex with high reproducibility and robustness [14-16]. This validated the hypothesized theory/mechanism for tPBM to photo-oxidize CCO to boost the metabolism rate of cells/neurons [17].

Moreover, using scalp EEG, power enhancement of larger-scale alpha and beta rhythms in the eyes-open resting state human brain were reported during and after tPBM [18, 19]. This observation indicated that tPBM not only increased oxygenation and metabolism rate of neurons but also enhanced the firing rate of neurons and connectivity of the brain. Although with different experimental protocols, these findings showed great consistency with many independent studies on EEG responses to tPBM from other research groups [20, 21]. However, it is known that the eyes-open and eyes-closed EEG behave distinctively in the human brain [22]. Also, the powers of brain waves/EEG signals are more vulnerable to eye-blinks and drowsiness in the eyes-open resting state compared to the eyes-closed resting state. This emphasized the essence of measuring tPBM-induced power changes of brain oscillation during eyes-closed human resting states. Moreover, we observed that the laser beam produces a warm sensation on the subject's forehead. Since the EEG signal is sensitive to sensations [21], the warmness created by tPBM can potentially affect the EEG signal. Thus, the improvement of behavioral performances and EEG power we observed in previous studies might be due to the thermal sensation rather than photobiomodulation (i.e., photon-tissue) interactions. Therefore, it is also essential to measure responses of EEG signals in response to thermal stimulation that is equivalent to the heat produced from tPBM.

Consequently, the tPBM-induced effect under the eyes-closed resting state is unknown, and whether the measured changes in EEG powers could result directly from laser heating is also unclear. However, studies have shown that tPBM improves not only [CCO], but also hemodynamics, especially $\Delta[HbO_2]$ and [ΔHb] in the brain on the stimulation site. However, it is unclear that if the $\Delta[HbO_2]$ increment is limited to the stimulation site. Thus, it is needed to investigate the tPBM evoked $\Delta[HbO_2]$ in the whole head using the LABNIRS system.

1.4 Specific Aims and Dissertation Outline

The scope of my dissertation focuses on utilizing non-invasive brain imaging technologies such as multi-channel whole-head fNIRS and EEG (1) to image decision-making tasks based on Newsvendor Problem (2) to image electrophysiological and hemodynamic response to transcranial photobiomodulation. There are three specific aims, as follows:

Aim 1: To investigate hemodynamic brain imaging in response to a risk decision making task in business content, namely, the newsvendor problem (NP) using a 77-channel fNIRS imager

- Aim 1a: to study and map human brain activations in response to the NP using the general linear model;
- Aim 1b: to explore and quantify dynamic functional connectivity using graph theory by identifying alterations in global and local properties of brain networks in response to the NP.

Aim 2: To investigate and map tPBM and thermal effect on electrophysiological signals, which was administered on the right forehead during the eyes-closed resting state using a 64-channel electroencephalograph (EEG).

- Aim 2a: to quantify and map dose-dependent and frequency-dependent effects of tPBM on whole-head EEG powers of healthy participants during eyes-closed resting state (n=46);
- Aim 2b: to investigate and map time-dependent and frequency-dependent effects of thermal stimulation on whole-head EEG powers of healthy human participants during the eyes-closed resting state (n=14).

Aim 3: To investigate and map whole-head hemodynamic brain imaging in response to right-forehead tPBM during the eyes-closed resting state using the 111-channel fNIRS imager.

- Aim 3a: to study and map whole-head human hemodynamic activations in response to right frontal tPBM (N=19);
- Aim 3b: to explore and quantify dynamic functional connectivity patterns in response to right frontal tPBM (N=19).

Chapter 2

Neural correlates of newsvendor problem-based decision-making in the human brain: An exploratory study to link neuroeconomics with neuroimaging using wide field-of-view fNIRS

(This chapter is a manuscript that has been submitted to Frontiers in Neuroscience)

Hashini Wanniarachchi, Yan Lang, Xinlong Wang, Tyrell Pruitt, Shridhar Nerur, Key Yut Chen, Hanli Liu

2.1 Introduction

Neuroeconomics is an emerging field that integrates economic theories with neuroscience to enhance the understanding of how the human brain makes decisions under different business conditions [23]. The "behavioral perspective in decision-making" is common in business research. For example, studies in management science have found that psychological factors, particularly attitudes towards risks and rewards, are essential drivers of business decisions. In general, business research usually assesses cognitive and psychological processes indirectly via human-subject experiments, surveys, and/or real-world observations. On the other hand, functional neuroimaging is a unique tool that allows researchers to "peek into the black box" and gather data directly from pertinent regions of the brain while subjects are engaged in making a decision. Advanced neuroimaging technologies, such as multi-channel electroencephalography (EEG) and functional magnetic resonance imaging (fMRI), are potentially able to provide clues to the underlying cognitive processes that previously were assumed to be the determinants of human decision-making.

Multi-channel fNIRS is a portable and non-invasive imaging technique that measures cortical hemodynamic activities in the human brain. It quantifies the cerebral concentration changes of

oxygenated hemoglobin (Δ[HbO]) and deoxygenated hemoglobin (Δ[Hb]) with the high temporal resolution based on the alteration of optical absorption and scattering of near-infrared (NIR) light propagating through the human brain. The temporal and spatial features of Δ[HbO] and Δ[Hb] are then used as biomarkers of neuronal activations [24, 25]. In the last two decades, fNIRS has gained popularity and has been recognized as a non-invasive tool to functionally image brain activations and diagnose brain diseases [2, 26]. Compared to fMRI, fNIRS is cost-effective and less sensitive to motion artifacts, has less restriction on body movement or confinement, and has a higher temporal resolution. All these features make it easier to use in a task-oriented, more-naturalistic experimental environment.

In this study, we utilized the newsvendor problem (NP) in our experimental design as NP has been widely used in management science [27]. NP refers to a prevalent business decision-making scenario, where an individual must balance between potential loss and waste to achieve maximum expected profit. The typical scenario is that of a store manager deciding the number of units of products to stock when the number of customers is uncertain [6]. Too little stock leads to potential loss of sales; too much stock leads to potential waste. Risky decisions have to be made when stocking the inventory for profit under arbitrary requirements. While many publications have reported brain activities in response to risk decision-making under varying conditions of risk [7], as far as we know, no inventory management scenarios, such as NP, have been investigated in conjunction with neuroimaging techniques. The specialty of NP is to consider whole business management scenarios, not just one element, for the best decision-making outcome. This study aims to fill this void by mapping human brain activations or deactivations and cortical network changes caused by NP with fNIRS.

Graph theory analysis (GTA) is an analysis method that has been developed to examine large-scale complex brain networks [28-32]. It can provide an easy and yet powerful mathematical means to characterize the topological properties of the brain networks [33-35]. In particular, a few recent studies have combined GTA with channel-wise fNIRS, and have revealed the topological organization and architecture of large-scale, resting-state human brain cortical networks [36-38]. This study also applies GTA to investigate changes in brain network properties when the brain changes from resting state to dynamic task-based activity.

Specifically, to examine brain activities in response to the NP tasks, we formulated two hypotheses: Hypothesis I was that NP stimulates both DLPFC and OFC significantly in the human brain, and that more challenging NP results in the deactivation of right-DLPFC in addition to activation of left-DLPFC. Hypothesis II was that brain network properties would change when a person transits from rest to the NP decision-making phase. To test these two hypotheses, we designed and incorporated the NP protocol using a computer-based platform with simultaneous 77-channel fNIRS data acquisition.

2.2 Material and Methods

2.2.1 Participants

A total of 27 subjects (20 males and 7 females; 23 ± 5 years of age) participated in the study. They were randomly assigned into two experimental groups with different risk levels. The subjects were included in the study if they met the following criteria: belonged to either sex, were from any ethnic background, and were between 18 and 40 years of age. The subjects were excluded if they (1) were diagnosed with a psychiatric disorder, (2) had a history of a neurological condition or severe brain injury or violent behavior, (3) had a history of prior institutionalization or

imprisonment, and (4) were currently under any medicine or drug. The study protocol complied with all applicable federal guidelines and was approved by the institutional review board (IRB) of the University of Texas at Arlington. Informed consent was obtained from every subject who participated in the experiment.

2.2.2 NP Protocol Design

The experimental protocol design was based on the Newsvendor Problem [27], where a news vendor must decide how many newspapers to buy each day at the wholesale price and sell at the retail price. This NP problem has five major characteristics: (1) the demands are uncertain but from a known distribution; (2) the decision must be taken for every period; (3) there is a cost for ordering too many items; (4) the number of items ordered at each time is called order quantity, which must be decided for the inventory by the subject in each trial; and (5) each trial is independent. According to the NP model [2, 6, 39], under the condition that the order quantity (q) is larger than the unknown demand (D), the final profit (π) can be calculated as a function of q and D by Eq. (2-1) [39], as shown below:

$$\pi(q, D) = p \min(q, D) - c\, q \qquad (2\text{-}1)$$

where c is the cost, and p is the price to sell.

Based on the conditions listed above, the experimental protocol was designed with two independent treatments, namely, the high-profit margin (HM) ($c << p$) and low-profit margin (LM), ($c < p$). Table 1 shows the details of the design for the two different treatments used in our study. In the HM treatment, the price to sell, p, was designed to be \$32 while the cost was only \$8, all of which resulted in a lower risk of losing profits. On the other hand, in the low-profit margin (LM) treatment, while keeping p still \$32, the cost was raised to \$24, leading to a higher risk of

losing profits. The demand was kept unknown until the participant made his or her decision by typing the order quantity between 0 and 300 per trial. The given demand was randomly generated from a uniform distribution between 0 to 300 with a mean of 150. The history of demands from previous trials was visible to the participant after each trial, based on which the participant could decide for the current trial. There were 40 trials in total in each experiment. The selling price and cost were kept constant and known for each HM and LM treatment.

Table 1-1 NP Protocol Summary

Treatment	**High-profit Margin (HM)**	**Low-profit Margin (LM)**
Price (p)	$32	$32
Cost (c)	$8	$24
Demand Distribution	Uniform [0 300]	Uniform [0 300]

2.2.3 NP Protocol Implementation

Subjects were randomly divided into either the HM treatment (n=13) or LM treatment (n=14) group before the experiment. One entire experiment consisted of a 30-s baseline and 40 blocks corresponding to 40 trials of NP tasks, as shown in Fig. 2-1a. The 30-s 'baseline' was needed to acquire the baseline of cerebral hemodynamic functions of each subject. Each block contained one NP trial, and each NP trial entailed 4 phases: decision, rest, feedback, and rest. The 'decision' phase lasted for a maximum of 20 seconds, during which each subject was asked to decide on the order quantity given such visible information as price, cost, and demand distribution range for either the HM or LM group. The subject was instructed to enter the quantity in a text box on the screen within the 20-s maximal period. If the subject did not enter anything within the 20 s, the

program automatically determined the order quantity to be ‘0’. In general, decision-making durations were not the same for each subject over the trials.

After the decision phase, the screen shifted to a 5-s 'rest' phase, followed by the 10-s 'feedback' phase. Within this 10-s period, the subject was shown a summary table listing the price, cost, demand distribution, profit/loss, and the cumulative profits/losses that were made after every trial. Then the protocol proceeded to the next trial following another 5-s 'rest' period. All trials of either LM or HM session consisted of the same setting during the decision phase. All the profit/loss details were stored along with the corresponding time stamps.

The NP trials were presented on a laptop computer in the form of a game. The subjects were directed to use both hands during the experiment, one hand to press the spacebar on the keyboard for making an event stamp for fNIRS, and the other to enter the order quantity for the corresponding trial. Before each experiment, each subject was provided information on how to play the NP game and given a 5-trial practice session to get familiar with the experimental protocol.

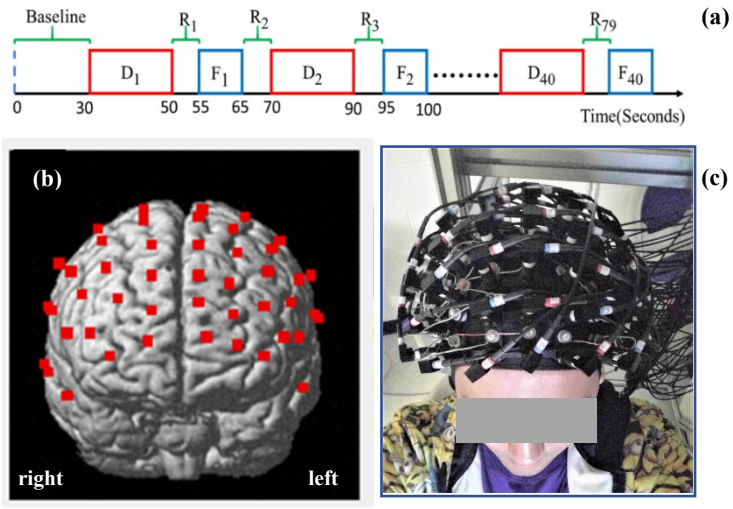

Figure 2-1: Experimental protocol and setup. (a) The NP experimental protocol consists of a 30-s initial baseline and 40 trials. Each trial has 4 phases: up to 20-s NP decision task (Di), 5-s rest (R2i-1), 10-s feedback (Fi), and 5-s rest (R2i) again before starting another block/trial for the Di+1 trial.

(where i = 1, 2, 3, …, 40) Each block lasts about 30-40 seconds. (b) The front view of the channel layout of fNIRS optodes on a human brain template with 77 channels derived from 25 pairs of light sources and 23 detectors. The red squares illustrate the channel locations for 77 channels. (c) The experimental setup for the NP experiment. The subject wears the whole-head cap, with a 77-channel layout hooked up to the LABNIRS system while maintaining seated on an upright position.

2.2.4 fNIRS Experiments

A continuous-wave, multi-channel fNIRS system (LABNIRS, Shimadzu Corp., Kyoto, Japan) was employed in this study. As reported before [40], a customized, wide field-of-view, 77-channel layout incorporating 25 sets of laser transmitters and 23 light receivers was used to cover from the prefrontal cortex to the sensorimotor cortex. Fig. 2-1b shows the front view of wide field-of-view, 77-channel locations on a human brain template, while Fig. 2-1c is a photo viewing a human subject wearing a whole-head helmet that facilitates all-optical optodes connected to the LABNIRS data collection system. The distance between the nearest source and detector fiber optodes was 3 cm, resulting in a sensitive detection depth of 1.5-2 cm under the scalp. All the source and detector fibers were firmly and steadily held by the helmet on each subject's head; the data sampling frequency was 12.82 Hz. Spatial co-registration measurements were taken using a 3D digitizer (FASTRACK, Polhemus, Colchester, VT, USA).

2.2.5 Data Analysis

2.2.5.1 Behavioral Analysis

The NP protocol generated two types of behavioral scores: (1) the decision-making (reaction) time and (2) the profit/loss score that each subject made for each trial. These two parameters were averaged across 40 trials for each subject for each of HM (n=13) and LM (n=14) groups. Then, the grand-averaged reaction time and profit score over each group were quantified and pooled with

box plots to quantify their respective distributions. Statistical testing was next performed using a two-sample t-test for both averaged reaction time and profit score to identify a significant difference between the HM and LM groups.

2.2.5.2 fNIRS Data Processing

The raw outputs of the fNIRS system were time-dependent optical intensities at three wavelengths (i.e. 780 nm, 805 nm, and 830 nm), the alterations of which were affected by the changes of hemoglobin concentrations. A band-pass filter of 0.01 - 0.2 Hz was applied to remove artifacts from cardiac pulses (~0.8-1.2 Hz), respiration (~ 0.2 - 0.3 Hz) [41], muscle movements, and systemic drifts. Next, the modified Beer-Lambert Law was used to convert the recorded optical intensities at 780 nm and 830 nm into concentration changes of oxygenated hemoglobin (Δ[HbO]) and deoxygenated hemoglobin(Δ[Hb]) [24, 42]. Then, each time series of Δ[HbO] and Δ[Hb] was baseline calibrated by subtracting its temporal average to remove any potential drift during the baseline recording. Moreover, to further remove systemic, physiological variations contained in the scalp and skull, we subtracted the signal spatially averaged across all 77 channels to remove the global noise [40]. Also, the channels close to the superficial temporal artery were excluded from the analysis to prevent signal mixing with patterns from arteries [43-45]. Afterward, the pre-processed data was used for further analysis. The data analysis was performed in two steps: (1) NP-evoked Δ[HbO] activations based on a general linear model (GLM) and (2) NP-evoked alterations in brain connectivity based on GTA.

2.2.5.3 Activation Maps-Based on the General Linear Model

GLM is a mathematical model popularly applied in fMRI [46, 47] and fNIRS [48, 49] to estimate amplitudes of hemodynamic activation or deactivation at different brain regions in response to a

variety of tasks. In our study, a preprocessed time series of Δ[HbO] per channel was used as the input in the GLM analysis using MATLAB. In the process, the designed temporal matrix was generated with a boxcar function, reflecting the NP task blocks convoluted with a canonical hemodynamic response function (HRF) [50]. For each NP experiment (with HM or LM treatment), two regressors were generated corresponding to the decision phase and feedback phase, while the data analysis was mainly focused on the decision phase. Eq. (2-2) demonstrates the model equation for the GLM model developed based on the experiment. 'y' is the time series; x_1 and x_2 represent the model response functions or design matrices corresponding to the decision phase and feedback phase; β_1 and β_2 are the amplitudes of Δ[HbO] corresponding to the decision and feedback phases, respectively; 'e' is the error term.

$$y = \beta_1 x_1 + \beta_2 x_2 + e \qquad (2\text{-}2)$$

Following the model, the activation amplitudes (i.e., β_1 and β_2 values) for both regressors were calculated or fitted through a regression algorithm between the calculated Δ[HbO] time series and the temporal design matrix using a weighted least square method [48]. Such regression processes were carried out for each channel, giving rise to an array of 77 fitted beta values relative to their baselines for each human subject. However, only beta values corresponding to the decision phase were considered for further exploration in this paper.

Next, beta values were averaged across the subjects to observe the activation as a response to decision-making under NP. Further, the beta values were used to perform statistical analysis exploiting one-sample or two-sample t-tests to test our hypothesis I. Specifically; we wanted to investigate (1) whether DLPFC and/or OFC were significantly evoked by NP versus baseline regardless of treatment (HM or LM) types, (2) whether DLPFC and/or OFC were activated by HM or by LM versus baseline, and (3) whether a more challenging NP created a significant difference

in brain activation or deactivation in DLPFC or OFC regions. For test (1), one-sample t-tests (against the mean of zero baselines) were performed over beta values of Δ[HbO] from all 27 subjects for each of the 77 channels, without considering any treatment effect. This step allowed us to map/identify significant cerebral activation/deactivation regions (i.e., channels) while the subjects made risky NP decisions. For test (2), beta values of Δ[HbO] were analyzed for subjects separately with either LM or HM treatment, respectively. Similarly, one-sample t-tests were performed among 13 participants with HM treatment and separately among 14 participants with LM, at each channel to examine the statistical significance versus the mean of zero baselines. For test (3), two-sample t-tests were performed at each channel between the two groups (with HM and LM treatments) to determine significant differences in brain activation/deactivation. All activation related statistical tests were performed at a significance level of $\alpha=0.05$. Accordingly, topographic t-value maps were generated using easytopo 2.0 [51].

2.2.5.4 Applying GTA to Assess Network Properties in the Brain

Graph theory is a renowned mathematical model to study characteristics of a network system [52, 53], and it has been applied to investigate resting state functional connectivity of the human brain as measured with fMRI, Electroencephalography (EEG), and Magnetoencephalographic (MEG) [54-57], as well as fNIRS [36-38]. A recent study demonstrated that based on GTA, brain networks were altered when the human brain transitioned from resting state to task-evoked states [58]. In this study, we also applied GTA to primarily focus on how brain networks were altered from the resting state to the decision-making state in a dynamic context.

Our analysis based on GTA was performed following similar steps to those in refs. [36-38, 59], as follows: (1) The processed Δ[HbO] time series for all channels were analyzed to create Pearson's correlation coefficient (PCC) matrices in the rest and decision-making phases. Only

positive correlations were considered for calculations. Nodes were defined as channels, and edges were defined as normalized Pearson's correlation strength. The longer the data, the less specific the task-based data is. (2) Rest and decision periods of three trials (See Fig. 2-1(a)) were extracted and concatenated into two-time series separately. (3) A three-trial moving window overlapping one trial was applied to create multiple concatenated time series, which resulted in multiple PCC matrices for both rest and decision phases, respectively. Only the first 20 trials were included for the connectivity calculations to avoid impacts from fatigue and stress. (4) The PCC matrices for all concatenated time series were converted to z-values by Fisher's r-to-z transformation to improve normality, resulting in a 77 × 77 z-value functional connectivity matrix Zij for each subject, where i, j = 1, 2, … 77. (5) All three-trial-derived, Fisher-transformed Z matrices were averaged to become two respective matrices for both rest and task phases for each subject. (6) These two matrices were entered as inputs in GRaph thEoreTical Network Analysis (GRETNA) [60] to construct the functional brain network for each subject. (7) Within GRETNA, we chose the sparsity, S, as the threshold criterion, the number of current existing edges divided by the total possible number of edges in the current matrix in a network.

We selected and quantified five global topological properties/metrics to study network patterns with a range of S level (S; $0.05 < S < 0.50$; increment = 0.05) [61], as follows: (1) global efficiency (Eg) that represents global efficiency of the subgraph composed of the nearest neighbors of the node; (2) local efficiency (Eloc) that describes how efficient the communication is between the first neighbors of i when i is removed; (3) clustering coefficient (Cp) that measures network segregation; (4) path length (Lp) that is the average of the shortest path length between all pairs of nodes; (5) small worldness (σ) that reflects small-world characters and is characterized by a high

C_p and low L_p. Detailed definitions and explanations on these network metrics can be found in ref. [59].

All seven steps were repeatedly performed on all 27 subjects, followed by statistical comparisons for each of the five network-metrics within $0.05 < S < 0.50$ (i) between the rest versus decision-making regardless of LM or HM and (ii) between LM and HM.

2.3 Results

2.3.1 Behavioral Results

When the subjects played NP games, their profit/loss score and the reaction time per trial were recorded, so were the total scores and average decision-making times overall 20 trials. The corresponding results for both LM and HM groups are shown in Fig. 2-2. Fig. 2-2a shows that the mean profit averaged over the LM group was less than zero ($-198.27), whereas the HM group gained a mean yield of $2,183.50 during each trial, with a significant difference in profit between the two groups by a two-sample t-test. Fig. 2-2b shows that the subjects under the LM protocol spent an average of 9.6 seconds to make the risk decision while the HM group needed an average of 8.25 seconds to complete the task, which was not significantly different by the two-sample t-test. These observations were expected because risky decisions under the HM protocol were more straightforward and quicker to make while gaining good profit, as compared to the LM treatment.

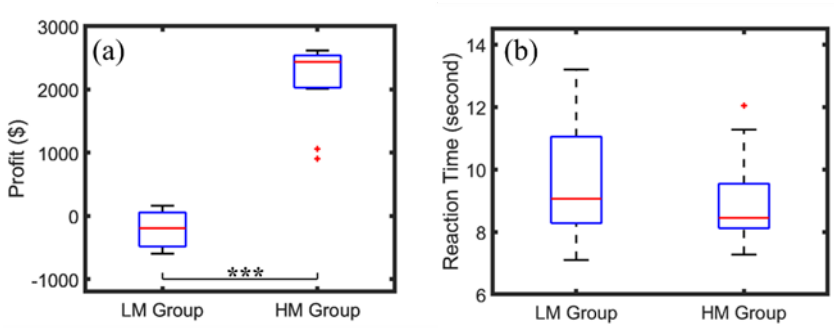

Figure 2-2. Behavioral scores distribution of (a) average of profit and (b) average reaction or decision-making time in response to LM and HM protocols. '***' indicates the statistical significance between LM and HM at $p < 0.001$ ($p=1.915\times10^{-13}$). The reaction time did not show a significant difference. Outliers are marked as '+'.

2.3.2 Brain activation evoked by NP determined with GLM

As a result of GLM analysis, the group averaged β_1 values and their statistical t-values were generated based on the hemodynamic changes, Δ[HbO] when subjects performed the NP-based tasks. These statistical tests aided us in identifying significantly activated locations on the cortex in response to the decision-making task. Three statistical analyses were performed to test: (1) whether DLPFC and OFC were significantly evoked by the NP with respect to the baseline regardless of treatment (HM or LM) types; (2) whether DLPFC and/or OFC were activated by HM or LM versus baseline; and (3) whether more challenging NP tasks (i.e., LM) created a significant difference in brain activation or deactivation in DLPFC and/or OFC regions with respect to less challenging NP conditions.

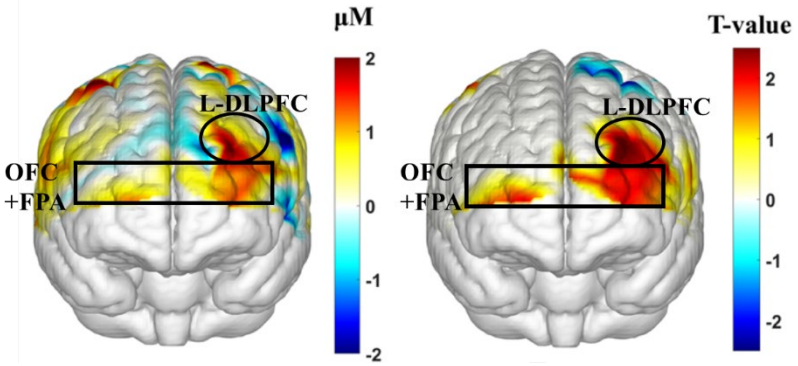

Figure 2-3. Topographic maps in response to brain stimulations by the 40-trial NP from all subjects (n=27) without considering the treatment level**.** (a) Averaged topographic beta, β1, map (in μM) derived from Δ[HbO] during the decision-making phase. (b) Corresponding t-map derived from a one-sample t-test at a significance level of $p < 0.1$ for a two-tailed t-test.

We obtained the front view of a topographic Δ[HbO]-derived beta map shown in Fig. 2-3a averaging over 20 decision-making trials from all 27 human subjects regardless of either HM or LM treatment. The topographic map illustrates activated cortical areas identified by the output of NIRS_SPM [62] corresponding to the co-registration readings. Fig. 2-3b presents the corresponding t-map to compare Δ[HbO] signals between the decision phase and baseline with a one-sample t-test. These observations suggest that NP tasks considerably activated left the DLPFC (l-DLPFC) and OFC and front polar cortex (FPC) on both hemispheres. Also, some deactivation is noted in the left supplementary motor area (SMA).

Next, Figs. 2-4(a)-4(c) show front-view t-maps of Δ[HbO] evoked by the NP tasks under three comparison conditions. Fig. 2-4(a) illustrates that the NP decision-making with HM treatment significantly activated OFC on both hemispheres and l-DLPFC. Fig. 2-4(b) demonstrates unambiguously that the NP decision-making with LM strongly activated the l-DLPFC and Broca's area, but not OFC. Moreover, LM tasks deactivated the right DLPFC (r-DLPFC). Finally, Fig. 4(c) shows a topographic t-map obtained by a two-sample t-test between Δ[HbO] values under LM and HM treatment. It is seen that more challenging NP with LM dominated significant deactivation in r-DLPFC and significant activation in left Broca's area compared to the NP tasks with HM risk-taking. All of these observations supported our Hypothesis I that NP stimulates both DLPFC and

OFC significantly in the human brain, and that more challenging NP results in the deactivation of right-DLPFC in addition to activation of left-DLPFC.

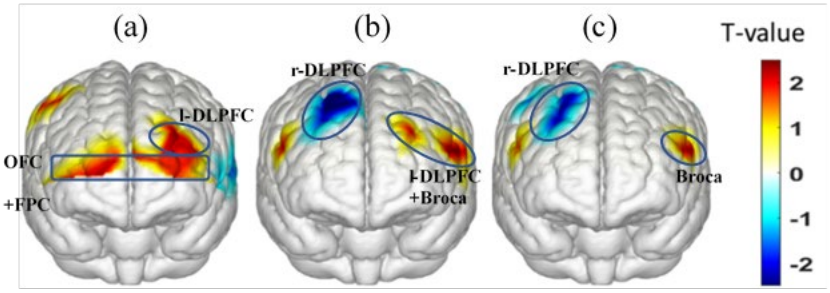

Figure 2-4 Front-view topographic t-maps of Δ[HbO] evoked by the NP. (a) HM treatment (n=14) compared to baseline; (b) LM treatment (n=13) compared to baseline. One-sample t-tests were performed comparing each treatment relative to the baseline. (c) shows a front-view topographic t-map comparing activation/deactivation between LM and HM tasks based derived from the two-sample t-test at a significance level of $p < 0.1$ for a two-tailed t-test.

2.3.3 Brain network changes induced by NP analyzed by GTA

NP-induced changes in brain network properties during the resting and decision phases were obtained based on GTA, yielding five global network properties: global efficiency (Eg), local efficiency (Eloc), clustering coefficient (Cp), path length (Lp), and small-worldness (sigma (σ)) for sparsity between 0.05-0.5. Consequently, Fig. 2-5 illustrates the network properties for each parameter averaged over all subjects (n=27) for the two phases. Fig. 2-5 shows that the NP tasks significantly reduced Eg, but increased Eloc, Cp, and Lp as compared to rest for almost all of the sparsity range (0.05-0.4 thresholds). Even though σ (Fig. 2-5(e)) does not show a significant difference between the phases, both of them show small-worldness maintaining $\sigma > 1$ [52-54], holding characteristic behaviors of small-world networks

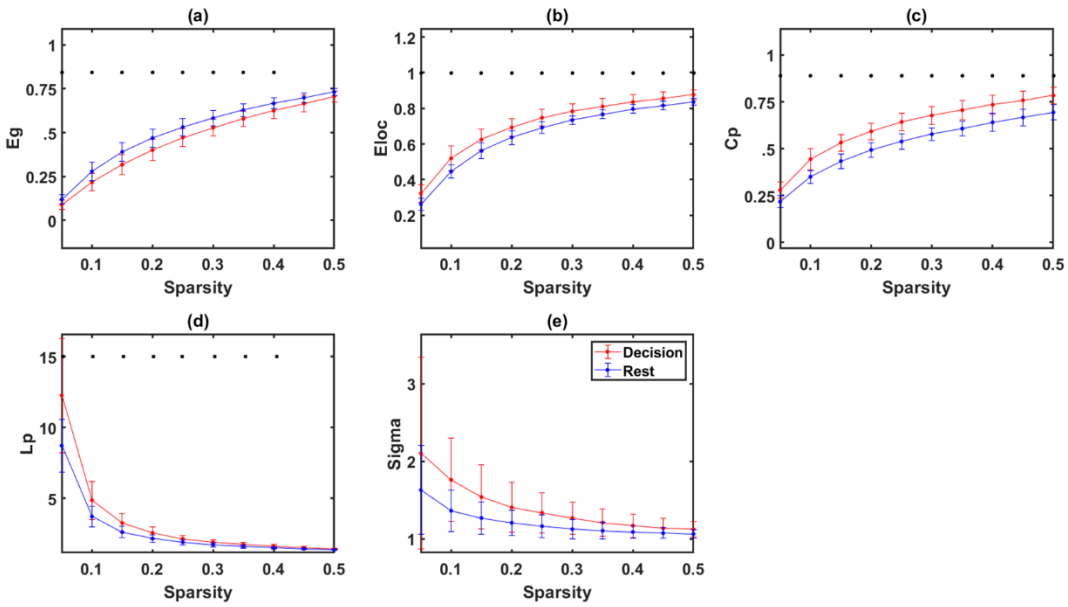

Figure 2-5 Comparison of averaged dynamic functional network properties derived from GTA during NP decision (red) and rest (blue) phases for all subjects (n=27): (a) Eg, (b) Eloc, (c) Cp, (d) Lp, and (e) sigma. Sparsity ranges from 0.05-0.5. Significant differences of each network property at respective sparsity between the NP decision and rest phases are marked by * on the top of each panel. The error bars represent the standard deviation. The statistical significance was set to be at $p < 0.01$.

Furthermore, the five network properties were separately quantified for the LM group (n=14) and HM group (n=13), as shown in Fig. 2-6 with similar parameter settings to those in Fig. 2-5. It is seen that both the LM and HM groups fundamentally followed the same patterns as those in Fig. 2-5 derived from both groups together. On closer inspection on these figures, we observed that (1) both groups had significant increases in Cp across all the sparsity range as compared to the rest phase, (2) the LM group had significant increases in Eloc with more sparsity numbers than the HM group, but (3) the HM group had significant decreases/increases in Eg/Lp, respectively, with more sparsity numbers than the LM. (4) In particular, the LM group exhibited significant increases in σ during the NP task phase versus the rest phase at several sparsity levels. In contrast, the HM group did not reveal such features.

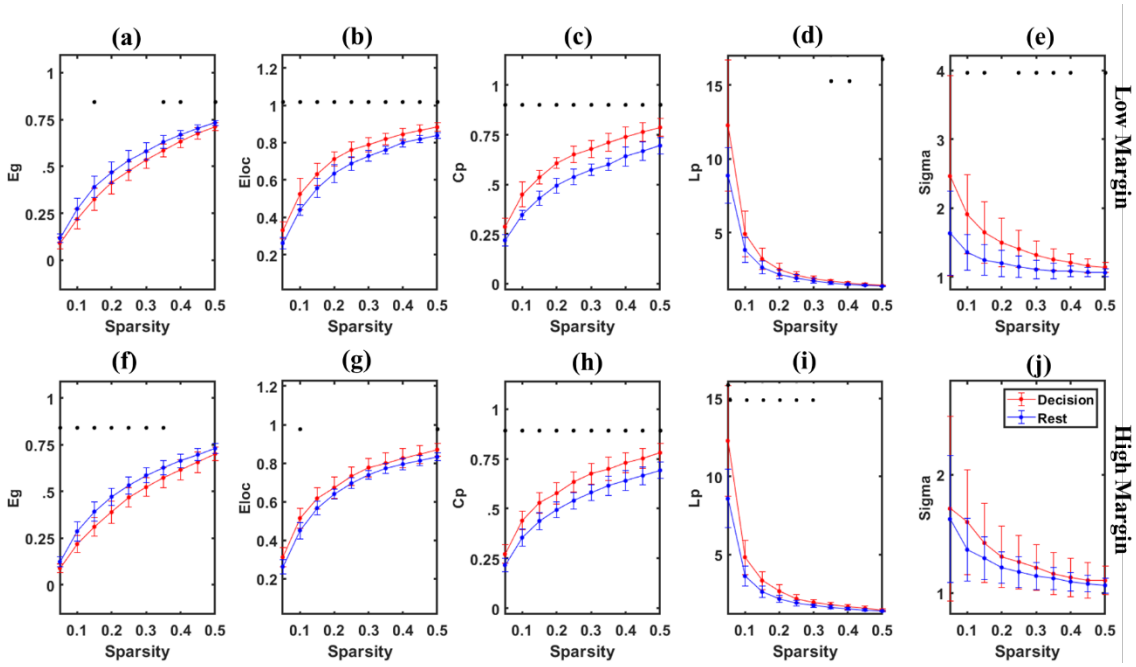

Figure 2-6 Brain network properties for LM (N=14) and HM (N=13) for the rest phase (red) and the decision phase (blue). Network efficiency parameters for LM (top row (a-e)) and HM (bottom row (f-j)) such that Global efficiency (Eg), local efficiency (Eloc) indicate in (a-b) and (f-g), respectively. Small-world property parameters such that the Clustering coefficient (Cp), Path length (Lp), and small worldness (sigma) indicate in (c-e) and (h-j), respectively. Sparsity ranges from 0.05-0.5 for every 0.05. The sparsity levels having significantly different decision versus rest network properties, are marked in black stars. The error bar represents the standard deviation. The statistical significance is calculated at $p < 0.01$.

In summary, Figs. 2-5 and 2-6 illustrate that the brain network properties were altered when the human brain switched from rest to the NP decision-making phase, particularly during the higher risk levels. The clustering coefficient, Cp, was significantly enhanced under both high- and low- risk decision-making. At the same time, the higher risk decision-making significantly boosted the small-worldness, σ, of the brain. All the results shown in this subsection strongly supported Hypothesis II, which posited that brain network properties would be altered when a person transitions from rest to the NP decision-making phase.

2.4 Discussion

In a complex and turbulent business environment, managers must make decisions that require complex trade-offs and risk considerations. Decision-making under risk is a complex cognitive process, requiring contribution and integration of actions from multiple regions of the human brain [63-65]. The scope of this study was to observe which cortical regions of the human brain are responsible for making risky decisions in a business context, as represented by the widely studied newsvendor problem (NP). The first hypothesis was that NP stimulates both DLPFC and OFC significantly in the human brain and that more challenging NP with LM treatment triggers more deactivation in DLPFC than HM treatment. The second hypothesis was that brain network properties show significant alterations when the human brain switched from a rest state to the NP decision phase. To prove these hypotheses, we conducted 77-channel, wide field-of-view fNIRS measurements from 27 human subjects concurrently when they performed NP decision-making tasks. After data analyses and reviews of results, we have learned several valuable lessons and gained scientific findings, as discussed as follows.

2.4.1 Behavioral Outcomes Affected by NP Decision-Making Tasks

The behavioral scores (Fig. 2-2) revealed how NP tasks with HM and LM affected subjects' performance in average profits and average decision-making time. During the LM treatment, it was difficult to earn positive rewards while the LM group took about the same time as the HM group to make the decision. In contrast, the HM group received much better and significant profits. These observations may imply that the subjects facing the LM challenge were under much more stress than those under the HM condition since the former group had to think much harder and more carefully for making risky decisions to win profits with challenging circumstances and limited time.

2.4.2 Brain Activation Triggerd by NP Decision-Making Tasks

Our results (Fig. 2-3) confirmed that both DLPFC and OFC regions, particularly l-DLPFC, played significant and critical roles in cognitive processing when subjects had to solve the NP regardless of difficulty levels. Several previous studies in the literature have reported that DLPFC is responsible for risky decision-making (in non-business context) and cognitive control in terms of planning and working memory [9, 25, 66, 67]. Our findings in this paper are consistent with those reported. Another significantly activated area observed in this study was the front polar area (i.e., BA10), which is another crucial part of the brain involving executive functions. Even though it is not a part of the reward pathway, there is evidence of its contribution to decision-making.

Moreover, a slight deactivation is observed in the left anterior temporal lobe. One of the studies comparing brain activation on fMRI-based semantic and non-semantic tasks has shown deactivation in the left anterior temporal lobe in response to non-semantic tasks while semantic tasks triggered activation. Also, left-lateralized activation is closely related to scripted words or generating speech. Our study was more related to a non-semantic aspect. Therefore, the deactivation observed in the l-temporal lobe can be attributed to the comprehension of written words when reading NP questions [68, 69].

2.4.3 Brain Activation by Low Risk (HM) NP Tasks

It is seen (Fig. 2-4(a)) that the HM group presented prominent and significant activation in l-DLPFC when making low-risk NP decisions. This protocol scenario would be similar to a goal-oriented decision-making in a less risky environment. Our observation on l-DLPFC is consistent with a few published reports. In an fMRI-based study where the subjects were given the task of "Tower of London," a popular protocol based on planning, it was observed that the left DLPFC

was significantly activated during the hierarchical goal state [70]. Another study reported significant DLPFC stimulations when the subjects decided to execute a right-hand movement to enter the order quantity on the computer keyboard [71]. Furthermore, we observed that OFC was activated during the HM NP tasks. Since OFC is suggested to be one of the significant components in the reward pathway [72], the activation of OFC explains the anticipation for gains during the trials.

2.4.4 Brain Activation by High Risk (LM) NP Tasks

Compared to HM stimulation, several distinct features of the brain responses to LM stimulation (Fig. 2-4(b)) are noted: (1) strong activation in left Broca's area, (2) significant deactivation in r-DLPFC, and (3) no activation/deactivation in OFC. This set of tasks were more challenging than those in HM, so the subjects needed to pay more attention to the tasks and to control their emotions during the tasks. Since Broca's area has a function of modulating emotional response besides the language process, it is reasonable to observe strong activation in this cortical area in response to the LM tasks. Also, the observed r-DLPFC deactivation may be attributed to the intense stress due to more difficult decision-making challenges [73, 74]. OFC is expected to have a strong response in this case because OFC plays a key role in decision-making involving reward, but we did not observe such activations in OFC. A plausible reason for this finding is that, as the more challenging NP tasks shifted the subjects' attention from a less-stressful reward phase to a more-stressful defying phase, the brain activations occurred in DLPFC rather than in OFC.

2.4.5 Comparing High Risk (LM) Versus Low Risk (HM) Brain Activation

Consequently, to be more rigorous in testing for significant differences between brain responses to LM and HM treatment, two-sample t-tests were performed. The results (Fig. 2-4(c)) confirmed

that LM tasks triggered (1) significant activation in Broca's area and (2) significant deactivation in r-DLPFC. The reason for the former observation was mentioned above; namely, Broca's area has a function of modulating emotional response. The latter observation was consistent with the results reported in several recent publications. For example, an fMRI study involving 27 subjects suggested that deactivation in r-DLPFC may occur due to acute stress, which weakens high-level cognitive functions such as working memory [75]. Also, a transcranial direct current stimulation (tDCS) based study with 120 participants showed that tDCS delivered on the r-DLPFC could prevent stress-induced working memory deficits [73, 74]. In our study, the NP with the LM protocol was somewhat risky and a bit lengthy, subjecting the participants to higher levels of stress. Consequently, we observed clear and significant deactivation in r-DLPEC only during LM tasks.

2.4.6 Brain Network Alteration Caused by NP Decision-Making

Our GTA-derived network properties (Fig. 2-5) demonstrated that regardless of difficulty levels, NP-evoked decision-making tasks altered global brain network properties of the human brain from those at rest. The observation of decreases in Eg (in sparsity range of 0.05-0.4) and increases in Eloc (in sparsity range of 0.05-0.5) caused by NP indicates that NP stimulated sub-region connections in the brain more locally, not globally. This observation also implies that more communications among regional segregations take place to achieve the decision-making tasks. Also, increases in both Cp (in sparsity range of 0.05-0.5) and Lp (in sparsity range of 0.05-0.4) by NP reveal that NP decision-making needs the brain to boost or enhance network segregation, which also leads to an increase of Lp and Eloc consistently [58]. As evidence, the activation maps of Δ[HbO] (Fig. 2-3) illustrate that only several cortical regions (i.e., DLPFC, OFC, and FPA) were involved in the decision-making process, regardless of either LM or HM treatment. These results support indirectly the underlying reasoning of enhanced Eloc and Cp during NP tasks.

2.4.7 Brain Network Alteration Caused by NP Tasks with HM and LM

The first observation from Fig. 2-6 was that the LM group had significant increases in Eloc with a broader sparsity range (0.05-0.5) than the HM group (at only sparsity=0.1 and 0.5). It can be interpreted using the argument similar to that given in Section 4.6: The brain needs sub-regions to work more efficiently and with better communications among themselves to complete a more difficult task (i.e., under LM task) than an easier one (i.e., under HM task). The second observation that the HM group had significant increases in Eg and Lp with more sparsity numbers (0.05-0.3) than the LM is consistent with the observation without separating HM and LM groups (0.05-0.4; shown in Fig. 2-5). The third observation that the LM group exhibited significant increases in σ during the task phase versus the rest phase (sparsity range=0.1-0.5) is particularly intriguing and can be explained as follows. It implies that more challenging NP tasks would require a more significant small-worldness organization of the brain networks. Such a network organization is more efficient in the local information processing needed for high-risk NP tasks when compared to more manageable or lower-risk decision-making tasks. This interpretation is supported indirectly by the brain activation map shown in Fig. 2-4(c), which exhibits localized cortical regions that were significantly stimulated by the LM (high risk) NP tasks.

2.4.8 Limitations of the Study and Future Work

First, even though the focused and detected areas of brain activation by NP were DLPFC, OFC, and FPA at the cortical level, multiple other brain regions beyond the cortex were involved in the complex NP decision-making processes but challenging to have access by fNIRS. Second, since the 27 subjects had to be split into LM and HM groups, each sample size was statistically small. It is appropriate in future studies to corroborate the findings of this study with larger sample size. Third, the brain network properties or metrics were obtained using PCC with a relatively short

period of time for both rest (~ 15 sec) and NP (~ maximum of 60 sec) task phases. Such a short period is perhaps not adequate to provide stable or physiologically meaningful results [76]. More rigorous and appropriate algorithms for quantifying dynamic functional connectivity of the human brain at both rest and task-evoked phases need to be further explored and applied for this study in the near future.

2.5 Conclusion

In conclusion, this study showed that NP-based decision-making stimulated vital brain areas, such as DLPFC and OFC, for high-level cognitive functions based on 77-channel, wide field-of-view, hemodynamic measurements with fNIRS from 27 human control subjects. The study observed that there were multiple regions activated and deactivated in responses to the tasks. Explicitly, DLPFC and OFC were significantly evoked by NP tasks versus baseline regardless of treatment types. Significant deactivation in r-DLPFC was observed and attributed to the challenging stress created by the LM with respect to HM. Furthermore, NP decision-making altered global brain network properties from the resting phase such that Eloc, Cp, and Lp were all increased while Eg was reduced. Also, high-risk LM tasks triggered more significant small-worldness organization of the brain networks than the low-risk tasks. All these alterations in network properties together enhanced better communications among sub-regions or local segmentations to achieve more difficult LM tasks. Overall, this study supported our hypotheses: (1) that NP stimulates both DLPFC and OFC significantly in the human brain, and that more challenging NP results in the deactivation of right-DLPFC in addition to activation of left-DLPFC, and (2) that brain network properties are altered when a person transits from rest to the NP decision-making phase.

2.6 Further Discussion Remarks

2.6.1 Graph Theory Thresholding

GTA is performed upon a thresholding algorithm. The thresholding is required to avoid misleading effects of specious interactions among regions in the connectivity matrices. Network sparsity is one of the methods applied in thresholding. Network sparsity is defined as the ratio between the number of actual edges to the maximum possible number of edges for each network. However, when the number of nodes is equal in several networks, the sparsity threshold confirms the equal number of edges for each network by using a subject-specific connectivity potency threshold. Thus, it permits an investigation of relative network organization. However, during a situation where it is difficult to define a single threshold, the researchers can define a range of thresholds to calculate network properties. Moreover, the sparsity can also be described as the portion of connections engaged from the full network; thus, setting a sparsity level of 0.3 interprets as that only the top 30% of links are concerned for calculations [33, 60, 77].

2.6.2 Dynamic Functional Connectivity Aspect of GTA

The connectivity analysis used for this study is based on a dynamic functional connectivity approach. The duration, which has been considered for dynamic functional connectivity, ranges from 30 seconds to 120 seconds for calculating each connectivity matrix [78, 79]. In my study, the duration of the interval of decisions was a minimum of 30 seconds. Therefore, when the connectivity matrices are generated, they are aimed to study using a dynamic functional connectivity approach.

2.6.3 Limitations and Future Work

There are several limitations to this work. One of the notable limitations of this study is the penetration depth of fNIRS. According to the literature, decision making involves several internal

structures in the brain, such as ACC, striatum, and medial prefrontal cortex. However, fNIRS only can measure up to several centimeters from the scalp. For example, using our system, the maximum penetration depth is approximately 1.5 cm, given that source-detector separation is 3 cm.

Moreover, even though the sample size for all decisions (N=27) is relatively sufficient when the data was analyzed under marginal conditions, the sample size is relatively small. In contrast, LM consisted of 14 subjects, and HM consisted of 13 subjects. One of the concerns related to connectivity analysis is determining nodes. Channels do not represent one point; instead, it covers an area of the cortex. These areas can be shared with nearby channels as well. Therefore, it can cause interaction effects. Thus, it is challenging to define perfect nodes for the analysis.

Further, among the network properties, there are many global and nodal level parameters to be studied. Global parameters majorly provide (a) information about functional separation and (b) functional incorporation of information flows within the brain network, (c) small-worldness, and (d) network resistance against failure, which we discussed in the analysis [80, 81]. However, the local parameters focus on identifying hubs in the network. Hubs are the nodes with high nodal centrality. It allows them to influence the network topology significantly. There are two types of network hubs. They are known as the connectors or provincials, created upon the high or low participation coefficient defined for them. Connector hubs are inclined to integrate nodes between different segments. The regional hubs are responsible for linking nodes in the same module. To assess the connectors and provincials, the degree of centrality and betweenness centrality can be calculated. The degree of centrality refers to the number of edges a node has. The higher the degree is, the more crucial the node is. This degree measurement can be a useful measure since many nodes with high degrees also have high centrality [82]. Further, betweenness centrality measures

the nodes which act as bridges between higher nodal degreed nodes. These nodes are often useful in identifying the most central nodes [83]. These nodal parameters are helpful in identifying short- and long-distance connections in the brain networks.

Additionally, the second primary phase of the protocol is the ‘Feedback’ phase. During the feedback phase, the subject is shown what he or she earned or lost during the current trial, as well as the previous trials. Also, this phase allows the subject to assess the decision they made in the last trials. However, this phase helps determine a positive gain or negative gain in the next trials. However, since the demand is randomly generated, the decision may also not be affected by the feedback phase of the previous trial. It is worth learning the hemodynamic response in this phase.

Chapter 3

Transcranial photobiomodulation effects on large-scale brain oscillations by 1064-nm laser and its association thermal influence

(This Chapter is a manuscript that will be submitted soon)

Hashini Wanniarachchi, Xinlong Wang, Anqi Wu, Hanli Liu

3.1 Introduction

Photobiomodulation (PBM), also known as low-level laser therapy (LLLT) in clinical applications, is a technique that utilizes red to near-infrared (NIR) light to stimulate mitochondrial respiration functions in a wide range of cells and nerves in the human body [17, 84, 85]. Transcranial photobiomodulation (tPBM) is an approach to deliver NIR laser to the human brains, which has shown promising outcomes in treating psychiatric and neurological brain disorders such as depression, anxiety [86], and traumatic brain injuries [18, 87, 88]. Furthermore, recent studies have shown that tPBM using a 1064-nm laser can be applied to improve cognitive functions on healthy brains. This noninvasive optical neuromodulation tool has been reported to enhance human cognitive performance on a variety of cognitive tasks using sham-controlled experiments with about 300 human subjects [10-13].

Our previous studies have objectively measured and observed significantly enhanced concentrations of hemoglobin oxygenation (HbO) and oxidized cytochrome-c-oxidase (CCO) during and after tPBM on human right frontal-cortex with high reproducibility and robustness to understand and interpret the beneficial mechanism of tPBM to the human brain and to understand the physiological mechanism of tPBM in enhancing cognitive functions, [14, 15, 89]. These investigations validated the hypothesized-theory/mechanism that tPBM can photo-oxidize CCO,

the key mitochondrial enzyme for oxygen metabolism, to boost the metabolic activities of cells/neurons [17]. Also, we reported that thermal stimulation created hemodynamic and metabolic effects opposite to tPBM (i.e., laser illumination), which suggested that the increased hemodynamic oxygenation and metabolic activities were not due to the thermal (warm sensation) effects from tPBM [90].

Recently, tPBM was reported effective in enhancing the powers of large-scale alpha and beta oscillations in the human brain during eyes-opened resting state, measured by scalp EEG on the healthy human brain [16, 19]. This observation indicated that tPBM not only increased oxygenation and the metabolism rate of neurons but also enhanced the firing rate of neurons and connectivity of the brain. Although with different experimental protocols, these findings showed great consistency with many independent studies on EEG responses to tPBM from other research groups [20, 21, 91].

However, it is known that: eyes-open and eyes-closed EEG produce distinctively different results in the human brain [22]. Also, the powers of brain EEG signals are more vulnerable to eye-blinks and drowsiness in the eyes-open resting state compared to the eyes-closed resting state. This emphasizes the essence of measuring tPBM-induced power changes of brain oscillation during the eyes-closed human resting state. Moreover, we observed that the 1064-nm laser beam used for conducting tPBM also produces a warm sensation on the subject's forehead. Because the EEG signal is sensitive to thermal phenomena [92], the warmness created by the 1064-nm laser-illumination during tPBM can potentially affect the EEG signals. Thus, the improvement of behavioral performances and EEG power we observed in previous studies might be due to a mixture of dual-modal effects from thermal sensations and photobiomodulation (i.e., photon–tissue interactions) caused by the tPBM laser-illumination. Therefore, it is also essential to measure

the responses of EEG signals to thermal stimulation that is equivalent to the heat produced from the laser illumination during tPBM, which can help in purifying the absolute photobiomodulation (i.e., tissue–photon interactions) effects of tPBM on human electrophysiology.

In this study, we non-invasively collected scalp EEG signals before, during, and after tPBM (i.e., 1064-nm laser illumination) under the eyes-closed human resting state using the same experimental protocol to our previous studies [10, 16, 85, 93]. Additionally, we measured/calibrated the temperature increment induced by the tPBM laser-illumination on the human scalp. Then, we recorded additional sets of scalp EEG signals before, during, and after the corresponding thermal stimulation using the same experimental protocol. Both the tPBM and thermal experiments followed a sham-controlled protocol. The EEG power alterations induced respectively by sham-controlled tPBM -laser -illumination and the sham-controlled thermal stimulation were computed, followed by statistical comparisons between them. The result showed that - 1) compared to the sham, a significant increase of EEG power in alpha and beta bands was induced by tPBM laser-illumination; 2) compared to the sham of the thermal experiment, thermal stimulation decreased alpha and beta EEG powers, which was the opposite to sham-controlled tPBM effects; and (3) with thermal-effects calibrated/subtracted, the absolute thermal-excluded neuromodulation effects of tPBM were observed as globally enhanced alpha and beta powers. These observations suggested that tPBM can neuromodulate and strengthen the power of brain oscillations in alpha and beta frequencies. Also, such neuromodulation effects cannot be attributed simply to heat sensations from the tPBM laser.

3.2 Materials and Methods

3.2.1 Participants

A total of 49 healthy human subjects (30 males, 19 females) 26 ± 8.8 years of age, were enrolled from the local community of the University of Texas at Arlington, Texas, for the sham-controlled tPBM experiment. However, 3 subjects were removed from the dataset due to self-reported/observed tiredness and sleepiness during the investigation. Another total of 14 human subjects with 29 ± 8.8 years of age was recruited from the same community (8 males and 6females) for the sham-controlled thermal stimulation experiment. There was no substantial difference in age between gender groups ($p < 0.2$). Before the recruitment, screening of the human participants was performed according to the exclusion criteria: 1) previous diagnosis with a psychiatric disorder; 2) history of neurological disease; 3) history of severe brain injury; 4) history of violent behavior. All the participants were told to avoid any caffeine beverages 2–3 hours before each experiment.

2.2.2 Experimental Setup

A Biosemi (64-electrode) 10–10 EEG system was employed for the data collection. Before each experiment, electrical gel was applied to improve the conductivity between the electrodes and the scalp. The participants were instructed to maintain their eyes closed with a minimal level of motions during the experiment. Subjects were also directed to indicate minor hand gestures in response to the investigator to verify that they were not sleeping during the experiment. At the end of the experiment, each participant was asked to verify that he/she was awake during the investigation without any drowsiness and sleepiness.

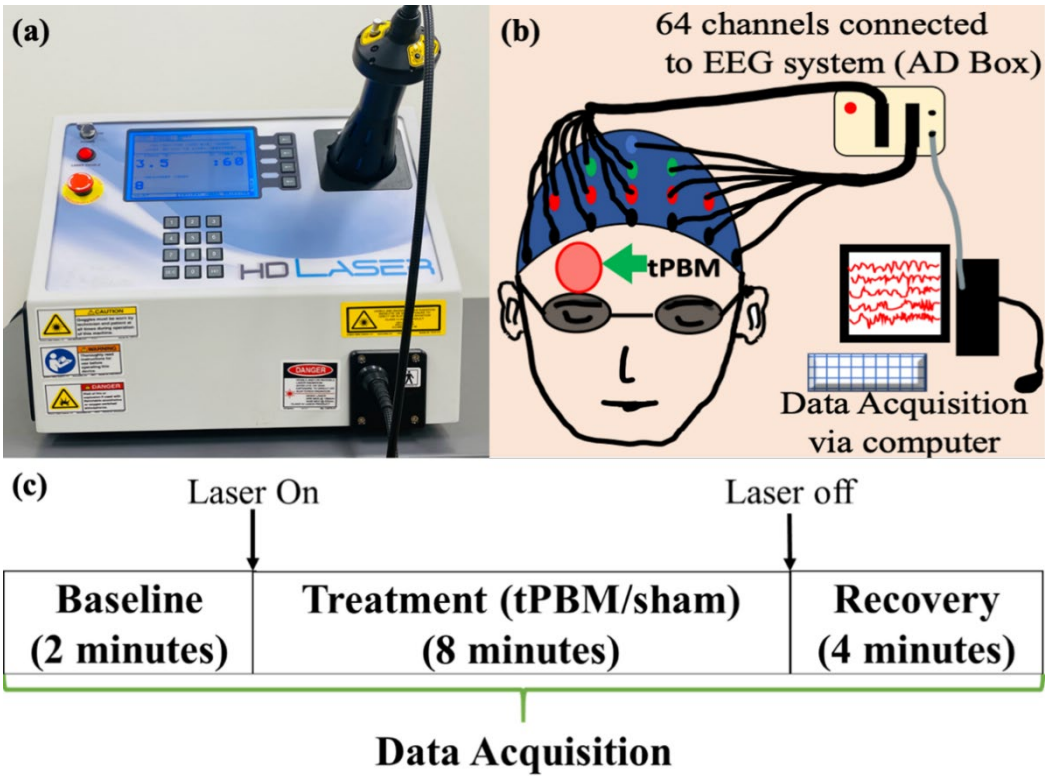

Figure 3-1 Experimental Setup for tPBM. (a) FDA – cleared 1064-nm continuous-wave laser (Model CG-500), (b) Experimental setup: EEG electrodes were attached to the international 10-10 standard EEG cap while the subject was at resting state, eyes closed wearing a safety goggle. The laser head was pointed at the right forehead of the subject, (c) Experimental protocol for EEG-tPBM:

2 – min baseline, 8 – min treatment (laser power of 3.5 W at the treatment and 0.1 W at sham stimulation with extra blockage for further power depreciation), and 3 – min recovery.

Fig. 3-1 shows the experimental setup and protocol. A continuous-wave (CW) 1064-nm laser (Model CG-5000 Laser, Cell Gen Therapeutics LLC, Dallas, TX, USA [Fig. 3-1a]) cleared by the Food and Drug Administration (FDA), was utilized to conduct tPBM and the corresponding sham in this study. A 1064-nm laser is the same laser device used in our previous studies [12, 14, 16, 90]. The laser is equipped with an adequately collimated beam, which permits the delivery of tPBM in an area of 13.6 cm^2. We conducted tPBM with a total power of 3.5 W, which led to a power density of 0.257 W/ cm^2 and a total energy dose of 1680 J over 8 min of tPBM (3.5 W × 480 s = 1680 J) on the right prefrontal forehead, as indicated in Fig. 3-1b). For the sham experiment, the laser power output was set to 0.1 W during the - min stimulation time. In addition, a black colored cap was used to block the aperture of the laser. As a result, respective power density under the sham stimulation was further confirmed to be 0 W/cm^2 by a sensitive power meter (Model 834-R, Newport Corp., Andover, MA, USA) to ensure the complete impediment of laser light.

The stimulation protocol (Fig. 3-1c) consisted of a 2-min baseline, an 8-min stimulation, and a 3-min recovery period. In both tPBM and sham experiments, the laser aperture was pointing at the right prefrontal forehead under electrodes FP2 and AF8. Participants wore protection goggles to protect their vision. The data were acquired at either 256 Hz or 512 Hz. However, all the 512 Hz data were down-sampled to 256 Hz during data preprocessing. Each subject underwent both sham and tPBM experiments over a period of 1 week, with a 2 days separation. The order of the tPBM or sham investigation was randomly assigned. All subjects were inquired about their experience after each experiment, including the heat sensation and potential drowsiness they

perceived. Furthermore, a thermal stimulation experiment was designed to explore the impact of tPBM-associated heat sensations on human EEG signals.

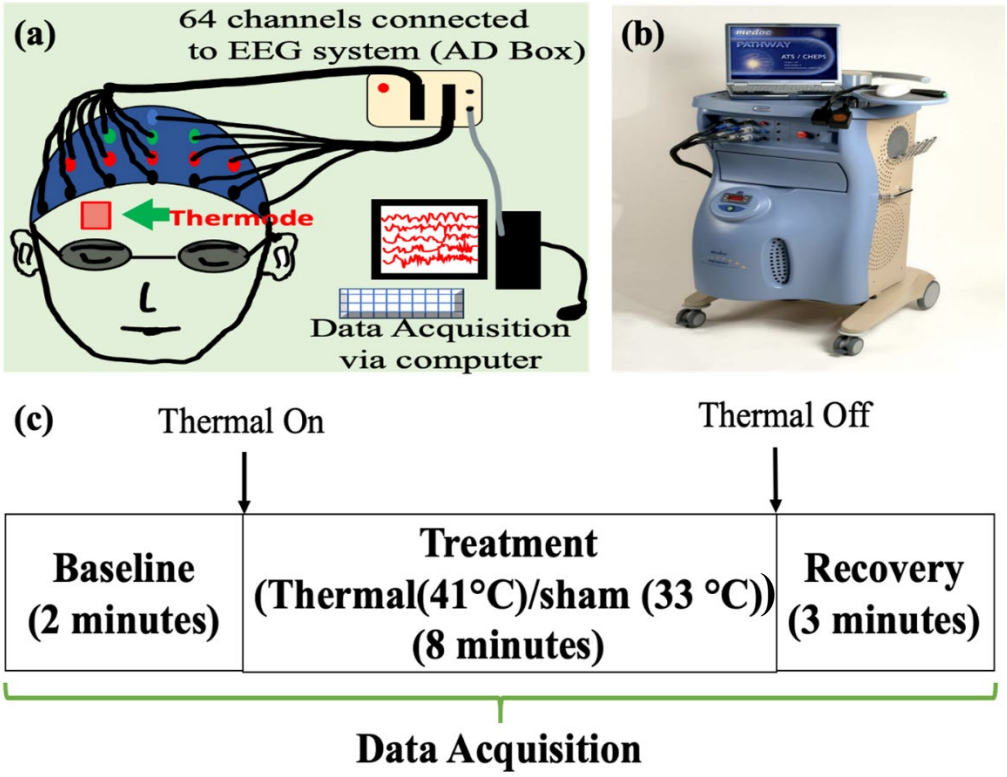

Figure 3-2 Experimental Setup for EEG-Thermal stimulation (a) EEG recordings were performed when subjects maintained an eyes-closed resting state. The thermode heat generator was continuously handheld on the right forehead of the subject to produce heat, (b) Heat simulator (Pathway model with ATS thermode), (c) The time-dependent temperature fluctuation curve: the stimulation temperatures were controlled at 41 °C for thermal stimulation and 33 °C for sham stimulation; the tPBM-induced temperature changes measured by a clinical thermometer (mean with standard deviation) during tPBM experiment are marked as red asteroids and blue error bars.

The time-dependent temperature changes on the human forehead induced by active and sham tPBM were initially measured using an infrared clinical thermometer (Medical Head and Ear Thermometer, Metene, England). Then, a heat stimulator, as shown in Fig. 3-2b (Pathway model

ATS, Pain and Sensory Evaluation system, Medoc Advanced Medical Systems, Israel), was employed to replicate and induce the same temperature changes on the human foreheads through a 16mm x 16mm ATS mode probe. The ATS thermode can deliver painful and non-painful stimuli at a temperature within the range of 0 °C to 55 °C with a maximum rate of 8 °C /sec. The probe was placed on the same place on the forehead, where the laser was pointed during tPBM (right forehead) to convey the non-painful heat stimuli [Fig. 3-2a]. Subjects kept their eyes closed during the experiment.

Fig. 3-2c shows the schematic diagram of the experimental protocol. The experimental protocol of thermal stimulation was designed to include a 2-min baseline, an 8-min thermal stimulation, followed by a 2-min recovery period. The temperature of the skin surface remained at 33 °C during both the baselines of tPBM and sham-tPBM experiments for 2 min. The temperature increased from 33 °C to 41 °C at 8 °C /sec. Then, the temperature was maintained at 41 °C during the stimulation of an 8-min period. Next, we removed the thermode during post-stimulation for 2 min.

As for the EEG recording during thermal stimulation, the sampling frequency was 512 Hz; however, it was also down-sampled to 256 Hz during data analysis to be consistent with the data analysis for tPBM. The temporal structure of the experimental design for the thermal stimulation experiment was invariant to the tPBM investigation, except that there were only 2 min of post-thermal stimulation recovery period, which was 1 min less than the tPBM recovery duration. Due to the unequal recovery periods, further analysis was performed for only baseline and treatment periods, which accounts for 2 min of baseline and 8 min of stimulation.

3.2.3 Data Analysis

Each collected EEG dataset contained 64 channels of time series corresponding to the collected neural activities at different cerebral locations detected by the 64 EEG electrodes. Data from 3

participants were excluded due to drowsiness and fatigue from self-report and experimenter's observation. Therefore, a total of 46 pairs (subjects) of tPBM-and-sham data and a total of 14 pairs (subjects) of thermal-and-sham data were included in the data processing. We first computed the sham-controlled tPBM and frequency-dependent power alterations induced by the 1064-nm laser-illumination during the eyes-closed resting state. Then, we calculated the thermal-sham-controlled and frequency-dependent power alterations induced by the thermal stimulation equivalent to the tPBM laser-illumination during the eyes-closed resting state. Finally, we compared the difference in EEG power changes between sham-controlled-tPBM versus sham-controlled-thermal experiments.

3.2.3.1 Preprocessing

The data were preprocessed using MATLAB and a MATLAB based open source software, EEGLAB. First, the acquired 64-channel EEG raw data were bandpass filtered at 0.5 - 70 Hz. A notch filter was applied to eliminate line noise at 60 Hz. Re-referencing was performed by subtracting the average of voltage signals across all the 64 electrodes. In addition, robust principal component analysis and independent component analysis were performed to remove artifacts, such as eye movements, saccades, and jaw clenches. Next, 64-electrode artifact-free time series were divided into multiple time-segments, including (1) the last 60-s of the baseline before the onset of tPBM/sham (Tb_{tPBM} and $Tb_{sham\text{-}light}$); (2) the first 4-min of the tPBM/sham stimulation ($T_{1\text{-}4\text{-}tPBM}$ and $T_{1\text{-}4\text{-}sham\text{-}light}$); and (3) the last 4-min of the tPBM/sham stimulation ($T_{5\text{-}8\text{-}tPBM}$ and $T_{5\text{-}8\text{-}sham\text{-}light}$). The preprocessed data were then used to perform further analysis.

Likewise, the EEG data of thermal stimulation were preprocessed similarly, producing Tb_{heat}, $Tb_{sham\text{-}heat}$, $T_{1\text{-}4\text{-}heat}$, $T_{1\text{-}4\text{-}sham\text{-}heat}$, $T_{5\text{-}8\text{-}heat}$, and $T_{5\text{-}8\text{-}sham\text{-}heat}$.

3.2.3.2 Time-Resolved Frequency-Dependent Power Density Topography

The 64-electrode temporal segmented time series were bandpass filtered into different frequency bands. Then, the power density values were calculated at each electrode for all five frequency bands, delta (0.5-4 Hz), theta (4-8 Hz), alpha (8-13 Hz), beta (13-30 Hz), and gamma (30-70 Hz). First, 2-sample t-tests were performed to verify that there was no significant difference in EEG powers between the baselines of tPBM and sham experiments (i.e., Tb_{tPBM} and $Tb_{Sham\text{-}light}$). Then, the EEG power densities of the baseline period from each subject, and each band were used as the standard to be normalized with other time segments to express the relative power alterations by tPBM/sham. Briefly, the power density values for each frequency band were calculated for $T_{1\text{-}4\text{-}tPBM}$, $T_{1\text{-}4\text{-}sham\text{-}light}$, $T_{5\text{-}8\text{-}tPBM}$, and $T_{5\text{-}8\text{-}sham\text{-}light}$. Then, they were normalized by Tb_{tPBM} or $Tb_{sham\text{-}light}$. For example, the normalized power changes for each electrode in the first 4-min of tPBM were calculated as $T_{1\text{-}4\text{-}tPBM}$ /Tb_{tPBM}, while the normalized power changes for each electrode in the first 4-min of sham was calculated as $T_{1\text{-}4\text{-}sham\text{-}light}$ /$Tb_{sham\text{-}light}$. This process was repeated on all 64 electrodes, leading to mean power topographies for tPBM and sham. Finally, subtractions were conducted between tPBM and sham to produce the sham-controlled (i.e., sham-subtracted) effects on EEG power induced by tPBM laser illumination. Note that these results include both absolute photobiomodulation effects and thermal sensation influences.

Similarly, the same process was applied to the EEG time series recorded for thermal stimulation/experiments, producing mean power topographies for thermal and sham. Finally, the mean power topographies were plotted and subtracted to show the thermal sensation induced power changes over time.

3.2.3.3 Statistical Analysis

Statistical analysis was performed to compute (1) the sham-controlled tPBM laser-illumination effects on brain oscillations; and (2) the difference between sham-controlled laser illumination effects versus sham-controlled-thermal effects. First, paired t-tests were performed between tPBM and its sham stimulation to compute the significantly modulated EEG powers by the 1064-nm laser illumination in the tPBM experiment. This result includes a mixture of dual-modal effects from thermal sensation and pure photobiomodulation (tissue-photon interaction). The reason for using paired t-tests was because the same subjects participated in both the tPBM and its sham experiments.

In addition, 2-sample t-tests were performed to test the difference between tPBM laser-illumination effects versus the corresponding pure thermal effects. This result denotes the absolute/purified photobiomodulation effects (tissue-photon interaction) of tPBM on human brain oscillations with the exclusion/subtraction of thermal influences. The reason for using two-sample t-tests was because different subjects participated in the tPBM and thermal experiments. Furthermore, the false discovery rate (FDR) corrections were performed to minimize the possibility of compounded type I errors in repeated t-tests. All statistical tests were performed at $\alpha=0.05$.

Moreover, due to the unbalanced sample size between the tPBM and thermal experiments, effect size (d) at each electrode was calculated for the comparison between sham-subtracted tPBM and sham-subtracted thermal stimulation. Specifically, it was calculated by evaluating the difference between two group means divided by the pooled standard deviations of the 2 groups. The result was that $0.2 < d < 0.5$ indicates a small separation between the 2 variables; $0.5 < d < 0.8$ indicates a medium separation; and $d > 0.8$ indicates a large separation between the 2 groups.

3.3 Results

We report results based on several comparisons. First, we looked at the effects of tPBM laser-illumination on EEG power compared to its sham experiment. Then, we investigated the impact of thermal stimulation on EEG power and determined the differences between the sham-controlled thermal effects and the sham-controlled laser illumination effects.

3.3.1 Time-Resolved Frequency-Dependent Power Density Topography for tPBM

Fig. 3-3 illustrates the baseline normalized frequency-dependent topographies for sham-controlled power alterations by tPBM laser-illumination and the corresponding statistical t-maps during the first half and second half of the stimulation.

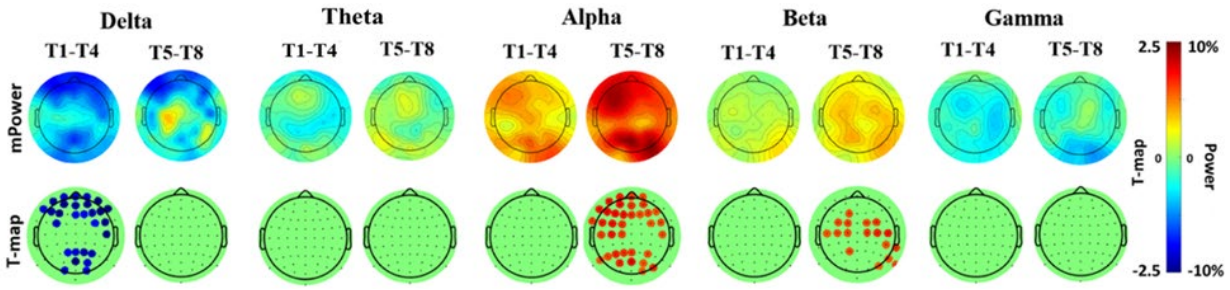

Figure 3-3 Cross-subject sham-controlled, and frequency-dependent topographies for power alterations induced by tPBM (N=46). The first row shows the mean power for T1-T4 and T5-T8. The second row indicates the corresponding statistical T-topographies for the comparison between tPBM versus sham, with paired t-test at $\alpha = 0.05$ under FDR correction.

For the delta band, significantly decreased power was observed at frontal and parietal regions during the first 4-min of tPBM. However, there was no difference in delta power induced by tPBM on the human scalp in the last 4-min of tPBM/sham. In other words, the decreased delta power went back to the baseline of the previous 4-min of tPBM. Further, significantly increased alpha power was observed globally on the human scalp during the last 4-min of tPBM. Mainly, a slightly asymmetric pattern was observed, as more power activations were observed on the contralateral

side (left hemisphere) of the brain. Moreover, significantly increased beta power was more localized at the central/medial regions of the scalp during the last 4-min of tPBM. No significant power difference was observed between tPBM and sham in theta and gamma bands.

3.3.2 Time-Resolved Frequency-Dependent Power Density Topography for Thermal Stimulation

Fig. 3-4 demonstrates the baseline normalized frequency-dependent temporal power fluctuations during thermal stimulation compared to its sham stimulation for the first and second halves of the stimulation period.

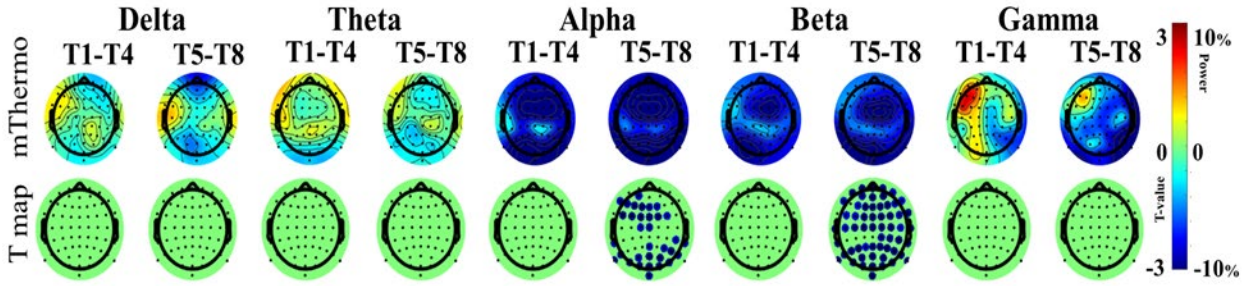

Figure 3-4 Cross-subject sham-controlled, and frequency-dependent topographies for power alterations induced by thermal stimulation (N=14). The first row shows the mean power for T1-T4 and T5-T8. The second row indicates the corresponding statistical T-topographies for the comparison between thermal versus sham, with paired t-test at $\alpha = 0.05$ under FDR correction.

The outcome in Fig. 3-4 illustrates that alpha and beta frequencies were significantly lowered in power during thermal stimulation relative to its sham. In the alpha band, a frontoparietal reduction can be observed. Moreover, in the beta band, power decreases globally. The delta, theta, and gamma bands did not show any significant changes in power. These observations show similarities to tPBM stimulation.

3.3.3 Time-Resolved Frequency-Dependent Power Density Topography comparing tPBM Versus Thermal Stimulation

Fig. 3-5 illustrates the baseline-normalized and frequency-dependent topographies for the comparison between power changes of sham-controlled tPBM laser illumination and sham-controlled thermal stimulation. In Fig. 3-5, the first 2 rows of topographies illustrate the cross-subject average of baseline-normalized and sham-subtracted power alterations for tPBM laser-illumination (mtPBM) and thermal stimulations (mThermo), respectively. The last 2 rows of topographies illustrate the statistical topographies for t-test (T-map) and effect sizes (ES) between sham-controlled 1064-nm laser-illumination effects and sham-controlled thermal effects. The t-tests were based on 2-sample t-tests at $\alpha = 0.05$ under FDR correction.

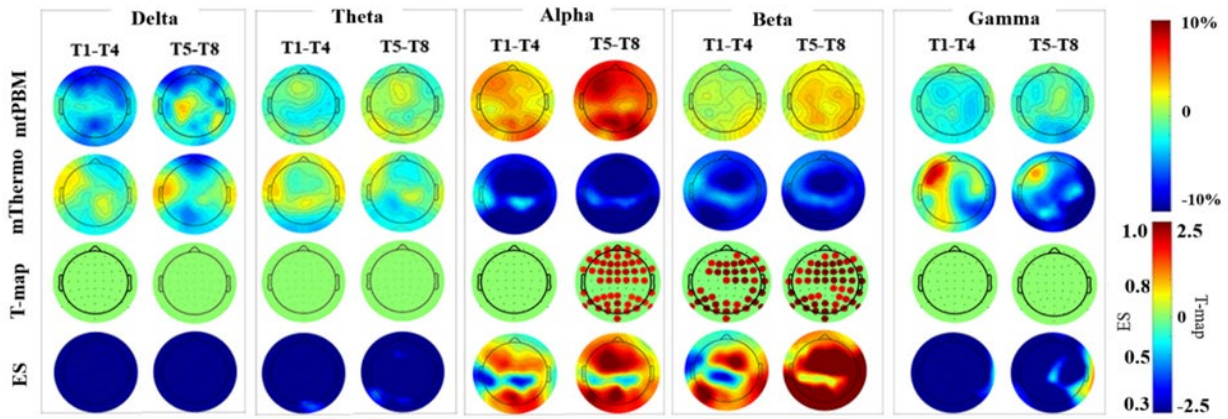

Figure 3-5 Cross-subject, baseline-normalized, and sham-subtracted topographies for power alterations for tPBM (N=46) and Thermal (N=14), in all five frequency bands for the first 4-min (T1-T4) and last 4-min (T5-T8) of the stimulation period. The first row shows the mean tPBM power fluctuations. The second row illustrates the mean thermal power fluctuations. Statistical topographies for two-sample t-tests and effect size (ES) for the comparison between tPBM and Thermal effects are shown in rows-3 and 4, respectively. The T-topographies in row 3 were based on $\alpha = 0.05$ under FDR corrections.

As shown in Fig. 3-5, thermal stimulation created the opposite effects on EEG power in alpha and beta bands with respect to the tPBM laser-illumination. The t-tests were based on 2-sample t-tests at $\alpha = 0.05$ under FDR correction. Specifically, the mean alpha power changes induced by tPBM-laser-illumination were statistically higher than those caused by thermal stimulation at frontoparietal regions during the last 4-min of tPBM/thermal stimulation. Similarly, the mean beta power changes induced by tPBM-laser-illumination were statistically higher than those generated by thermal stimulation at frontoparietal regions during both the first and the last 4-min of tPBM/thermal stimulation. In other words, having thermal effects excluded/subtracted from the dual-modal effects induced by the laser-illumination during tPBM, the absolute photobiomodulation (i.e., tissue-photon interaction) results of tPBM can be expressed as globally enhanced alpha and beta powers. However, no difference was observed between these two means of stimulations in the delta, theta, and gamma bands.

3.4 Discussion

In this study, we recorded in vivo scalp EEG before, during, and after tPBM/sham from 49 human subjects under the eyes-closed resting state. Furthermore, we generated the same temperature enhancement induced by tPBM laser-illumination on human foreheads using a thermal generator system. We recorded in vivo EEG from 14 human subjects before, during, and after thermal stimulation with its corresponding sham experiment. Baseline-normalized EEG power alterations were compared between tPBM laser-illumination and its sham experiments. Moreover, the sham-subtracted EEG power induced by tPBM-laser-illumination was compared with the sham-subtracted thermal-induced EEG power. We observed that the tPBM laser-illumination could significantly decrease the power in delta frequency and enhance power in alpha and beta frequencies. Also, thermal stimulation created the opposite effects of tPBM-laser-illumination

where alpha and beta deactivated, implying that the observed tPBM effects were not due to heat sensation. Finally, calibrated/compared with thermal influences, the absolute/pure tPBM results on EEG power were primarily expressed by the global increment of alpha and beta waves.

3.4.1 tPBM Modulates Alpha, Beta and Delta Power

Fig. 3-3 illustrates the sham-controlled topographic power increment induced by tPBM laser-illumination. The globally enhanced power of alpha and beta oscillations was observed. Notably, a significant increment of power for alpha waves was detected in the anterior-posterior regions. In contrast, a considerable increment of power for beta waves was observed in the central and posterior regions. Significant statistical differences were observed during the last 4-min of tPBM showing a time-dependent manner of power activation.

Although the power of the alpha wave is believed to be related to wakefulness [94], the power of the alpha wave during awake states is also commonly associated with cognition related brain functions such as memory encoding, attention, and brain network synchronization and interaction [95-97]. Moreover, studies indicate that cortical alpha waves are engendered due to the collaboration of thalamocortical and cortico-cortical approaches [98]. With more than 300 human subjects, previous studies using the same 1064-nm laser and the same experimental protocol have shown significant behavioral improvements in cognitive functions [10-12, 85]. As shown in Fig. 3-5 in this study and our previous studies, alpha power was significantly photobiomodulated by tPBM, in both eyes-open and eyes-closed resting state. These findings serve as the electrophysiological evidence for the behavioral improvements.

Also, the observations reported in this study are less biased or driven by the trend/shift of drowsiness/vigilance states, because, in this study, the power increment was not only baseline-normalized, but also sham experiment-subtracted. The tPBM and sham experiments shared the

same experimental protocol and were not undertaken in the same visit. Also, the power increment was resolved by subtracting the baseline-normalized EEG powers between tPBM and sham experiments, which shared the same trend/shift of drowsiness and vigilance states for every subject along with the 13-min investigation.

A tPBM laser-illumination induced beta power increment was also observed (Fig. 3-3). The literature has shown that beta activation is responsible for maintaining concentration. Also, several studies have shown evidence that improved beta waves are a sign of better cognition ability [99, 100]. Hostovecky et al. demonstrated that beta waves are essential to neurofeedback activities [99]. Furthermore, another study showed that beta activation is an indication of cognitive processes with higher concentration by conducting rejection tasks or mental arithmetic tasks, both of which require attention and internal processing [100].

On the other hand, the beta wave is also a sign of somatosensory processing. Beta activation might be responsible for the heat sensation from the tPBM laser [101]. However, the beta response to heat will most probably be limited to the left central region of the brain near the somatosensory cortex because the right forehead was illuminated by the tPBMlaser [102]. However, the beta activation in this study was globally distributed, which cannot be explained as thermal sensations. Therefore, part of the beta power increment in this study might be produced by the optical responses to tPBM, which is responsible for cognition improvement.

While the power of delta waves has been widely recognized for human sleep, the power of resting state delta oscillation has also been linked to cognitive functions. Bablioni et al. reported that better cognitive performance is associated with a decreased power of delta waves. Also, the volume of gray matter is negatively correlated with the power of the delta wave [103]. As shown in Fig. 3-3, the tPBM laser illumination induced decreased delta power in resting state human

brains. The decreased delta might potentially serve as an indication of increased cognitive functions and the volume of gray matter.

Furthermore, according to the literature, increased delta wave has been associated with fatigue [104, 105], depression [106], and addiction [107, 108]. The modulatory effects of tPBM laser-illumination on delta wave are opposite to the abnormalities found in patients with emotional and cognitive disorders, which suggests a promising prospect for tPBM to reverse the changes seen in various psychiatric and psychological conditions such as depression, fatigue, addiction, and other psychiatric/psychological conditions [106]. However, the timely increment in delta power can also be a result of thermal stimulation.

3.4.2 Thermal Stimulation Impact on EEG

As seen in Fig. 3-4, the thermal stimulation generated by the equivalent heat/temperature from laser aperture induced: (1) increased delta power at temporal regions; (2) decreased delta power at frontal areas; and (3) globally decreased alpha and beta powers. Even though delta is not significantly activated, these observations are consistent with previous EEG studies using non-noxious stimuli and noxious stimuli [109]. However, there have been only a limited number of EEG studies on the effect on humans of nonpainful heat stimulus to the brain [110, 111].

The decreased power of the alpha wave may be due to an augmented activity of cortico-cortical and thalamocortical feedback loops [112]. As shown in Fig. 3-4, both alpha and beta activities were globally decreased during the thermal stimulation except for the left central region. Given that the thermal stimulation was delivered on the right side of the body/head, this observation indicates that while heat initiates/triggers central region activation, it can further induce a globally decreased power of alpha and beta waves as co-occurring effects.

3.4.3 Thermal Effect on tPBM

As seen in Fig. 3-5, compared to the sham-controlled tPBM laser illumination effects in which increased alpha and beta powers were observed, thermal stimulation produced the opposite effects on EEG power to laser stimulation. Based on the statistical tests shown in Fig. 5, these 2 stimulation methods/media (light and thermal) induced significantly distinct changes of electrophysiology in alpha and beta frequencies.

Furthermore, one of our previous studies has investigated the thermal effects on tissue-vascular hemodynamic oxygenation and metabolic rates also indicated the similar conclusion that the thermal effect is independent and opposite to the tPBM impacts on human tissue [90]. The observations implied that the brain activation induced by tPBM-laser was not due to thermal sensation. Instead, it might be due to another mechanism/physiological path, which is the photon-tissue photobiomodulation effects on the prefrontal cortex where tPBM took place.

Additionally, it can be inferred that the results shown in Fig. 3-5 may be closer to the truthful and absolute photobiomodulation effects in the human brain by tPBM. The EEG power differences induced by sham-controlled illumination of the 1064-nm laser shown in Fig. 3-5 consists of dual-modal effects of both tissue–light interaction/photobiomodulation and the thermal sensations from the 1064-nm laser. The statistical comparisons (Fig. 3-5) compared the average of EEG power changes caused by the laser-illumination versus the average of EEG power changes induced by the thermal sensation to extract the purified effects induced by tissue-light interactions. Significantly higher global alpha and beta powers were observed for the laser-induced dual-modal effects over the pure thermal impact, indicating that the significant difference between the laser-induced dual-modal effects versus the thermal results was in alpha and beta powers. In other words, by removing/subtracting thermal influences from the comprehensive effects induced by the 1064-

nm laser, the absolute/pure results of tPBM were determined as the globally increased power of alpha and beta waves. Therefore, the true electrophysiology induced by photobiomodulation (i.e., pure tissue–photon interactions) is more appropriately expressed as the globally increased EEG power in alpha and beta bands shown in Fig. 3-5. In addition, the laser/thermal stimulation applied in this study does not damage the tissue. A study conducted on a rabbit brain using CW and pulsed wave lasers demonstrated that the heat generated by a laser with less than 750 mW/cm^2 does not cause tissue damage [113].

3.4.4 tPBM Power During Eyes-Open and the Eyes-Closed Resting States

One of the purposes of this study was to compare the tPBM-induced effects between eyes-open and eyes-closed resting states because EEG signals have been shown to behave differently between these states [22]. In the eyes-open resting state, the brain encounters many visual stimuli and activates the visual information processing networks/paths. However, those processes and pathways are suppressed during the eyes-closed resting state due to the blockage of visual information input [22], indicating the distinct emphasis of brain networks and processes in these two states.

Although the eyes-closed state naturally creates higher absolute powers of alpha wave compared to the eyes-open state on healthy humans [22], it would not affect the interpretation and comparison of the cerebral activations reported for the current study because all the power comparisons in the present research and our previous reviews were based on self-standardization by normalizing to each individual's own baseline. This produces the relative increment of power to its baseline before tPBM or sham is conducted. Furthermore, the subtraction between tPBM and sham (or thermal stimulation and sham) creates the relative difference of activations in the brain under real and fake tPBM/thermal stimulation. All the relative measurements were performed

under the same/constant eyes-closed resting state. Therefore, the observation of relative EEG power increment in this study can be compared with the relative EEG powers calculated in the same fashion under the eyes-open state.

Consistent with our previous study on the assessment of tPBM effects during eyes-open resting state [22], in the current research, a global power increment was observed in alpha and beta frequencies during the eyes-closed state. The results indicated that the activation of electrophysiology induced by tPBM is consistent/reproducible for human resting states. Moreover, the alpha/beta power increment is also compatible with several other published tPBM studies [20, 21]. For example, using an 810 nm pulsed LED system, Zomorrodi et al. reported a shrinkage in the delta band and power improvements in alpha and beta bands [21]. These results emphasized the robustness of alpha and beta waves being neuromodulated by tPBM.

Apart from the consistency in the global distribution of power enhancement for the alpha wave, there are a few slight differences between the 2 studies. This might be due to the subtle differences between the experimental protocols. In our previous eyes-open study, the stimulation was 11 min with 2.2W tPBM delivered by the same laser. However, to minimize the possibility of subjects being drowsy during the experiment, the current study was designed as an 8-min stimulation at 3.5 W, using the same laser. Due to the consistent total tPBM energy delivered, human subjects in these 2 studies should have had a similar level of activations in alpha and beta bands at the end of the stimulation. However, comparing their activation topographies, the distribution of beta power activation in the current study was located in the central regions of the brain. In contrast, the beta activations in the previous study were found more in the occipital areas. Moreover, significant deactivation in the delta band was not observed in the last eyes-open experiment [16]. These results might be due to the higher laser power used in the current study compared to the previous one,

which might have led to more sensible heat/warmness by the participants. As shown in Fig. 3-5, according to the cross-subject topographies of thermal stimulation, thermal sensation tends to decrease the frontal delta power. This can be a potential explanation for the reduced delta power in the current study due to the higher heat sensation from the laser. Nevertheless, the statistical maps (Fig. 3-5) show that, after the consideration of thermal stimulation, decreasing delta power was not shown/included for the pure/real photobiomodulation effects by tPBM, which is consistent with the study in the eyes-open state.

3.4.5 Limitations and Future Work

The significant findings in this study also lead to several drawbacks as well as opportunities for future work. The first drawback is that the thermal stimulation was given based on contact delivery from the thermode probe to the human forehead. In contrast, the sensation of equivalent heat during the tPBM experiment was non-contact. Also, the total area of thermal stimulation was relatively smaller compared to the site of tPBM stimulation. Further, the sample size for the thermal stimulation group was relatively too small to have sufficient statistical significance in comparison with the tPBM group. As for future work, a non-contact heat generator is needed to replicate the findings in this study on a larger number of human subjects.

3.5 Conclusion

This study shows that conducting tPBM with a 1064-nm laser on the right forehead can modulate human eyes-closed resting state oscillations in the delta, alpha, and beta frequencies. The tPBM laser-illumination enhances the power of alpha frontally and parietally and beta rhythms frontally, centrally, and right parietally. Moreover, thermal stimulation, using the equivalent heat from the 1064-nm laser, generated the opposite trend of effects in alpha and beta EEG power. With the

consideration of thermal effects, the pure/absolute tissue-photon photobiomodulation effects induced by tPBM can be more appropriately expressed as the globally increased alpha and beta power, which can serve as the electrophysiological parameters/evidence for behaviorally improved cognitive functions. Nonetheless, there are still open questions, such as how to determine optimal wavelengths and effective dosage to have the best impact of tPBM. Further, the underlying mechanism of reduced alpha and beta EEG power in response to thermal stimulation on the forehead needs to be further explored.

Chapter 4

Transcranial photobiomodulation induced changes in human brain functional activation and dynamic functional connectivity mapped by whole-head functional near-infrared spectroscopy in vivo

(This Chapter is a manuscript that will be submitted soon.)

4.1 Introduction

Near-Infrared (NIR) light has shown the ability to penetrate deep through the tissues to modulate mitochondrial respiration functions. This process is often called photobiomodulation (PBM), also known as low-level laser therapy (LLLT). This technique is applied in many clinical applications on a wide range of cells and nerves in the human body [17, 84, 85]. When the NIR light/laser is delivered to the human brain/head, it's known as transcranial photobiomodulation (tPBM), which has shown promise consequences in treating psychiatric and neurological disorders in the brain such as depression, anxiety [86], and traumatic brain injuries [18, 87, 88]. Furthermore, tPBM can be performed with different lasers/lights with many wavelengths in the NIR region [17]. However, the latest investigations have shown that tPBM using a 1064-nm laser can be functional to augment cognitive functions on healthy brains. The non-invasive optical neuromodulation method has been shown to enhance human cognitive abilities on a range of cognitive-based activities using sham-controlled tests with about 300 human subjects [10-13].

These prior experimental studies displayed significantly boosted concentrations of hemoglobin oxygenation (HbO) and oxidized cytochrome-c-oxidase (CCO) during and after tPBM on human right frontal-cortex with high reproducibility and robustness to illustrate the constructive mechanism of tPBM to the human brain [14, 15, 89]. These investigations proved the hypothesized- mechanism that tPBM has the capability to photo-oxidize CCO, the crucial

mitochondrial enzyme for oxygen metabolism, to heighten the metabolic undertakings of cells/neurons [17]

Near-infrared spectroscopy (NIRS) is an imaging modality that allows measuring biological and physiological states of living tissues non-invasively based on their absorption and scattering within the NIR light [4]. NIRS is widely applied to scrutinize the quantification of oxygenated and deoxygenated hemoglobin (i.e., [HbO] and [Hb]) concentrations in many types of tissues. For example, scientists utilize NIRS to image and diagnose conditions such as cancers in the human breast, prostate, and skin. Moreover, NIRS is commonly used to map functional brain activities *in vivo*. The NIRS systems generally have 2 or 3 wavelengths to compute Δ[HbO] and Δ[Hb] using the Modified Beer-Lambert Law (MBLL) [3, 4, 14]. NIRS has been used to measure hemoglobin concentrations in the brain under a resting state as well as under stimulus-based activities. The mapping of hemoglobin concentrations widely is widely used to determine localized activation in the brain under different conditions.

In the past, studies based on fMRI have considered the connections between different brain regions that are unchanging during the resting state. However, later studies have shown that functional connectivity during short periods is more illustrative of the underlying properties of brain complexes. Dynamic changes are possibly even more conspicuous for the duration of the resting state [114], through which mental activity is unrestrained than in task-based studies. Dynamic functional connectivity (DFC) investigations commonly use the sliding window correlation method. However, there are critical parameters related to calculating DFC, such as window length and the connectivity calculating method (i.e., correlation, covariance, wavelet transform coherence (WTC)) [78, 79, 115].

In this study, we measured resting state data during tPBM and sham conditions to investigate the impact of tPBM relative to sham on hemodynamic fluctuations in the whole head /brain at a cortical level instead of measuring the stimulation at the site. First, we explored the hemoglobin concentration fluctuations close to the stimulation site. Second, we delved into functional brain activation induced by tPBM on the whole brain. Third, we investigated the dynamic functional connectivity studying temporal network changes across the stimulation period of tPBM relative to sham.

4.2 Materials and Methods

4.2.1 Participants

Nineteen adults (5 females, age: 31.7 + 9.5 years) were enrolled for this study. All subjects reported that they were devoid of any neurological or psychiatric disorders. All experimental practices were approved by the Institutional Review Board of the University of Texas at Arlington (IRB# 2017-0859). The subjects were required to sign a written consent before participation in this study.

4.2.2 Experimental Setup

A continuous-wave (CW) fNIRS system (OMM-3000, Shimadzu Corp., Kyoto, Japan) was utilized in this study to measure cerebral hemodynamic responses. The system contained NIR laser diode sources (780, 805, and 830 nm) and photomultiplier tube (PMT) detectors. The data were collected at a sampling frequency of 10.1 Hz. The optode layout contained 32-sources and 34-detectors with a separation of 3 cm resulting in 111 source-detector channels (Fig. 4-1a). The localization of the optodes was marked with a 3D tracker. Statistical parametric mapping (NIRS_SPM) software was applied to estimate Montreal Neurological Institute (MNI) coordinates

for each source and detector location, which also provided the Brodmann area corresponding to each fNIRS channel [62].

Transcranial PBM was administered using an FDA-cleared 1064-nm, CW laser (Model CG-5000 Laser, Cell Gen Therapeutics, Dallas, TX, USA) (Fig. 4-1b). The laser's aperture delivered a collimated beam with an area of 13.6 cm^2 at a maximum power of 3.5 W and a laser power density of 0.25 W/cm^2 [10, 93]. The laser aperture was covered with a filter that would filter out any wavelengths of less than 1000 nm to avoid interference between the laser of the stimulator and the fNIRS source laser diodes. tPBM was delivered to the right forehead of each subject at a frontal site without touching the skin. All presented in the room during the experiment wore protective eye goggles for safety.

The order of the treatment or sham was randomized. If the tPBM session was first, there was a waiting period of at least 1 week for the sham treatment to avoid any carryover effect. During the stimulation period, the CW laser was administered on the right forehead with an output of 3.5 W. In contrast, sham had negligible laser output by turning the laser on and then off immediately within 3 s. During the sham session, the laser power was set to 0.1 W, yet the laser head was covered with a black cap, not allowing any laser energy to penetrate. Subjects were seated with their eyes closed for 8 min of the pre-stimulation period, 8 min during the stimulation period, and 4-min of the post-stimulation period (Fig. 4-1c).

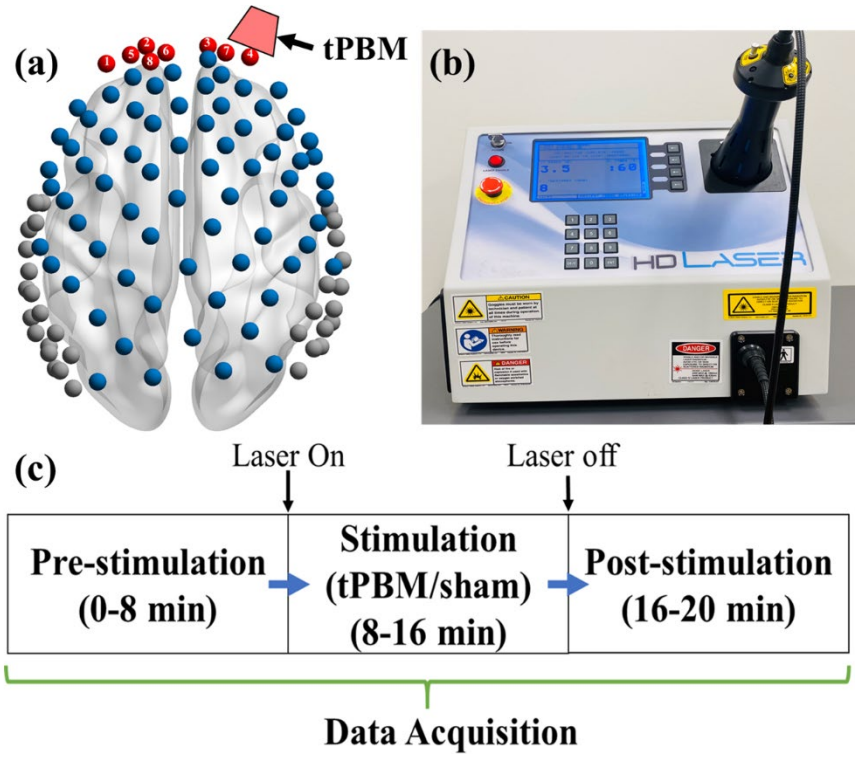

Figure 4-1 Experimental setup and protocol. a) 111-channel layout with 32 sources and 34 detectors. The first 8-channels of the layout are indicated in red with channel numbers. The gray color channels are not included in the analysis, b) 1064-nm laser. c) The experimental protocol randomized sham and tPBM stimulation/treatment for subjects. For the bottom of the protocol, there was a period of at least one week between the two experiments to avoid any effects from residuals.

4.2.3 Data Preprocessing

fNIRS data were preprocessed using Matlab 2019b (MathWorks, Natick, MA, USA) and the open-source package Homer 2.0 [116]. The raw intensity data were then filtered using a lowpass filter of 3rd order Butterworth filter at a cut-off frequency of 0.2 Hz to remove large portions of physiological noise, including heartbeat (1 – 1.5 Hz) and respiration (0.2 – 0.5 Hz) [117]. The principal component analysis was utilized to remove motion artifacts and global hemodynamic fluctuations that may overlap with hemodynamic response frequencies. The first 2 principal

components were removed from all fNIRS channel data to remove the global artifacts [116, 117]. Channels located near the branches from the middle cerebral artery (MCR) or the superficial temporal artery and temporal muscle were devoid of circumventing signal contamination [118, 119], which are indicated in gray in Fig. 4-1a. ΔOD data were converted into changes in hemoglobin concentration relative to baseline (Δ[HbO]) using the MBLL. The differential pathlength factor was assessed as 6.0 for each wavelength in Homer 2.0 [120]. Only Δ[HbO] values are presented in the Results section because Δ[Hb] concentrations were found to have related and opposite qualitative inclinations. In addition, Δ[Hb] was also observed to have smaller amplitudes and lower signal-to-noise ratios, as also found in previous neuroimaging studies [121-123].

4.2.4 Data Analysis

4.2.4.1 Oxygenated Hemoglobin Concentration (Δ[HbO]) Trend for tPBM and Sham.

The artifact-free time series for Δ[HbO] was used for further analysis. The time series for a subject contained data from 111 channels over 11.5 min. The last 0.5 min of the protocol was not used to keep a similar time duration for all subjects because of the inconsistency of total data points. The data inconsistency occurred due to synchronization problems in the experimental setting. The baseline, the averaged Δ[HbO] over 1 min prior to stimulation, was subtracted from its respective time series. The baseline subtracted time series were smoothed using a moving average filter of 30-s of data spans to plot the Δ[HbO] temporal changes for tPBM and placebo. The analysis was performed for all the channels used in the study.

4.2.3.2 Temporal Topographical Δ[HbO] Fluctuation induced by tPBM in the whole head

The smoothed Δ[HbO] data was utilized to generate time-dependent topographic brain images. The time series was separated into approximately 4- min blocks: the first 4-min of the stimulation (T1 -T4), the second 4-min of the stimulation (T5 -T8), and post-stimulation (R1 -R4). Next, the time series blocks were averaged across subjects. The process was repeated for both tPBM and placebo times series blocks. Then, the averaged concentration for each temporal block for tPBM and placebo was compared using a statistical paired t-test ($N = 19$) at $p < 0.05$. The significantly activated/deactivated channels of tPBM compared to placebo were plotted on to topographical brain maps.

4.2.3.3 Dynamic Functional Connectivity (DFC) Analysis

DFC studies the brain connectivity changes during a short period. The most widely used method to calculate DFC is the sliding window method. Previous DFC studies have been performed using window lengths of 30 - 240 s. However, if the window length is less than 15 s, there is a high possibility of detecting false positives. On the other hand, if the window length is more than 240 s, there is a likelihood of overlooking specific information related to dynamic hemodynamic connectivity changes. The Pearson correlation is commonly calculated to create a connectivity matrix over a sliding window [78, 79].

In this study, we used a 30-s window length to calculate the Pearson correlation over approximately 12 min of data points. The edges were recognized as correlation strength, and nodes are channels. The PC was calculated for each 30-s window for 111-channels, which resulted in 23 111-by-111 correlation matrices across the whole duration. The correlation matrices were calculated for tPBM and sham separately. Then the matrices underwent r-to-z transform to

improve the normality of the matrices. Only positive correlation values were considered for further analysis. Next, we utilized z values to compare tPBM versus sham. Statistical paired t-tests were performed for each node and each 30-s window comparing the strength of each node between tPBM and sham at $p < 0.05$ across the subjects (N = 19). FDR corrected (p=0.05) significantly activated channels were plotted using BrainNet Viewer [124]. Moreover, the total number of significantly activated connections from the upper triangle was plotted on a temporal graph to study the fluctuation of the number of significantly activated channels due to tPBM across the experiment.

4.3 Results

The study investigating the tPBM effect on the whole head collected data from 19 subjects with a 111 channel whole-head fNIRS system. Multiple analyses were performed on the data yielding information on sham-controlled tPBM induced temporal and spatial activation. Moreover, the dynamic functional connectivity provided information on temporal connectivity changes over short periods.

4.3.1.1 Oxygenated Hemoglobin Concentration (Δ [HbO]) Fluctuation During Stimulation

Fig. 4-2 shows the Δ[HbO] for tPBM and sham for approximately 11.5 min for 8-channels from the prefrontal cortex. The channels closest to the stimulation site are 2,3,4, and 7 (Fig. 4-1a). Each plot represents the Δ[HbO] trend for tPBM (red) and sham (blue) against time.

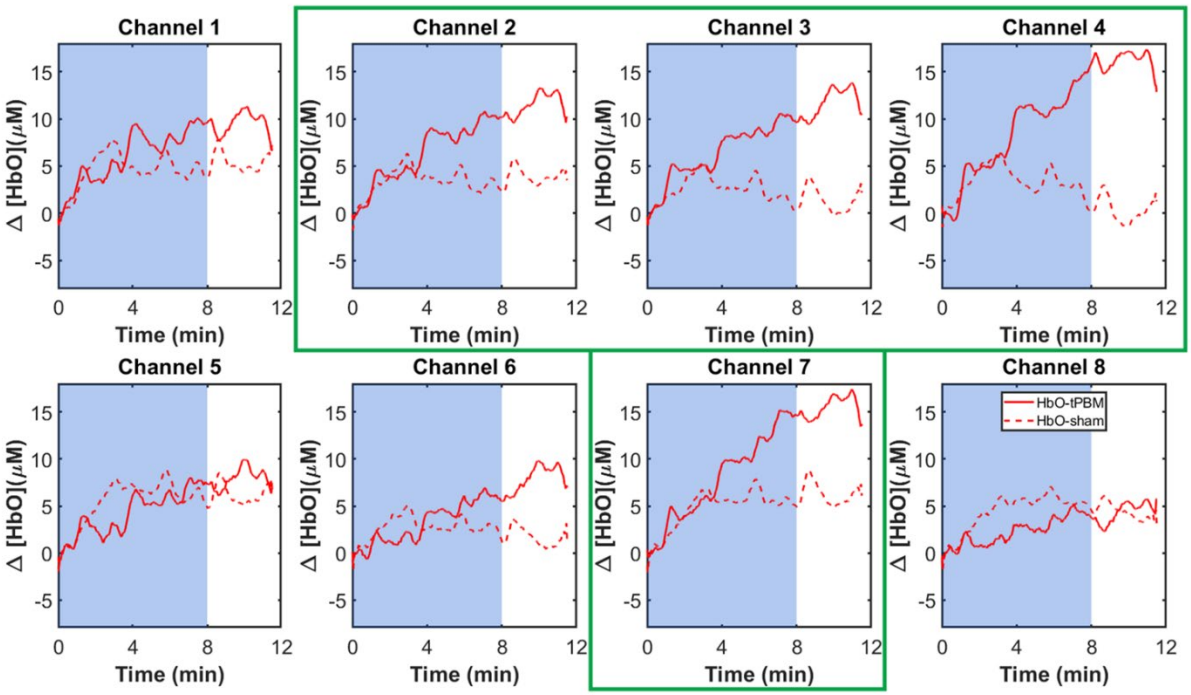

Figure 4-2 The Δ[HbO] trend for tPBM (solid red) and sham (dashed red) compared to the baseline for 8 min of stimulation and rest or post-stimulation period. The first 8-channels were chosen to plot to cover the Front polar cortex (FPC). The channels closest to the stimulation site are illustrated using the green box around corresponding plots. The blue shaded area is the 8-min of stimulation. Channels 1,2,5,6 and 8 are on the left side of the brain, whereas channels 3,4 and 7 are in the right cortex (Fig. 4-1a).

The plots in Fig. 4-2, corresponding to channel 2,3,4, and 7, clearly show an increasing trend for tPBM compared to sham. Even though channel 2 is a channel from the contralateral side to the stimulation site, it also indicates a rising trend for tPBM relative to sham. Sham maintains a relatively constant movement across channels and across time.

4.3.1.2 Function Brain Activation Induced by tPBM Compared to Sham

Fig. 4-3 shows topographical t-maps representing significantly activated/deactivated channels for tPBM relative to sham for 3 temporal blocks: T1-T4, T5-T8, and R1-R4.

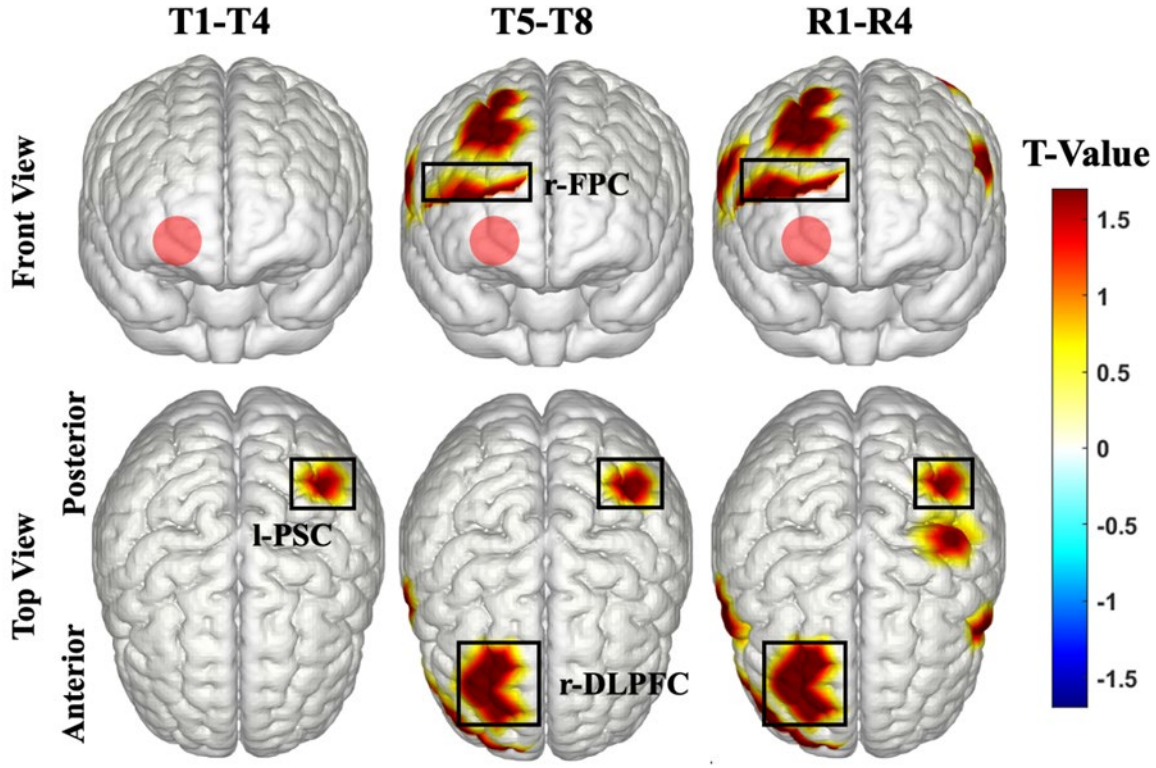

Figure 4-3 Significantly activated time dependent Δ[HbO] fluctuation in the whole cortex for tPBM relative to sham. The front (1st row) and top (2nd row) view of topographical t-maps for T1-T4, T5-T8, and R1-R4 showing significantly activated/deactivated channels/areas in the brain induced by sham-controlled tPBM for Δ [HbO]. The red color filled circle illustrates the stimulation location on the right forehead. Significance is calculated using a paired t-test at $p < 0.05$ between tPBM and sham after FDR correction. PSC- primary somatosensory cortex; FPC - front polar cortex; DLPFC -the dorsolateral prefrontal cortex; PMSMC- Premotor and supplementary motor cortex.

During T1-T4, the activation was observed only in the l-primary somatosensory cortex (PSC). During T5-T8, rDLPFC and rFPC show activation along with rBroca area. lPSC continued to be activated for the rest of the experiment duration. Further, during the recovery period, rDLPFC and rFPC demonstrated the same trend as T5-T8. As illustrated in Fig. 4-3, the activation was

prominent in the prefrontal area, especially rFPC and rDLPFC. The rPFC areas activated increase as time increases. There was a consistent activation in the left primary somatosensory area, which is the lobe opposite to the stimulation site. During T5-T8, there was substantial activation in the right FPC, DLPFC, and PSC as well.

4.3.1.3 Dynamic Functional Connectivity Due to tPBM

Fig. 4-4 illustrates the results for dynamic functional connectivity changes over stimulation and rest at every 30 s. The significant connections for tPBM were compared to sham in paired t-test at $p < 0.05$ for each window in red lines on topo plots. Fig. 4-4 shows topo plots illustrating significant connections for tPBM relative to sham for the stimulation and post-stimulation periods.

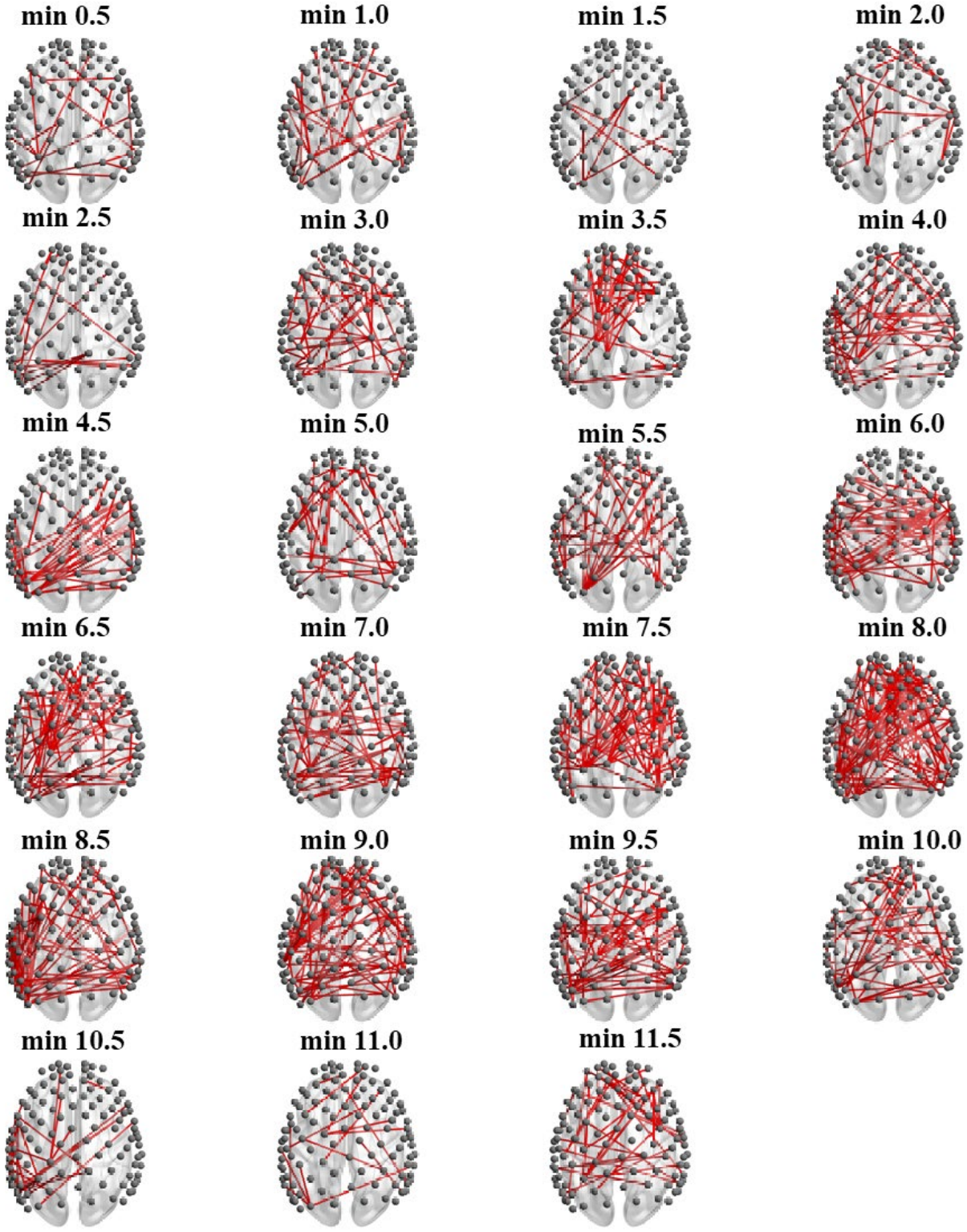

Figure 4-4 The significant connections among the different regions in the brain induced by tPBM compared to sham indicated in red lines at $p < 0.05$ (FDR Corrected). The gray dots indicate the

nodes of the network. Red lines are edges of the network. Topo plots of 0.5 min to 8.0 min shows the stimulation period. Topo plots of 8.5 min to 11.5 min shows rest/ post-stimulation periods.

As illustrated in Fig. 4-4, there is an increasing trend of connections during tPBM over sham during the treatment. However, it relatively decreased during the rest period. Most dense connections can be noted during the 8th min. However, the density of the connections started reducing when stimulation/treatment stopped. In addition, after the first 4-min, the connection density became more intensive compared to the first 4-min. Further, the brain tended to show more communication with multiple regions and across hemispheres.

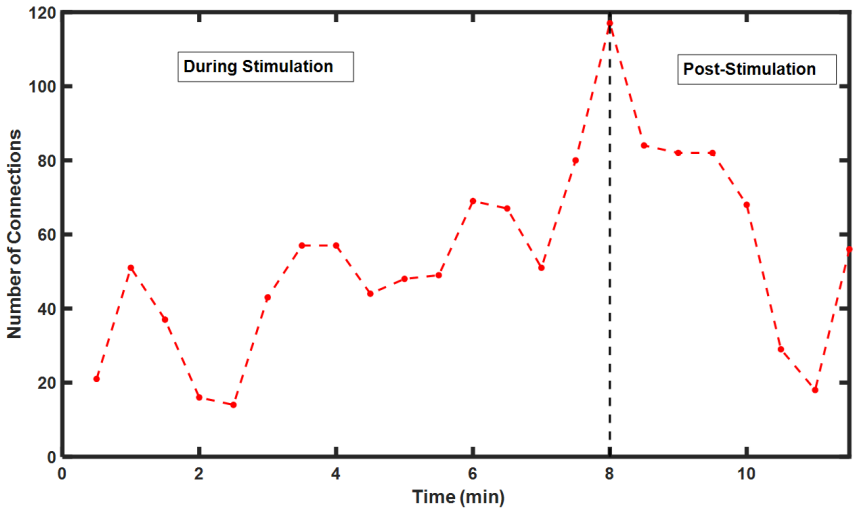

Figure 4-5 The number of connections fluctuation induced by tPBM over sham. The left side of the dashed vertical line represents the during stimulation. The right side of the dashed vertical line represents the post-stimulation.

Moreover, Fig. 4-5 further illustrates the fluctuation of the total number of significant connections formed chronologically during the experiment. Fig. 4-5 provides a quantitative representation of the number of links illustrated in Fig. 4-4. According to the graph, the connections gradually increased as a response to tPBM. However, the decrement is evident after the stimulation.

4.4 Discussion

Data were collected from 19 subjects under tPBM from a 1064-nm laser and sham stimulation during an eyes-closed resting state. Oxygenated hemoglobin patterns were studied for both tPBM and sham for the experimental duration for the channels close to the stimulation site. Further, we observed significant Δ[HbO] activation in multiple locations in the brain induced by tPBM relative to sham. In addition, we noticed substantial observations in dynamic functional connectivity as well.

4.4.1 Oxygenated Hemoglobin Δ[HbO] Fluctuation Induced by tPBM

Transcranial photobiomodulation (tPBM) is a process in which a NIR light source (760 – 1064 nm) aids in improving the metabolism and hemodynamics in the brain using the energy of the photons [14, 17]. The functionality of PBM depends on cytochrome c-oxidase (CCO), which is an enzyme in the mitochondrial respiratory chain (electron transportation chain). It plays a vital role in ATP production. The higher the oxidized CCO enhances, the better the mitochondrial oxidative phosphorylation produces better utilization of oxygen and metabolic energy [90]. CCO is the main component that absorbs energy/photons from the laser, which improves oxygen metabolism. There is a linear relationship between tPBM-induced Δ[CCO] and Δ[HbO] according to the previous studies that have demonstrated an interplay between the components. This relationship provides evidence to suggest that an oxygenated hemodynamic response increment transpires due to the tPBM-enhanced oxidized CCO [14, 90, 93].

The findings shown in Fig. 4-2 illustrate that Δ[HbO] of channels near the stimulation site has increased relative to sham over time. Similarly, tPBM conducted with a 1064-nm laser on the right forehead has been shown to increase Δ[HbO] and Δ[CCO] at the site of the stimulation (right forehead) measured by a single channel broadband fNIRS (bb-NIRS) system. Moreover, another

study conducted using the same protocol and laser, but with different operators, and subjects at different locations and taken several years apart, demonstrated the reproducibility of the impact of the laser [89, 93]. The results also illustrated Δ[HbO] activation pattern over time similar to our current Δ[HbO] pattern. Moreover, the activation induced by tPBM showed an increasing trend over time in many areas in the brain following the same pattern as was observed at the site of the stimulation with bb-NIRS [14, 89]. Consequently, the results imply that tPBM enhancement relative to sham can be detected using the whole-head fNIRS system.

4.4.2 Resting State Functional Cortical Activation Enhanced by tPBM

Due to the limited number of channels in the bb-NIRS system, there is a reduced possibility of measuring multiple regions in the brain. Overcoming the difficulty of having more channels, LABNIRS allowed us to measure the Δ[HbO] from the whole head with multiple channels. Fig. 4-3 illustrates significantly activated regions due to tPBM in the top and front views of the brain topographies in 4-min temporal segments. Consequently, this study shows Δ[HbO] changes in multiple areas on the cortex, including the right prefrontal cortex (rPFC), especially in the rFPC, and rDLPFC due to tPBM. Moreover, it shows activation in lPSC, indicating probable heat impact from the laser. In addition, the areas that are activated due to tPBM show improvement and consistency.

During the resting state, one's internal thinking continues. Subjects undergo constrained verbal feelings, creating mental metaphors, the recollection of previous experiences centered on episodic memory and planning. Moreover, under experimental conditions, subjects are instructed to prevent themselves from moving. This activates an inhibitory response for movement. All these activities can be identified as mechanisms of working memory and executive systems, recognized to be maintained by high-order connective multimodal and paralimbic areas [125-127]. PFC is known

to be responsible for working memory, cognitive, and executive functions [128, 129]. However, studies have shown that there is a relationship between resting state activation and task-oriented activation [130]. Among the cortical level structures, FPC and DLPFC play a crucial role. According to Fig 4-3, rFPC and rDLPFC illustrate significant activation by tPBM compared to sham. rDLPFC activation during rest shows more functionality in the region. A study conducted on the lateralization of DLPFC functionality reported that rDLPFC was involved in detailed planning and decision making at multiple levels of the planning [131].

Further, a study conducted to observe effects on meditation/attention focused breathing has shown significant activation in rDLFPC, which hints that tPBM can aid the brain in short-term meditative effects [132]. In addition, the studies performed to investigate the behavioral outcome of tPBM with approximately 300 subjects have shown that tPBM can significantly improve their behavioral impact in terms of reaction time and memory retrieval [10, 12, 18]. Consequently, tPBM-induced improvement of activation in rPFC can be directly associated with the enhanced working memory, cognitive, and executive functions due to tPBM. Moreover, PFC and PSC activation can relate to the activation of frontoparietal resting state network activation [127].

4.4.3 Impact of Heat Produced by Laser

The activation maps in Fig. 4-3 show significant difference in l-PSC activation. This activation may have occurred due to the influence of heat that the laser head generated. After the experiment, the subjects commented on the heat sensation they perceived during the tPBM. Therefore, the contralateral hemisphere activation in l-PSC to the right forehead can be attributed to heat. However, Wang et al. reported that when thermal stimulation replicating the same heat was delivered to the right forehead, deactivation of Δ[HbO] was seen at the stimulation site [90].

Nonetheless, since the experiment was performed with bb-NIRS, there was no evidence to show that l-PSC was also activated due to heat stimulation.

4.4.4 Dynamic Functional Connectivity (DFC) Changes Stimulated by tPBM

Resting state connectivity causes significant awareness of spontaneous brain activity. However, DFC network patterns are essential for a more thorough understanding of large-scale network activity. Many recent findings have indicated that these phenomena may be an inherent property of brain function with a neural basis. It is hypothesized that alterations in FC occur from the transformations in the coordination and connectivity of neocortical microcircuits themselves. For example, an alteration in large scale FC and a depolarization condition of a local cortical column may cooperate via two major complementary routes: (1) a local state change can be the source for long-range changes in FC, and (2) the local state shift is an indication of obscure influences and hence reflects the reconfiguration of a more extensive network [78, 79].

Fig. 4-4, and Fig. 4-5 illustrate the connectivity fluctuations in the brain due to tPBM relative to sham. Fig. 4-4 demonstrates how brain connectivity changes across the brain regions. In the initial 4-min, the connections are not highly dense. However, after 4-min, tPBM causes the brain to form more dense connections between frontal areas and parietal regions, which shows the activation of the front-parietal network. These indications show signs of enhanced cognitive function due to tPBM [29]. The density of connections increases with the tPBM dosage, as shown in Fig. 4-4, and Fig 4-5.

Consequently, according to the hypothesis for DFC changes, we can interpret from our results as tPBM causes neocortical microcircuits to change their orientation, which leads to enhanced connectivity during tPBM. Especially during the 8^{th} min, there seems to have a high density of connections in the rPFC compared to other regions, which are also very close to the tPBM site.

Moreover, when the tPBM dose is completed, the connectivity reduces. To sum up, DFC analysis shows that tPBM has a significant effect on DFC in different regions in the brain compared to sham.

4.4.5 Limitations and Future Work

The study investigated the effects of 1064-nm laser directed at the right forehead by observing cerebral hemodynamics measured with the whole-head fNIRS system. Since this is a proof of principle study, many limitations exist, including several listed below: (1) Due to limited wavelengths of the fNIRS system, the only parameters we could measure were [HbO] and [Hb]. Quantification of [CCO] needs a multi-wavelength bb-NIRS system with multiple channels to cover the whole-head. (2) More investigations are required to perform in order to figure out what is the optimal wavelength is for the laser with neurophysiological benefits. (3) We still need to study the post-stimulation effects of the tPBM. (4) For calculating DFC, an appropriate dynamic window length of time series, selection of proper edges and nodes, and interpretation of results remain to be further explored.

4.5 Conclusion

This study demonstrated that conducting tPBM with 1064-nm laser on the right forehead improves activation of [HbO] mainly in PFC, especially in rFPC, and in rDLPFC, which are responsible for various executive functions such as working memory and cognitive functions. The stimulation site is the right forehead. Moreover, DFC analysis shows that during the tPBM, the connectivity relatively increased proportionally to the dosage of the irradiation. However, during the post-stimulation, the connectivity density dropped. The findings indicate that the tPBM can evoke spontaneous changes to brain connectivity during short periods, which causes increased

connections between distant and closer regions. Consequently, tPBM can be applied to improve executive functions while improving brain connectivity to enhance brain performance.

4.6 Further Discussion Remarks

4.6.1 Improved Calculations for Dynamic Functional Connectivity

Dynamic functional connectivity can be quantified using variability. Often, it is compared with static functional connectivity [45, 133]. As a comparison, I calculated using an overlap of 50% and 90%, considering 30-s intervals and 60-s intervals, to assess the DFC. Fig. 4-6 shows the DFC fluctuation in terms of the number of significant connections across time for 30-s intervals and 60-s intervals with a 50 % or 90 % overlap, respectively. All four subplots in Fig. 4-6 show an overall increasing trend and less variability during post-stimulation.

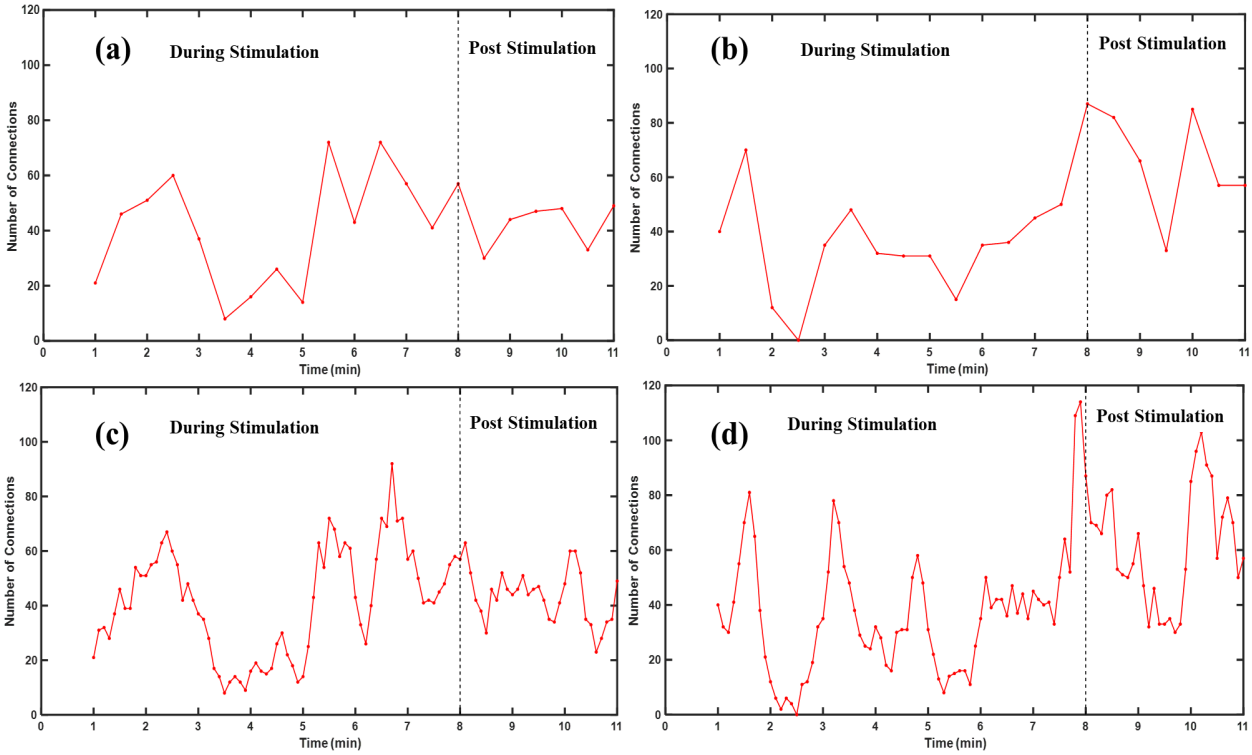

Figure 4-6: The number of connections fluctuation induced by tPBM over sham for different connectivity matrix intervals and 50% and 90% overlap when calculating the matrix. The left side of the dashed vertical line represents the data during stimulation. The right side of the dashed vertical

line represents the data post-stimulation. (a) 30-s intervals with 50 % overlap, (b) 60-s interval with 50 % overlap, (c) 30-s interval with 90 % overlap, and (d) 60-s interval with 90 % overlap.

4.6.2 Functional Connectivity Variability

One of the widely used methods to quantify DFC is using functional connectivity variability (FCV). FCV was calculated across the experimental duration to assess the variance of the normalized correlation coefficients. Further, FCV for tPBM and sham were calculated separately. Mean FCV across subjects for tPBM and sham was illustrated in Fig. 4-7. However, there was no significant difference between tPBM and sham at $p < 0.05$ significance level.

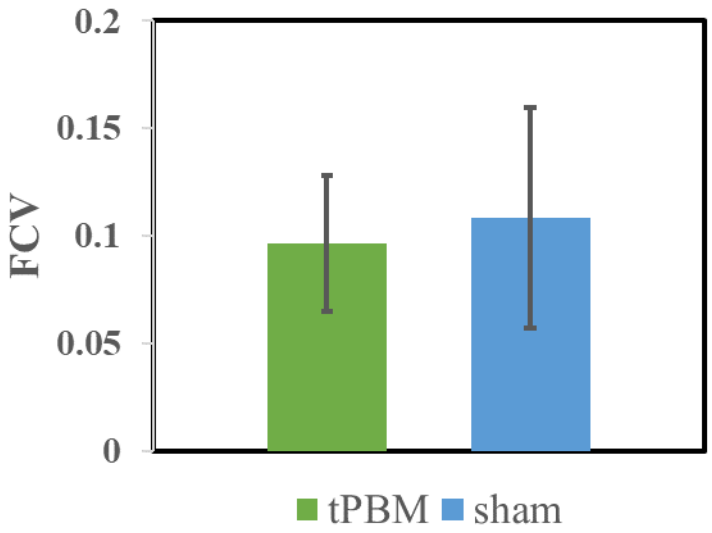

Figure 4-7: Mean functional connectivity variability (FCV) across subjects for tPBM and sham for 30 seconds interval without overlapping considering the whole duration of the experiment including treatment and recovery period. tPBM represents in the green bar. Sham represents in the blue bar. The error bar symbolizes the standard deviation of FCV.

Fig. 4-7 shows that the mean variability in tPBM is lower than in the sham. Even though tPBM and sham mean FCV values are not statistically significant, low variability in DFC is a sign of increased attention [45, 133].

4.6.3 Reduce Mental Stress Through Right Dorsolateral Prefrontal Activation Using tPBM

In this dissertation research, deactivation and activation in rDLPFC indicated an exciting relationship. In a task involving mental stress, rDLPFC deactivated; however, tPBM was able to activate rDLPFC. Specifically, according to the observations in Chapter 2, a low margin scenario (Fig. 2-4) showed a significant decrement in rDLPFC, possibly due to fatigue and stress [73, 74]. In contrast, the tPBM study demonstrated that rDLPFC could be significantly activated using tPBM, as shown in Fig. 4-3. A tDCS study showed that stress and fatigue could be reduced by performing tDCS on the rDLPFC [73]. This evidence indicates that activating rDLPFC can help reduce mental fatigue or stress, an observation that leads to the possibility of using tPBM to improve fatigue/ stress in humans in a relatively more accessible and safer manner in future work.

Chapter 5 – Conclusion and Future Scope

5.1 Conclusions

The main objectives of my dissertation work were to (1) assess cerebral hemodynamic response to neuroeconomic decision-making tasks; (2) evaluate and quantify electrophysiological and hemodynamic response to transcranial photobiomodulation (tPBM) during the eyes-closed resting state. In the study, metrics such as a general linear model (GLM), graph theory analysis (GTA), functional activation, and dynamic functional connectivity (DFC) were applied to assess hemodynamic responses generated from fNIRS. Moreover, a power analysis was utilized to quantify and compare the effects of tPBM and tPBM-induced thermal impact measured by EEG. Specifically, Chapter 2 investigated hemodynamic brain imaging in multiple foreign regions in response to a risky decision-making task in a business domain, namely, the newsvendor problem (NP) using a 77-channel fNIRS imager. Chapter 3 investigated and mapped tPBM and thermal effect on electrophysiological signals administered on the right forehead during the eyes-closed resting state using a 64-channel electroencephalograph (EEG). Chapter 4 fulfilled the third aim, of investigating and mapping whole-head hemodynamics brain imaging in response to right-forehead tPBM during eyes-closed resting state using a 111- channel fNIRS imager.

Explicitly, in the first study, as presented in Chapter 2, an fNIRS system was utilized to measure hemodynamic signals from 27 healthy subjects with a comprehensive NP task protocol with neuroimaging to investigate brain-behavior under NP. The study showed that NP evoked PFC activation, especially in FPC, OFC, and DLPFC. Moreover, during a higher risk NP, more activation tended to be in lDLPFC while deactivation was observed in rDLPFC. Further, under a lower risk NP, FPC, OFC, and lDLPFC were activated. The findings show that FPC, OFC, and DLPFC are responsible for NP decision-making at the cortical level. When there is a higher risk

of failing, rDLPFC deactivates, indicating the probability of fatigue and mental stress. Moreover, with higher-risk situations, the lDLPFC activates more prominently. However, the lower risk situation triggered cortical level activation in OFC, showing the impression of reward path activation due to positive outcomes.

Further, Chapter 2 discussed the brain network characteristic deviation from the resting state to a task-oriented state using graph theory analysis (GTA). The observations showed that the decision phase has lower global efficiency and higher pathlength while displaying higher local efficiency and clustering coefficient. Regardless of the risk level, brain network characteristics exhibited the same behavior when comparing the decision phase and rest. The results indicated that the brain works more efficiently locally as clusters during a task while globally functions at its best during the resting state.

As presented in Chapter 3, an EEG system was used to measure electrophysiology signals from 49 healthy human brains under transcranial photobiomodulation (tPBM) during the eyes-closed resting state. Moreover, the impact of the heat from the laser was tested under thermal stimulation replicating the temperature fluctuations during tPBM. The power analysis shows that tPBM modulated and enhanced alpha and beta power. In contrast, alpha and beta showed deactivation due to thermal stimulation. The findings show that tPBM and thermal stimulation yielded relative opposite responses in brain oscillations. However, enhanced alpha and beta oscillations due to tPBM can be interpreted as signs of improved cognition, working memory, and concentration. Consequently, the tPBM can modulate alpha and beta rhythms in the brain.

Chapter 4 consisted of a study utilizing the whole-head fNIRS system to investigate the hemodynamic response to tPBM in 19 healthy volunteers. Results indicated that tPBM showed primary activation in rPFC. It is the region closest to the stimulation site, which is the right

forehead. rPFC is responsible for working memory and for cognitive and executive functions. Moreover, DFC analysis showed that during tPBM, the connectivity increased proportionally to the dosage of the irradiation. However, during the post-stimulation, the connectivity density dropped. The findings indicate that tPBM can evoke spontaneous changes to brain connectivity during short periods, which causes an increase in the connections between distant and closer regions. Consequently, tPBM can be applied to improve executive functions while improving brain connectivity to enhance brain performance.

5.2 Limitations and Future Work

The work in this dissertation comes with several limitations. However, there are approaches to mitigate the challenges in future work.

First, I focused on brain activation only during the decision-making phase due to the complicated nature of the protocol. However, there is still more information we can extract in the feedback phase. The feedback phase is also a critical phase to observe the reaction to NP. Therefore, there is still room to study the feedback phase. Through the spontaneous nature of the protocol and NP, it is possible to investigate the neural-electrophysiology behind the NP-based decision-making tasks utilizing EEG.

Second, there are numerous methods to perform data analysis for EEG signals. However, I have considered calculating only EEG powers using the root mean square (RMS) method. Therefore, future work can utilize more robust data analysis methods, such as power spectrum density, to investigate the impact of tPBM further. Moreover, there is a possibility to study tPBM tPBM-induced effects on the human brain in depth by investigating functional connectivity changes due to tPBM.

Third, the tPBM studies were performed only with the use of a 1064- nm laser. However, lasers at other NIR wavelengths might give more optimal results, which is an issue that needs further investigation. Moreover, there are more key concepts to be explored, such as post-stimulation effects, optimal stimulation dosage, and means to minimize the heat effect. Last, a multimodal imaging approach with fNIRS and EEG is our next approach to study neurovascular coupling and the impact of stimulation location by the 1064-nm laser or lasers at other wavelengths.

Appendix

This section consists of the MATLAB codes that were used for processing each aim.

A. Decision-Making GLM Analysis (Aim 1a)

Decision

```
clc;
clear
close all;
```

```
sub =[1 2 3 4 5 6 12:15 17 18 20:22 24 26 27 29:31 33:36 38 39];
N=length(sub);

block =[40 40 30 40 50 40 40 40 40 34 40 40 40 20 40 39 40 36 40 40 40 40 40 40 40 40 39];
col=1;
for i=1:N

    blocks = block(i);
    disp(sub(i));
    %Load the timer file
    timer_file=xlsread(['D:\Lab\labnirs_coba\original_data\coba\voltage\data\Subject'
num2str(sub(i)) '\sub' num2str(sub(i)) '.xlsx']);
    [onset_1,duration_1,onset_2,duration_2,modulation]=timer_function(timer_file,blocks);

    %load the .mat file
    S1=load(['D:\Lab\labnirs_coba\original_data\coba\voltage\detrend_hbo_nirs_data_sub_'
num2str(sub(i)) '.mat']);
    oxy1=S1.nirs_data.oxyData;
    oxy1=oxy1(:,1:77);
    x_oxy=mean(oxy1,2);

    % Removing scalp noise
    for i1=1:1:77
        m_oxy(:,i1)=oxy1(:,i1)-x_oxy;
    end


% Preparing variables to GLM input
    fs=12.8205;
    b_oxy=m_oxy;
    fs=12.8205;
    onset{1,1}=onset_1;
    onset{1,2}=onset_2;
    duration{1,1}=duration_1;
    duration{1,2}=duration_2;
    names={'Task','Rest'};
    M{1}=modulation;
    M{2}=modulation;
% Run GLM to get beta values
```

```
    [beta(:,:), tvalue(:,:), pvalue(:,:), covb] =
glm(b_oxy,{onset{1,1},onset{1,2}},{duration{1,1},duration{1,2}},{M{1},M{2}},0,0,fs);

    clear S1 oxy1 dxy1 x_oxy x_dxy stats_oxy m_oxy
    clear stats_dxy m_dxy b_oxy b_dxy

% Extracting decision betas and feedback betas

    betad1(:,i) = beta(:,1);
    betaf1(:,i) = beta(:,2);

    disp(i);
end
```

Performing t-test for decision beta

```
ch = 77;
for i = 1:ch
    [h11(i,:),p1,c1,stats1] = ttest(betad1(i,:),0, 'alpha',0.1);
    t_value1(i)=stats1.tstat;

    if abs(t_value1(i)) < 1.703
        t_value1(i) = 0;
    end
end

% Calculating mean beta values
betad = mean(betad1(:,2:end),2);
betaf = mean(betaf1(:,2:end),2);
```

Plotting

```
figure
topo_plotting(t_value1,2.5,[0 1 0]);
```

Published with MATLAB® R2019b

B. Graph Theory Analysis (Aim 1b)
Comparing LM & HM

```
close all
clear
clc
```

Network Parameters

```
load('d:\Lab\Coba_fnirs_gretna\dynamic\LM_1lap\LM_01_05_1lap\NetworkEfficiency\NetworkEfficiency.
mat',"Eg","Eloc");
lmDecision_eg= Eg;
lmDecision_eloc= Eloc;

load('d:\Lab\Coba_fnirs_gretna\dynamic\LM_1lap\LM_01_05_1lap_rest\NetworkEfficiency\NetworkEffici
ency.mat',"Eg","Eloc")
lmrest_eg= Eg;
lmrest_eloc= Eloc;

load('d:\Lab\Coba_fnirs_gretna\dynamic\HM_1lap\HM_01_05_1lap\NetworkEfficiency\NetworkEfficiency.
mat',"Eg","Eloc");
hmDecision_eg= Eg;
hmDecision_eloc= Eloc;

load('d:\Lab\Coba_fnirs_gretna\dynamic\HM_1lap\HM_01_05_1lap_rest\NetworkEfficiency\NetworkEffici
ency.mat',"Eg","Eloc")
hmrest_eg= Eg;
hmrest_eloc= Eloc;

load('d:\Lab\Coba_fnirs_gretna\dynamic\LM_1lap\LM_01_05_1lap\SmallWorld\SmallWorld.mat',"Cp","Lp"
,"Sigma");
lmDecision_cp=Cp;
lmDecision_lp= Lp;
lmDecision_sigma=Sigma;

load('d:\Lab\Coba_fnirs_gretna\dynamic\LM_1lap\LM_01_05_1lap_rest\SmallWorld\SmallWorld.mat',"Cp"
,"Lp","Sigma");
lmrest_cp=Cp;
lmrest_lp= Lp;
lmrest_sigma=Sigma;

load('d:\Lab\Coba_fnirs_gretna\dynamic\HM_1lap\HM_01_05_1lap\SmallWorld\SmallWorld.mat',"Cp","Lp"
,"Sigma");
hmDecision_cp=Cp;
hmDecision_lp= Lp;
hmDecision_sigma=Sigma;
```

```
load('d:\Lab\Coba_fnirs_gretna\dynamic\HM_1lap\HM_01_05_1lap_rest\SmallWorld\SmallWorld.mat',"Cp"
,"Lp","Sigma");
hmrest_cp=Cp;
hmrest_lp= Lp;
hmrest_sigma=Sigma;
```

Comparing Decision vs Rest for LM and HM

```
a=0.01;
hlmeg=ttest_gretna(lmDecision_eg,lmrest_eg,a);
hlmeloc=ttest_gretna(lmDecision_eloc,lmrest_eloc,a);
hlmcp=ttest_gretna(lmDecision_cp,lmrest_cp,a);
hlmlp=ttest_gretna(lmDecision_lp,lmrest_lp,a);
hlmsigma=ttest_gretna(lmDecision_sigma,lmrest_sigma,a);
hhmeg=ttest_gretna(hmDecision_eg,hmrest_eg,a);
hhmeloc=ttest_gretna(hmDecision_eloc,hmrest_eloc,a);
hhmcp=ttest_gretna(hmDecision_cp,hmrest_cp,a);
hhmlp=ttest_gretna(hmDecision_lp,hmrest_lp,a);
hhmsigma=ttest_gretna(hmDecision_sigma,hmrest_sigma,a);
```

Plotting 10 plots for LM and HM for 5 parameters

```
leg={'Decision','Rest'};
figure('WindowState', 'maximized')
subplot(2,5,1)
fntsize=16;
plotting_gretna_with_sig(lmDecision_eg,lmrest_eg,hlmeg,leg),
ylabel('Eg','FontSize',fntsize,"FontWeight","bold")
subplot(2,5,2)
plotting_gretna_with_sig(lmDecision_eloc,lmrest_eloc,hlmeloc,leg),
ylabel('Eloc','FontSize',fntsize,'FontWeight',"bold")
subplot(2,5,3)
plotting_gretna_with_sig(lmDecision_cp,lmrest_cp,hlmcp,leg),
ylabel('Cp','FontSize',fntsize,'FontWeight',"bold")
subplot(2,5,4)
plotting_gretna_with_sig(lmDecision_lp,lmrest_lp,hlmlp,leg),
ylabel('Lp','FontSize',fntsize,'FontWeight',"bold")
subplot(2,5,5)
plotting_gretna_with_sig(lmDecision_sigma,lmrest_sigma,hlmsigma,leg),
ylabel('Sigma','FontSize',fntsize,'FontWeight',"bold")
subplot(2,5,6)
plotting_gretna_with_sig(hmDecision_eg,hmrest_eg,hhmeg,leg),
ylabel('Eg','FontSize',fntsize,'FontWeight',"bold")
subplot(2,5,7)
plotting_gretna_with_sig(hmDecision_eloc,hmrest_eloc,hhmeloc,leg),
ylabel('Eloc','FontSize',fntsize,'FontWeight',"bold")
subplot(2,5,8)
plotting_gretna_with_sig(hmDecision_cp,hmrest_cp,hhmcp,leg),
```

```
ylabel('Cp','FontSize',fntsize,'FontWeight',"bold")
subplot(2,5,9)
plotting_gretna_with_sig(hmDecision_lp,hmrest_lp,hhmlp,leg),
ylabel('Lp','FontSize',fntsize,"FontWeight","bold")
subplot(2,5,10)
plotting_gretna_with_sig(hmDecision_sigma,hmrest_sigma,hhmsigma,leg),
ylabel('Sigma','FontSize',fntsize,'FontWeight',"bold")
```

Comparing Decision vs rest for all subjects

```
decision_eg=cat(1,lmDecision_eg,hmDecision_eg);
decision_eloc=cat(1,lmDecision_eloc,hmDecision_eloc);
decision_cp=cat(1,lmDecision_cp,hmDecision_cp);
decision_lp=cat(1,lmDecision_lp,hmDecision_lp);
decision_sigma=cat(1,lmDecision_sigma,hmDecision_sigma);

rest_eg=cat(1,lmrest_eg,hmrest_eg);
rest_eloc=cat(1,lmrest_eloc,hmrest_eloc);
rest_cp=cat(1,lmrest_cp,hmrest_cp);
rest_lp=cat(1,lmrest_lp,hmrest_lp);
rest_sigma=cat(1,lmrest_sigma,hmrest_sigma);
```

Plotting Decision vs Rest

```
a=0.001;
heg=ttest_gretna(decision_eg,rest_eg,a);
heloc=ttest_gretna(decision_eloc,rest_eloc,a);
hcp=ttest_gretna(decision_cp,rest_cp,a);
hlp=ttest_gretna(decision_lp,rest_lp,a);
hsigma=ttest_gretna(decision_sigma,rest_sigma,a);

leg={'Decision','Rest'};
figure('WindowState', 'maximized')
subplot(2,3,1)
fntsize=16;
plotting_gretna_with_sig(decision_eg,rest_eg,heg,leg),
ylabel('Eg','FontSize',fntsize,"FontWeight","bold")
subplot(2,3,2)
plotting_gretna_with_sig(decision_eloc,rest_eloc,heloc,leg),
ylabel('Eloc','FontSize',fntsize,'FontWeight',"bold")
subplot(2,3,3)
plotting_gretna_with_sig(decision_cp,rest_cp,hcp,leg),
ylabel('Cp','FontSize',fntsize,'FontWeight',"bold")
subplot(2,3,4)
plotting_gretna_with_sig(decision_lp,rest_lp,hlp,leg),
ylabel('Lp','FontSize',fntsize,'FontWeight',"bold")
subplot(2,3,5)
plotting_gretna_with_sig(decision_sigma,rest_sigma,hsigma,leg),
ylabel('Sigma','FontSize',fntsize,'FontWeight',"bold")
```

```
yticks([0 1 2 3 4]);
yticklabels({'0','1','2','3','4'});
```

Published with MATLAB® R2019b

C. Chapter 3: Power Calculation (Aim 2a & Aim 2b)

```
close all
clear
clc
```

Calculating power for tpbm and pbo

```
% subjects for analysis
sub1=1:26;
sub2= 1:23;
fs= 256; % sampling frequency

% Calculating power using v^2; tls is for tPBM pbo is for pbo
[tls, pbo]= power_calc(sub1,sub2, fs);

% Removing bad subjects data
tls(:,:,:,[4,10,15])=[];
pbo(:,:,:,[4,10,15])=[];

diff= tls-pbo;
mdiff=mean(diff,4);
```

mean

```
for jj=1:5
    FigH = figure('Position', get(0, 'Screensize'),'Name',['Band ' num2str(jj) ]);
    F    = getframe(FigH);
    for kk= 1:2
        subplot(1,2,kk)
        EEG = pop_loadset('filename','ICA.set');
        topoplot(mdiff(:,jj,kk), EEG.chanlocs), title([' Minute - ' num2str(kk) ]);
        set(gca,'Clim',[-0.1 0.1]);
    end
    %saveas(gcf,['4by4_Power tls ' num2str(jj) '.png']);
end
```

ttest - tls

```
for j=1:5
    for t=1:2
        for ch=1:64
            data= diff(ch,j,t,:);
            [h(ch,j,t),p(ch,j,t),~, stat1]= ttest(data,0);
            ttempt1(ch,j,t)= stat1.tstat;

            if abs(ttempt1(ch,j,t))< 1.684
                ttemp1(ch,j,t)= 0;
            else
                ttemp1(ch,j,t)= ttempt1(ch,j,t);
            end
        end
    end
end
```

plotting t for tls

```
for j=1:5
    figure
    for t=1:2
        subplot(1,2,t)
        topoplot_dc(ttemp1(:,j,t),EEG.chanlocs);
    end
    saveas(gcf,['4by4_Power tls ttest_NODAL ' num2str(j) '.png']);
end
for jj=1:5
    FigH = figure('Position', get(0, 'Screensize'),'Name',['Band ' num2str(jj) ]);
    F    = getframe(FigH);
    for kk= 1:2
        subplot(1,2,kk)
        EEG = pop_loadset('filename','ICA.set');
        topoplot(ttemp1(:,jj,kk), EEG.chanlocs), title([' Minute - ' num2str(kk) ]);
        set(gca,'fontsize',15);
        set(gca,'Clim',[-2.5 2.5]);
    end
    %   saveas(gcf,['4by4_Power tls ttest ' num2str(jj) '.png']);
end
```

Published with MATLAB® R2019b

D. Chapter 4 - Trend Mapping oxy hemoglobin (Aim 3a)

```
clear
close all
clc
```

```
sub=[1:14 16:18];
addpath(genpath('d:\fNIRS TIBS\'));

% smoothing
[OxyTibs,OxyPbo] = oxy_Data(sub);
[DxyTibs,DxyPbo] = dxy_Data(sub);
```

t-test

```
for i=1:size(OxyTibs,1)
    for ii=1:12
        [h(i,ii),~]= ttest(OxyTibs(i,ii,:),OxyPbo(i,ii,:));
    end
end
h1= h*0.0175;
```

```
for i=1:size(h1,1)
    for ii=1:12
        if h1(i,ii)==0
            h1(i,ii)=NaN;
        end
    end

end
```

```
meanOTibs = mean(OxyTibs,3)*10^3;
meanOPbo = mean(OxyPbo,3)*10^3;
meanDTibs = mean(DxyTibs,3)*10^3;
meanDPbo = mean(DxyPbo,3)*10^3;

xl=linspace(0, 11.5, 7576)';
```

Plotting

```
FigH = figure('Position', get(0, 'Screensize'),'Name','Averaged subjects' );
F    = getframe(FigH);
cc=[1:8];
for ch= 1:length(cc)
    subplot(2,4,ch)
    v = [0 -8; 8 -8; 8 40; 0 40];
    f = [1 2 3 4];
    patch('Faces',f,'Vertices',v,'FaceColor',[0.0 0.3 0.8], 'EdgeColor', 'none', 'FaceAlpha',0.3,
'HandleVisibility','off'), hold on
    plot(xl,meanOTibs(:,cc(ch)),'r','LineWidth',2);
    plot(xl,meanOPbo(:,cc(ch)),'--r','LineWidth',2);
    title(['Channel ' num2str(cc(ch)) ]);
    xlabel('Time (min)','FontSize',20,'FontWeight','bold');
    ylabel('\Delta [HbO](\muM)','FontSize',14,'FontWeight','bold');
```

```
    box on

    ax = gca;
    set(findobj(gca,'type','line'),'linew',2)
    set(gcf, 'renderer', 'opengl')
    set(ax,'LineWidth',2)
    set(gca,'Fontsize', 16);
    xlim([0 12]);
    ylim([-8 18]);
    xticks([0 4 8 12]);
    ax.FontSize = 20;

    hold off
end

legend('HbO-tPBM','HbO-sham','HbR-tPBM','HbR-placebo','location','North',
'orientation','vertical', 'Fontsize', 14);
```

Published with MATLAB® R2019b

E. Connectivity Analysis (Aim 3b)

```
close all
clear
clc
```

```
sub =[1:19];
for k=1:length(sub)
    load(['TRT_sub' num2str(sub(k)) '.nirs'],'-mat');
    tibs1= procResult.dc(4848:12053,1,:)/10^6;
    [x, y, z] = size(tibs1);
```

```
    tibs=reshape(tibs1,[x z]);

    load(['PBO_sub' num2str(sub(k)) '.nirs'],'-mat');
    pbo1= procResult.dc(4848:12053,1,:);
    pbo=reshape(pbo1,[x z]);
    fs=10.10;
    clear aux d ml procInput procResult s SD t tIncMan userdata tibs1 pbo1 x y z

    j=1;
    for ii=1:.5:11
        tibs_chunk(:,:,j)= tibs(((ii-1)*60*fs)+1:(ii*60*fs),:);
        pbo_chunk(:,:,j)= pbo(((ii-1)*60*fs)+1:(ii*60*fs),:);
        j=j+1;
    end

    for kk=1:size(tibs_chunk,3)
        tibs_corr(:,:,kk,k)= atanh(corr(tibs_chunk(:,:,kk)));
        pbo_corr(:,:,kk,k)= atanh(corr(pbo_chunk(:,:,kk)));
    end
end

tibs_cc= tanh(tibs_corr);
pbo_cc= tanh(pbo_corr);


for i=1:111
    for iii=1:111
        for iv= 1:size(pbo_chunk,3)
            for v=1:19
                if tibs_corr(i,iii,iv,v)== inf
                    tibs_corr(i,iii,iv,v)=0;
                end
                if pbo_corr(i,iii,iv,v)== inf
                    pbo_corr(i,iii,iv,v)=0;
                end
            end
        end
    end
end
```

Compare tibs vs pbo paired ttest

```
for i=1:111
    for j=1:111
        for iv=1:size(pbo_chunk,3)
            data=tibs_corr(i,j,iv,:)-pbo_corr(i,j,iv,:);
            [h(i,j,iv), ~]= ttest(data,0, 'alpha',0.01,'tail','right');
        end
    end
end
```

```
for i=1:111
    for iii=1:111
        for iv= 1:size(pbo_chunk,3)
            if isnan(h(i,iii,iv))
                h(i,iii,iv)=0;
            end
        end
    end
end
```

Sum of connections

```
sumc=reshape(sum(sum(h)),[size(pbo_chunk,3),1])/2;
```

variance calculation

```
var_tb= var(tibs_corr,0,3);
var_pb= var(pbo_corr,0,3);
for i=1:19
    mask = tril(true(size(var_tb(:,:,1,i))),-1);
    out_tb1=var_tb(:,:,1,i);
    out_tb = out_tb1(mask);
    mtb(i,:)= mean(out_tb);
    out_pb1=var_pb(:,:,1,i);
    out_pb= out_pb1(mask);
    mpb(i,:)=mean(out_pb);
end

[h, c2]= ttest(mtb,mpb);
varm= [mean(mtb) mean(mpb)];
stdv= [std(mtb) std(mpb)];
c={'tPBM','sham'};
c1= 1;
```

Plotting

```
figure
x=1:0.5:11;
plot(x,sumc, 'r*-', 'LineWidth',2); hold on
line([8 8],[0 120],'LineStyle','--','Color','k','LineWidth',2);
ax=gca;
ax.LineWidth=4;
xlim([0 11.5]);
set(gca, 'fontsize',16);
xlabel(' Time (min)');
ylabel('Number of Connections');
```

```
str = {'Stimulation'};
annotation('textbox','String',str,'FitBoxToText','on','FontSize',16);
str = {'Post-Stimulation'};
annotation('textbox','String',str,'FitBoxToText','on','FontSize',16);
```

Published with MATLAB® R2019b

Reference

[1] M. Cazzell, L. Li, Z.-J. Lin, S. J. Patel, and H. Liu, "Comparison of neural correlates of risk decision making between genders: An exploratory fNIRS study of the Balloon Analogue Risk Task (BART)," *NeuroImage,* vol. 62, no. 3, pp. 1896-1911, 2012/09/01/ 2012, doi: 10.1016/j.neuroimage.2012.05.030.

[2] U. Benzion, Y. Cohen, R. Peled, and T. Shavit, "Decision-making and the newsvendor problem: an experimental study," (in en), *J Oper Res Soc,* vol. 59, no. 9, pp. 1281-1287, 2008/09/01/ 2008, doi: 10.1057/palgrave.jors.2602470.

[3] L. Kocsis, P. Herman, and A. Eke, "The modified Beer-Lambert law revisited," *Phys Med Biol,* vol. 51, no. 5, pp. N91-8, Mar 7 2006, doi: 10.1088/0031-9155/51/5/N02.

[4] F. Scholkmann *et al.*, "A review on continuous wave functional near-infrared spectroscopy and imaging instrumentation and methodology," *Neuroimage,* vol. 85 Pt 1, pp. 6-27, Jan 15 2014, doi: 10.1016/j.neuroimage.2013.05.004.

[5] C. Kolyva *et al.*, "Systematic investigation of changes in oxidized cerebral cytochrome c oxidase concentration during frontal lobe activation in healthy adults," *Biomedical optics express,* vol. 3, no. 10, pp. 2550-66, Oct 1 2012, doi: 10.1364/BOE.3.002550.

[6] H. Gaspars-Wieloch, "Newsvendor problem under complete uncertainty: a case of innovative products," (in en), *Cent Eur J Oper Res,* vol. 25, no. 3, pp. 561-585, 2017/09/01/ 2017, doi: 10.1007/s10100-016-0458-3.

[7] A. L. Krain, A. M. Wilson, R. Arbuckle, F. X. Castellanos, and M. P. Milham, "Distinct neural mechanisms of risk and ambiguity: A meta-analysis of decision-making," *NeuroImage,* vol. 32, no. 1, pp. 477-484, 2006/08/01/ 2006, doi: 10.1016/j.neuroimage.2006.02.047.

[8] C. Declerck and C. Boone, *Neuroeconomics of Prosocial Behavior: The Compassionate Egoist*. Academic Press (in en), 2015, p. 187.

[9] D. C. Farrar, A. Z. Mian, A. E. Budson, M. B. Moss, and R. J. Killiany, "Functional brain networks involved in decision-making under certain and uncertain conditions," *Neuroradiology,* vol. 60, no. 1, pp. 61-69, 2018/01// 2018, doi: 10.1007/s00234-017-1949-1.

[10] D. W. Barrett and F. Gonzalez-Lima, "Transcranial infrared laser stimulation produces beneficial cognitive and emotional effects in humans," (in en), *Neuroscience,* vol. 230, pp. 13-23, 2013/01/29/ 2013, doi: 10.1016/j.neuroscience.2012.11.016.

[11] N. J. Blanco, C. L. Saucedo, and F. Gonzalez-Lima, "Transcranial infrared laser stimulation improves rule-based, but not information-integration, category learning in humans," *Neurobiology of Learning and Memory,* vol. 139, pp. 69-75, 2017/03/01/ 2017, doi: https://doi.org/10.1016/j.nlm.2016.12.016.

[12] N. J. Blanco, W. T. Maddox, and F. Gonzalez-Lima, "Improving executive function using transcranial infrared laser stimulation," *Journal of Neuropsychology,* vol. 11, no. 1, pp. 14-25, 2017/03/01/ 2017, doi: 10.1111/jnp.12074.

[13] E. Vargas *et al.*, "Beneficial neurocognitive effects of transcranial laser in older adults," *Lasers Med Sci,* vol. 32, no. 5, pp. 1153-1162, Jul 2017, doi: 10.1007/s10103-017-2221-y.

[14] X. Wang, F. Tian, S. S. Soni, F. Gonzalez-Lima, and H. Liu, "Interplay between up-regulation of cytochrome-c-oxidase and hemoglobin oxygenation induced by near-infrared laser," *Scientific Reports,* vol. 6, no. 1, p. 30540, 2016/08/03 2016, doi: 10.1038/srep30540.

[15] Q. Wu, X. Wang, H. Liu, and L. Zeng, "Learning Hemodynamic Effect of Transcranial Infrared Laser Stimulation Using Longitudinal Data Analysis," *IEEE Journal of Biomedical and Health Informatics,* pp. 1-1, 2019, doi: 10.1109/JBHI.2019.2951772.

[16] X. Wang *et al.*, "Transcranial photobiomodulation with 1064-nm laser modulates brain electroencephalogram rhythms," (in en), *NPh,* vol. 6, no. 02, p. 1, 2019/06/13/ 2019, doi: 10.1117/1.NPh.6.2.025013.

[17] H. Chung, T. Dai, S. K. Sharma, Y. Y. Huang, J. D. Carroll, and M. R. Hamblin, "The nuts and bolts of low-level laser (light) therapy," *Ann Biomed Eng,* vol. 40, no. 2, pp. 516-33, Feb 2012, doi: 10.1007/s10439-011-0454-7.

[18] F. Tian, S. N. Hase, F. Gonzalez-Lima, and H. Liu, "Transcranial laser stimulation improves human cerebral oxygenation," *Lasers Surg Med,* vol. 48, no. 4, pp. 343-9, Apr 2016, doi: 10.1002/lsm.22471.

[19] X. Wang, J. Dmochowski, M. Husain, F. Gonzalez-Lima, and H. Liu, "Proceedings #18. Transcranial Infrared Brain Stimulation Modulates EEG Alpha Power," *Brain Stimulation,* vol. 10, no. 4, pp. e67-e69, 2017/07/01/ 2017, doi: https://doi.org/10.1016/j.brs.2017.04.111.

[20] V. Spera *et al.*, "Transcranial Near-Infrared Light: Dose-Dependent Effects on EEG Oscillations but not Cerebral Blood Flow," *bioRxiv,* p. 837591, 2019, doi: 10.1101/837591.

[21] R. Zomorrodi, G. Loheswaran, A. Pushparaj, and L. Lim, "Pulsed Near Infrared Transcranial and Intranasal Photobiomodulation Significantly Modulates Neural Oscillations: a pilot exploratory study," *Sci Rep,* vol. 9, no. 1, p. 6309, Apr 19 2019, doi: 10.1038/s41598-019-42693-x.

[22] A. C. Chen, W. Feng, H. Zhao, Y. Yin, and P. Wang, "EEG default mode network in the human brain: spectral regional field powers," *Neuroimage,* vol. 41, no. 2, pp. 561-74, Jun 2008, doi: 10.1016/j.neuroimage.2007.12.064.

[23] M. Hsu, M. Bhatt, R. Adolphs, D. Tranel, and C. F. Camerer, "Neural systems responding to degrees of uncertainty in human decision-making," *Science,* vol. 310, no. 5754, pp. 1680-3, Dec 9 2005, doi: 10.1126/science.1115327.

[24] D. A. Boas, A. M. Dale, and M. A. Franceschini, "Diffuse optical imaging of brain activation: approaches to optimizing image sensitivity, resolution, and accuracy," *Neuroimage,* vol. 23 Suppl 1, pp. S275-88, 2004, doi: 10.1016/j.neuroimage.2004.07.011.

[25] M. Cazzell, L. Li, Z. J. Lin, S. J. Patel, and H. Liu, "Comparison of neural correlates of risk decision making between genders: an exploratory fNIRS study of the Balloon Analogue Risk Task (BART)," *Neuroimage,* vol. 62, no. 3, pp. 1896-911, Sep 2012, doi: 10.1016/j.neuroimage.2012.05.030.

[26] D. A. Boas, C. E. Elwell, M. Ferrari, and G. Taga, "Twenty years of functional near-infrared spectroscopy: introduction for the special issue," *Neuroimage,* vol. 85 Pt 1, pp. 1-5, Jan 15 2014, doi: 10.1016/j.neuroimage.2013.11.033.

[27] Y. Cohen, R. Peled, and T. Shavit, "Decision-making and the newsvendor problem: an experimental study," *J. Oper. Res. Soc.,* vol. 59, no. 9, pp. 1281–1287, 2008.

[28] E. Bullmore and O. Sporns, "Complex brain networks: graph theoretical analysis of structural and functional systems," *Nature reviews. Neuroscience,* vol. 10, no. 3, pp. 186-98, Mar 2009, doi: 10.1038/nrn2575.

[29] X. H. Liao *et al.*, "Functional brain hubs and their test-retest reliability: a multiband resting-state functional MRI study," *NeuroImage,* vol. 83, pp. 969-82, Dec 2013, doi: 10.1016/j.neuroimage.2013.07.058.

[30] U. Braun *et al.*, "Test-retest reliability of resting-state connectivity network characteristics using fMRI and graph theoretical measures," *NeuroImage,* vol. 59, no. 2, pp. 1404-12, Jan 16 2012, doi: 10.1016/j.neuroimage.2011.08.044.

[31] M. Rubinov and O. Sporns, "Complex network measures of brain connectivity: uses and interpretations," *NeuroImage,* vol. 52, no. 3, pp. 1059-69, Sep 2010, doi: 10.1016/j.neuroimage.2009.10.003.

[32] D. J. Kim *et al.*, "Disturbed resting state EEG synchronization in bipolar disorder: A graph-theoretic analysis," *NeuroImage. Clinical,* vol. 2, pp. 414-23, 2013, doi: 10.1016/j.nicl.2013.03.007.

[33] F. Vecchio, F. Miraglia, and P. Maria Rossini, "Connectome: Graph theory application in functional brain network architecture," *Clinical Neurophysiology Practice,* vol. 2, pp. 206-213, 2017/01/01/ 2017, doi: https://doi.org/10.1016/j.cnp.2017.09.003.

[34] O. Sporns, G. Tononi, and R. Kötter, "The Human Connectome: A Structural Description of the Human Brain," *PLOS Computational Biology,* vol. 1, no. 4, p. e42, 2005, doi: 10.1371/journal.pcbi.0010042.

[35] G. A. Pavlopoulos *et al.*, "Using graph theory to analyze biological networks," (in eng), *BioData Min,* vol. 4, pp. 10-10, 2011, doi: 10.1186/1756-0381-4-10.

[36] H. Niu, J. Wang, T. Zhao, N. Shu, and Y. He, "Revealing topological organization of human brain functional networks with resting-state functional near infrared spectroscopy," *PloS one,* vol. 7, no. 9, p. e45771, 2012, doi: 10.1371/journal.pone.0045771.

[37] H. Niu and Y. He, "Resting-state functional brain connectivity: lessons from functional near-infrared spectroscopy," *Neuroscientist,* vol. 20, no. 2, pp. 173-88, Apr 2014, doi: 10.1177/1073858413502707.

[38] L. Li *et al.*, "Whole-cortical graphical networks at wakeful rest in young and older adults revealed by functional near-infrared spectroscopy," *Neurophotonics,* vol. 5, no. 3, p. 035004, Jul 2018, doi: 10.1117/1.NPh.5.3.035004.

[39] M. E. Schweitzer and G. P. Cachon, "Decision Bias in the Newsvendor Problem with a Known Demand Distribution: Experimental Evidence," *Management Science,* vol. 46, no. 3, pp. 404-420, 2000/03/01/ 2000, doi: 10.1287/mnsc.46.3.404.12070.

[40] P. Cacola, N. Getchell, D. Srinivasan, G. Alexandrakis, and H. Liu, "Cortical activity in fine-motor tasks in children with Developmental Coordination Disorder: A preliminary fNIRS study," *Int J Dev Neurosci,* vol. 65, pp. 83-90, Apr 2018, doi: 10.1016/j.ijdevneu.2017.11.001.

[41] S. B. Erdoğan, M. A. Yücel, and A. Akın, "Analysis of task-evoked systemic interference in fNIRS measurements: Insights from fMRI," *NeuroImage,* vol. 87, pp. 490-504, 2014/02/15/ 2014, doi: 10.1016/j.neuroimage.2013.10.024.

[42] T. Nguyen, O. Babawale, T. Kim, H. J. Jo, H. Liu, and J. G. Kim, "Exploring brain functional connectivity in rest and sleep states: a fNIRS study," *Sci Rep,* vol. 8, no. 1, p. 16144, Nov 1 2018, doi: 10.1038/s41598-018-33439-2.

[43] P. Smielewski, M. Czosnyka, J. D. Pickard, and P. Kirkpatrick, "Clinical evaluation of near-infrared spectroscopy for testing cerebrovascular reactivity in patients with carotid artery disease," *Stroke,* vol. 28, no. 2, pp. 331-8, Feb 1997, doi: 10.1161/01.str.28.2.331.

[44] A. Oldag *et al.*, "Assessment of cortical hemodynamics by multichannel near-infrared spectroscopy in steno-occlusive disease of the middle cerebral artery," *Stroke,* vol. 43, no. 11, pp. 2980-5, Nov 2012, doi: 10.1161/STROKEAHA.112.656710.

[45] E. L. Urquhart, X. Wang, H. Liu, P. J. Fadel, and G. Alexandrakis, "Differences in Net Information Flow and Dynamic Connectivity Metrics Between Physically Active and Inactive Subjects Measured by Functional Near-Infrared Spectroscopy (fNIRS) During a Fatiguing Handgrip Task," *Frontiers in Neuroscience,* 10.3389/fnins.2020.00167 vol. 14, p. 167, 2020. [Online]. Available: https://www.frontiersin.org/article/10.3389/fnins.2020.00167.

[46] V. D. Calhoun, T. Adali, V. B. McGinty, J. J. Pekar, T. D. Watson, and G. D. Pearlson, "fMRI Activation in a Visual-Perception Task: Network of Areas Detected Using the General Linear Model and Independent Components Analysis," *NeuroImage,* vol. 14, no. 5, pp. 1080-1088, 2001/11/01/ 2001, doi: https://doi.org/10.1006/nimg.2001.0921.

[47] V. D. Calhoun, M. C. Stevens, G. D. Pearlson, and K. A. Kiehl, "fMRI analysis with the general linear model: removal of latency-induced amplitude bias by incorporation of hemodynamic derivative terms," *NeuroImage,* vol. 22, no. 1, pp. 252-257, 2004/05/01/ 2004, doi: https://doi.org/10.1016/j.neuroimage.2003.12.029.

[48] F. Tian, A. Yennu, A. Smith-Osborne, F. Gonzalez-Lima, C. S. North, and H. Liu, "Prefrontal responses to digit span memory phases in patients with post-traumatic stress disorder (PTSD): A functional near infrared spectroscopy study," *NeuroImage. Clinical,* vol. 4, pp. 808-19, 2014, doi: 10.1016/j.nicl.2014.05.005.

[49] Z. J. Lin, L. Li, M. Cazzell, and H. Liu, "Atlas-guided volumetric diffuse optical tomography enhanced by generalized linear model analysis to image risk decision-making responses in young adults," *Hum Brain Mapp,* vol. 35, no. 8, pp. 4249-66, Aug 2014, doi: 10.1002/hbm.22459.

[50] M. L. Schroeter *et al.*, "Towards a standard analysis for functional near-infrared imaging," *NeuroImage,* vol. 21, no. 1, pp. 283-290, 2004/01/01/ 2004, doi: 10.1016/j.neuroimage.2003.09.054.

[51] F. Tian, Z.-J. Lin, and H. Liu, "EasyTopo: A Toolbox for Rapid Diffuse Optical Topography Based on a Standard Template of Brain Atlas," B. J. Tromberg, A. G. Yodh, and E. M. Sevick-Muraca, Eds., 2013/03// 2013, p. 85782J, doi: 10.1117/12.2003907.

[52] J. A. Bondy and U. S. R. Murty, *Graph theory with applications*. Macmillan London, 1976.

[53] P. Erdös, "Graph Theory and Probability," (in en), *Canadian Journal of Mathematics,* vol. 11, pp. 34-38, 1959 ed 1959, doi: 10.4153/CJM-1959-003-9.

[54] Y. Iturria-Medina, R. C. Sotero, E. J. Canales-Rodríguez, Y. Alemán-Gómez, and L. Melie-García, "Studying the human brain anatomical network via diffusion-weighted MRI and Graph Theory," *NeuroImage,* vol. 40, no. 3, pp. 1064-1076, 2008/04/15/ 2008, doi: 10.1016/j.neuroimage.2007.10.060.

[55] D. S. Bassett, A. Meyer-Lindenberg, S. Achard, T. Duke, and E. Bullmore, "Adaptive reconfiguration of fractal small-world human brain functional networks," *Proc Natl Acad Sci USA,* vol. 103, no. 51, p. 19518, 2006/12/19/ 2006, doi: 10.1073/pnas.0606005103.

[56] S. Achard, R. Salvador, B. Whitcher, J. Suckling, and E. Bullmore, "A Resilient, Low-Frequency, Small-World Human Brain Functional Network with Highly Connected Association Cortical Hubs," (in en), *J. Neurosci.,* vol. 26, no. 1, pp. 63-72, 2006/01/04/ 2006, doi: 10.1523/JNEUROSCI.3874-05.2006.

[57] R. Salvador, J. Suckling, M. R. Coleman, J. D. Pickard, D. Menon, and E. Bullmore, "Neurophysiological Architecture of Functional Magnetic Resonance Images of Human Brain," (in en), *Cerebral Cortex,* vol. 15, no. 9, pp. 1332-1342, 2005/09/01/ 2005, doi: 10.1093/cercor/bhi016.

[58] Z. Hu, J. Zhang, L. Zhang, Y.-T. Xiang, and Z. Yuan, "Linking Brain Activation to Topological Organization in the Frontal Lobe as a Synergistic Indicator to Characterize the Difference between Various Cognitive Processes of Executive Functions," *Neurophotonics,* vol. 6, no. 02, p. 1, 2019/05// 2019, doi: 10.1117/1.NPh.6.2.025008.

[59] L. Cai, Q. Dong, and H. Niu, "The development of functional network organization in early childhood and early adolescence: A resting-state fNIRS study," *Dev Cogn Neurosci,* vol. 30, pp. 223-235, Apr 2018, doi: 10.1016/j.dcn.2018.03.003.

[60] J. Wang, X. Wang, M. Xia, X. Liao, A. Evans, and Y. He, "GRETNA: A Graph Theoretical Network Analysis Toolbox for Imaging Connectomics," (in English), *Frontiers in Human Neuroscience,* vol. 9, 2015 2015, doi: 10.3389/fnhum.2015.00386.

[61] S. Achard and E. Bullmore, "Efficiency and Cost of Economical Brain Functional Networks," (in en), *PLOS Computational Biology,* vol. 3, no. 2, p. e17, 2007/02/02/ 2007, doi: 10.1371/journal.pcbi.0030017.

[62] J. C. Ye, S. Tak, K. E. Jang, J. Jung, and J. Jang, "NIRS-SPM: statistical parametric mapping for near-infrared spectroscopy," *Neuroimage,* vol. 44, no. 2, pp. 428-47, Jan 15 2009, doi: 10.1016/j.neuroimage.2008.08.036.

[63] J. I. Gold and M. N. Shadlen, "The Neural Basis of Decision Making," (in en), *Annual Review of Neuroscience,* vol. 30, no. 1, pp. 535-574, 2007/07// 2007, doi: 10.1146/annurev.neuro.29.051605.113038.

[64] N. A. S. Farb, "Can neuroimaging inform economic theories of decision making," *Neuroscience and neuroeconomics.,* vol. 2, p. 1, 2013.

[65] A. Khani and G. Rainer, "Neural and neurochemical basis of reinforcement-guided decision making," *Journal of Neurophysiology,* vol. 116, no. 2, pp. 724-741, 2016/08/01 2016, doi: 10.1152/jn.01113.2015.

[66] A. Makwana and T. Hare, "Stop and be fair: DLPFC development contributes to social decision making," *Neuron,* vol. 73, no. 5, pp. 859-61, Mar 8 2012, doi: 10.1016/j.neuron.2012.02.010.

[67] D. Huang *et al.*, "Activation of the DLPFC Reveals an Asymmetric Effect in Risky Decision Making: Evidence from a tDCS Study," *Front Psychol,* vol. 8, p. 38, 2017, doi: 10.3389/fpsyg.2017.00038.

[68] G. F. Humphreys, P. Hoffman, M. Visser, R. J. Binney, and M. A. Lambon Ralph, "Establishing task- and modality-dependent dissociations between the semantic and default mode networks," *Proc Natl Acad Sci USA,* vol. 112, no. 25, p. 7857, 2015, doi: 10.1073/pnas.1422760112.

[69] M. Visser and M. A. Lambon Ralph, "Differential Contributions of Bilateral Ventral Anterior Temporal Lobe and Left Anterior Superior Temporal Gyrus to Semantic Processes," *Journal of Cognitive Neuroscience,* vol. 23, no. 10, pp. 3121-3131, 2011/10/01 2011, doi: 10.1162/jocn_a_00007.

[70] C. P. Kaller, B. Rahm, J. Spreer, C. Weiller, and J. M. Unterrainer, "Dissociable contributions of left and right dorsolateral prefrontal cortex in planning," (in eng), *Cereb. Cortex,* vol. 21, no. 2, pp. 307-317, 2011/02// 2011, doi: 10.1093/cercor/bhq096.

[71] E. Hoshi and J. Tanji, "Area-Selective Neuronal Activity in the Dorsolateral Prefrontal Cortex for Information Retrieval and Action Planning," *J. Neurophysiol.,* vol. 91, no. 6, pp. 2707-2722, 2004/06/01/ 2004, doi: 10.1152/jn.00904.2003.

[72] K. I. Bolla *et al.*, "Orbitofrontal cortex dysfunction in abstinent cocaine abusers performing a decision-making task," *NeuroImage,* vol. 19, no. 3, pp. 1085-1094, 2003/07/01/ 2003, doi: 10.1016/S1053-8119(03)00113-7.

[73] M. Bogdanov and L. Schwabe, "Transcranial Stimulation of the Dorsolateral Prefrontal Cortex Prevents Stress-Induced Working Memory Deficits," (in eng), *The Journal of Neuroscience: The Official Journal of the Society for Neuroscience,* vol. 36, no. 4, pp. 1429-1437, 2016/01/27/ 2016, doi: 10.1523/JNEUROSCI.3687-15.2016.

[74] S. Qin, E. J. Hermans, H. J. F. van Marle, J. Luo, and G. Fernández, "Acute Psychological Stress Reduces Working Memory-Related Activity in the Dorsolateral Prefrontal Cortex," *Biological Psychiatry,* vol. 66, no. 1, pp. 25-32, 2009/07// 2009, doi: 10.1016/j.biopsych.2009.03.006.

[75] E. C. Dias and M. A. Segraves, "Muscimol-induced inactivation of monkey frontal eye field: effects on visually and memory-guided saccades," *J Neurophysiol,* vol. 81, no. 5, pp. 2191-214, May 1999, doi: 10.1152/jn.1999.81.5.2191.

[76] S. Geng, X. Liu, B. B. Biswal, and H. Niu, "Effect of Resting-State fNIRS Scanning Duration on Functional Brain Connectivity and Graph Theory Metrics of Brain Network," *Front Neurosci,* vol. 11, p. 392, 2017, doi: 10.3389/fnins.2017.00392.

[77] E. L. Dennis *et al.*, "Test-Retest Reliability of Graph Theory Measures of Structural Brain Connectivity," in *Medical Image Computing and Computer-Assisted Intervention – MICCAI 2012*, Berlin, Heidelberg, N. Ayache, H. Delingette, P. Golland, and K. Mori, Eds., 2012// 2012: Springer Berlin Heidelberg, pp. 305-312.

[78] R. M. Hutchison *et al.*, "Dynamic functional connectivity: promise, issues, and interpretations," *Neuroimage,* vol. 80, pp. 360-78, Oct 15 2013, doi: 10.1016/j.neuroimage.2013.05.079.

[79] M. G. Preti, T. A. Bolton, and D. Van De Ville, "The dynamic functional connectome: State-of-the-art and perspectives," *Neuroimage,* vol. 160, pp. 41-54, Oct 15 2017, doi: 10.1016/j.neuroimage.2016.12.061.

[80] F. V. Farahani, W. Karwowski, and N. R. Lighthall, "Application of Graph Theory for Identifying Connectivity Patterns in Human Brain Networks: A Systematic Review," (in English), *Frontiers in Neuroscience,* Systematic Review vol. 13, no. 585, 2019-June-06 2019, doi: 10.3389/fnins.2019.00585.

[81] O. Sporns, "Network attributes for segregation and integration in the human brain," *Current Opinion in Neurobiology,* vol. 23, no. 2, pp. 162-171, 2013/04/01/ 2013, doi: https://doi.org/10.1016/j.conb.2012.11.015.

[82] J. Golbeck, "Chapter 3 - Network Structure and Measures," in *Analyzing the Social Web*, J. Golbeck Ed. Boston: Morgan Kaufmann, 2013, pp. 25-44.

[83] Y. Iturria-Medina, R. C. Sotero, E. J. Canales-Rodríguez, Y. Alemán-Gómez, and L. Melie-García, "Studying the human brain anatomical network via diffusion-weighted MRI and Graph Theory," (in eng), *Neuroimage,* vol. 40, no. 3, pp. 1064-76, Apr 15 2008, doi: 10.1016/j.neuroimage.2007.10.060.

[84] M. T. T. Wong-Riley *et al.*, "Photobiomodulation Directly Benefits Primary Neurons Functionally Inactivated by Toxins: ROLE OF CYTOCHROME c OXIDASE," *Journal of Biological Chemistry,* vol. 280, no. 6, pp. 4761-4771, 2005. [Online]. Available: http://www.jbc.org/content/280/6/4761.abstract.

[85] F. Gonzalez-Lima and D. W. Barrett, "Augmentation of cognitive brain functions with transcranial lasers," *Front Syst Neurosci,* vol. 8, p. 36, 2014, doi: 10.3389/fnsys.2014.00036.

[86] P. Cassano, "Transcranial Photobiomodulation for Psychiatric Disorders: Past and Future Directions," in *2018 Conference on Lasers and Electro-Optics (CLEO)*, 13-18 May 2018 2018, pp. 1-2.

[87] M. A. Naeser, A. Saltmarche, M. H. Krengel, M. R. Hamblin, and J. A. Knight, "Improved cognitive function after transcranial, light-emitting diode treatments in chronic, traumatic brain injury: two case reports," *Photomed Laser Surg,* vol. 29, no. 5, pp. 351-8, May 2011, doi: 10.1089/pho.2010.2814.

[88] M. A. Naeser *et al.*, "Significant improvements in cognitive performance post-transcranial, red/near-infrared light-emitting diode treatments in chronic, mild traumatic brain injury: open-protocol study," *J Neurotrauma,* vol. 31, no. 11, pp. 1008-17, Jun 1 2014, doi: 10.1089/neu.2013.3244.

[89] T. Pruitt, X. Wang, A. Wu, E. Kallioniemi, M. M. Husain, and H. Liu, "Transcranial Photobiomodulation (tPBM) With 1,064-nm Laser to Improve Cerebral Metabolism of the Human Brain In Vivo," *Lasers Surg Med,* Mar 15 2020, doi: 10.1002/lsm.23232.

[90] X. Wang, D. D. Reddy, S. S. Nalawade, S. Pal, F. Gonzalez-Lima, and H. Liu, "Impact of heat on metabolic and hemodynamic changes in transcranial infrared laser stimulation measured by broadband near-infrared spectroscopy," *NPh,* vol. 5, no. 1, p. 011004, 2017/09// 2017, doi: 10.1117/1.NPh.5.1.011004.

[91] M. H. Berman, M. R. Hamblin, and P. Chazot, "Chapter 4 - Photobiomodulation and Other Light Stimulation Procedures," in *Rhythmic Stimulation Procedures in Neuromodulation*, J. R. Evans and R. P. Turner Eds.: Academic Press, 2017, pp. 97-129.

[92] Y. Yao, Z. Lian, W. Liu, and Q. Shen, "Experimental study on physiological responses and thermal comfort under various ambient temperatures," *Physiology & Behavior,* vol. 93, no. 1, pp. 310-321, 2008/01/28/ 2008, doi: https://doi.org/10.1016/j.physbeh.2007.09.012.

[93] X. Wang *et al.*, "Up-regulation of cerebral cytochrome-c-oxidase and hemodynamics by transcranial infrared laser stimulation: A broadband near-infrared spectroscopy study," *J Cereb Blood Flow Metab,* vol. 37, no. 12, pp. 3789-3802, Dec 2017, doi: 10.1177/0271678X17691783.

[94] J. L. Cantero, M. Atienza, and R. M. Salas, "Human alpha oscillations in wakefulness, drowsiness period, and REM sleep: different electroencephalographic phenomena within the alpha band," *Neurophysiol Clin,* vol. 32, no. 1, pp. 54-71, Jan 2002, doi: 10.1016/s0987-7053(01)00289-1.

[95] S. Palva and J. M. Palva, "New vistas for alpha-frequency band oscillations," *Trends Neurosci,* vol. 30, no. 4, pp. 150-8, Apr 2007, doi: 10.1016/j.tins.2007.02.001.

[96] S. Hanslmayr, J. Gross, W. Klimesch, and K. L. Shapiro, "The role of alpha oscillations in temporal attention," *Brain Res Rev,* vol. 67, no. 1-2, pp. 331-43, Jun 24 2011, doi: 10.1016/j.brainresrev.2011.04.002.

[97] W. Klimesch, "EEG-alpha rhythms and memory processes," *Int J Psychophysiol,* vol. 26, no. 1-3, pp. 319-40, Jun 1997, doi: 10.1016/s0167-8760(97)00773-3.

[98] M. Steriade, P. Gloor, R. R. Llinas, F. H. Lopes de Silva, and M. M. Mesulam, "Report of IFCN Committee on Basic Mechanisms. Basic mechanisms of cerebral rhythmic activities," *Electroencephalogr Clin Neurophysiol,* vol. 76, no. 6, pp. 481-508, Dec 1990, doi: 10.1016/0013-4694(90)90001-z.

[99] M. Hosťovecký and B. Babušiak, "Brain activity: beta wave analysis of 2D and 3D serious games using EEG," (in English), *Journal of Applied Mathematics, Statistics and Informatics,* vol. 13, no. 2, pp. 39-53, 2017, doi: https://doi.org/10.1515/jamsi-2017-0008.

[100] W. J. Ray and H. W. Cole, "EEG alpha activity reflects attentional demands, and beta activity reflects emotional and cognitive processes," *Science,* vol. 228, no. 4700, pp. 750-2, May 10 1985, doi: 10.1126/science.3992243.

[101] A. Breton, V. Ronca, A. I. Mallet-Dacosta, F. Longatte, R. Servajean-Hilst, and Y. Attal, "Identifying the neural signature of thermic comfort sensation: neuroergonomic evaluation of a new ventilating system integrated in car seat," (in English), *Human Neuroscience Archive,* Abstract, doi: 10.3389/conf.fnhum.2018.227.00008.

[102] H. Olausson *et al.*, "Cortical activation by tactile and painful stimuli in hemispherectomized patients," *Brain,* vol. 124, no. Pt 5, pp. 916-27, May 2001, doi: 10.1093/brain/124.5.916.

[103] C. Babiloni *et al.*, "Resting state cortical electroencephalographic rhythms are related to gray matter volume in subjects with mild cognitive impairment and Alzheimer's disease," *Hum Brain Mapp,* vol. 34, no. 6, pp. 1427-46, Jun 2013, doi: 10.1002/hbm.22005.

[104] S. K. Lal and A. Craig, "Driver fatigue: electroencephalography and psychological assessment," *Psychophysiology,* vol. 39, no. 3, pp. 313-21, May 2002, doi: 10.1017/s0048577201393095.

[105] S. K. Lal and A. Craig, "Reproducibility of the spectral components of the electroencephalogram during driver fatigue," *Int J Psychophysiol,* vol. 55, no. 2, pp. 137-43, Feb 2005, doi: 10.1016/j.ijpsycho.2004.07.001.

[106] G. G. Knyazev, "EEG delta oscillations as a correlate of basic homeostatic and motivational processes," *Neuroscience & Biobehavioral Reviews,* vol. 36, no. 1, pp. 677-695, 2012.

[107] E. Shufman *et al.*, "Electro-encephalography spectral analysis of heroin addicts compared with abstainers and normal controls," *Isr J Psychiatry Relat Sci,* vol. 33, no. 3, pp. 196-206, 1996. [Online]. Available: http://www.ncbi.nlm.nih.gov/pubmed/9009520.

[108] V. Synytsky, G. Gruzdev, G. Trofimchouk, V. Voronovskaya, I. Tetko, and A. Villa, "Neurophysiological and psychophysiological effects of sulpiride in the norm and in patients with opiate addiction," *Neurophysiology,* vol. 34, no. 4, pp. 313-320, 2002.

[109] N. P. Bechtereva, *Psychophysiology: Today and Tomorrow*. Elsevier (in en), 2013, p. 274.

[110] B. Bromm and J. Lorenz, "Neurophysiological evaluation of pain," *Electroencephalogr Clin Neurophysiol,* vol. 107, no. 4, pp. 227-53, Oct 1998, doi: 10.1016/s0013-4694(98)00075-3.

[111] H. Kazarians, E. Scharein, and B. Bromm, "Laser evoked brain potentials in response to painful trigeminal nerve activation," *International Journal of Neuroscience,* vol. 81, no. 3-4, pp. 111-122, 1995/01/01 1995, doi: 10.3109/00207459509015303.

[112] R.-R. Nir, A. Sinai, R. Moont, E. Harari, and D. Yarnitsky, "Tonic pain and continuous EEG: Prediction of subjective pain perception by alpha-1 power during stimulation and at rest," (in en), *Clinical Neurophysiology,* vol. 123, no. 3, pp. 605-612, 2012/03/01/ 2012, doi: 10.1016/j.clinph.2011.08.006.

[113] Y. Chen, L. De Taboada, M. O'Connor, S. Delapp, and J. A. Zivin, "Thermal effects of transcranial near-infrared laser irradiation on rabbit cortex," *Neuroscience Letters,* vol. 553, pp. 99-103, 2013/10/11/ 2013, doi: https://doi.org/10.1016/j.neulet.2013.07.049.

[114] G. Deco, A. Ponce-Alvarez, D. Mantini, G. L. Romani, P. Hagmann, and M. Corbetta, "Resting-state functional connectivity emerges from structurally and dynamically shaped slow linear fluctuations," *J Neurosci,* vol. 33, no. 27, pp. 11239-52, Jul 3 2013, doi: 10.1523/JNEUROSCI.1091-13.2013.

[115] N. Mancho-Fora *et al.*, "Resting-state functional dynamic connectivity and healthy aging: A sliding-window network analysis," *Psicothema,* vol. 32, no. 3, pp. 337-345, Aug 2020, doi: 10.7334/psicothema2020.92.

[116] T. J. Huppert, S. G. Diamond, M. A. Franceschini, and D. A. Boas, "HomER: a review of time-series analysis methods for near-infrared spectroscopy of the brain," *Appl Opt,* vol. 48, no. 10, pp. D280-98, Apr 1 2009. [Online]. Available: https://www.ncbi.nlm.nih.gov/pubmed/19340120.

[117] N. Naseer and K.-S. Hong, "fNIRS-based brain-computer interfaces: a review," (in eng), *Frontiers in human neuroscience,* vol. 9, pp. 3-3, 2015, doi: 10.3389/fnhum.2015.00003.

[118] A. Oldag *et al.*, "Assessment of Cortical Hemodynamics by Multichannel Near-Infrared Spectroscopy in Steno-Occlusive Disease of the Middle Cerebral Artery," *Stroke,* vol. 43, no. 11, pp. 2980-2985, 2012/11/01 2012, doi: 10.1161/STROKEAHA.112.656710.

[119] P. Smielewski, M. Czosnyka, D. Pickard John, and P. Kirkpatrick, "Clinical Evaluation of Near-Infrared Spectroscopy for Testing Cerebrovascular Reactivity in Patients With Carotid Artery Disease," *Stroke,* vol. 28, no. 2, pp. 331-338, 1997/02/01 1997, doi: 10.1161/01.STR.28.2.331.

[120] M. Kohl *et al.*, "Determination of the wavelength dependence of the differential pathlength factor from near-infrared pulse signals," *Phys Med Biol,* vol. 43, no. 6, pp. 1771-82, Jun 1998. [Online]. Available: https://www.ncbi.nlm.nih.gov/pubmed/9651039.

[121] E. Visani *et al.*, "Hemodynamic and EEG Time-Courses During Unilateral Hand Movement in Patients with Cortical Myoclonus. An EEG-fMRI and EEG-TD-fNIRS Study," *Brain Topogr,* vol. 28, no. 6, pp. 915-25, Nov 2015, doi: 10.1007/s10548-014-0402-6.

[122] A. R. Anwar *et al.*, "Comparison of causality analysis on simultaneously measured fMRI and NIRS signals during motor tasks," *Conf Proc IEEE Eng Med Biol Soc,* vol. 2013, pp. 2628-31, 2013, doi: 10.1109/EMBC.2013.6610079.

[123] J. Rhee and R. K. Mehta, "Functional Connectivity During Handgrip Motor Fatigue in Older Adults Is Obesity and Sex-Specific," (in English), *Front Hum Neurosci,* Original Research vol. 12, p. 455, 2018, doi: 10.3389/fnhum.2018.00455.

[124] M. Xia, J. Wang, and Y. He, "BrainNet Viewer: A Network Visualization Tool for Human Brain Connectomics," *PLOS ONE,* vol. 8, no. 7, p. e68910, 2013, doi: 10.1371/journal.pone.0068910.

[125] M. M. Mesulam, "From sensation to cognition," *Brain,* vol. 121, no. 6, pp. 1013-1052, 1998, doi: 10.1093/brain/121.6.1013.

[126] J. M. Fuster, "Linkage at the top," *Neuron,* vol. 21, no. 6, pp. 1223-1224, 1998.

[127] B. Mazoyer *et al.*, "Cortical networks for working memory and executive functions sustain the conscious resting state in man," *Brain Res Bull,* vol. 54, no. 3, pp. 287-98, Feb 2001, doi: 10.1016/s0361-9230(00)00437-8.

[128] E. K. Miller and J. D. Cohen, "An Integrative Theory of Prefrontal Cortex Function," *Annual Review of Neuroscience,* vol. 24, no. 1, pp. 167-202, 2001/03/01 2001, doi: 10.1146/annurev.neuro.24.1.167.
[129] A. C. Roberts, T. W. Robbins, and L. Weiskrantz, *The prefrontal cortex: Executive and cognitive functions* (The prefrontal cortex: Executive and cognitive functions.). New York, NY, US: Oxford University Press, 1998, pp. viii, 248-viii, 248.
[130] Q. Zou *et al.*, "Intrinsic resting-state activity predicts working memory brain activation and behavioral performance," *Human Brain Mapping,* vol. 34, no. 12, pp. 3204-3215, 2013/12/01 2013, doi: 10.1002/hbm.22136.
[131] C. P. Kaller, B. Rahm, J. Spreer, C. Weiller, and J. M. Unterrainer, "Dissociable Contributions of Left and Right Dorsolateral Prefrontal Cortex in Planning," *Cerebral Cortex,* vol. 21, no. 2, pp. 307-317, 2010, doi: 10.1093/cercor/bhq096.
[132] B. Tomasino and F. Fabbro, "Increases in the right dorsolateral prefrontal cortex and decreases the rostral prefrontal cortex activation after-8 weeks of focused attention based mindfulness meditation," *Brain and Cognition,* vol. 102, pp. 46-54, 2016/02/01/ 2016, doi: https://doi.org/10.1016/j.bandc.2015.12.004.
[133] A. H. C. Fong *et al.*, "Dynamic functional connectivity during task performance and rest predicts individual differences in attention across studies," *NeuroImage,* vol. 188, pp. 14-25, 2019/03/01/ 2019, doi: https://doi.org/10.1016/j.neuroimage.2018.11.057.

Biographical Information

Hashini Wanniarachchi was born and brought up in Sri Lanka. She earned her bachelor's degree from the University of Texas at Arlington in Industrial and Manufacturing Engineering, Arlington, TX, USA. She joined the graduate program in the Department of Bioengineering, the University of Texas at Arlington in 2016. Her research focused on a collaborative project with professors from the Department of Information Systems in the College of Business and Administration in 2017-2018, and an NIH-funded project to investigate transcranial photobiomodulation in humans in 2018-2020. He has given 3 research presentations BMES and OSA Biomedical Optics topical meetings. Her areas of research interests include experimental design, computational modeling, statistical analysis, and optical instrumentation.